

LLE Review

Quarterly Report



About the Cover:

Inertial confinement fusion research at the OMEGA Laser Facility utilizes optical pulses delivered as 60 separate beams to compress target capsules and create the high temperatures and pressures necessary to initiate the reaction. Accurate measurement of the energy time history of each pulse is critical in adjusting the laser system to achieve maximum performance and to the interpretation of the results from each experimental target shot. LLE has recently completed development and installation of a suite of six multichannel streak cameras that are capable of making measurements over the wide energy range that is of interest with the necessary time resolution. Calibration features built into each camera coupled with extensive operation, data reduction, and maintenance software allow the suite to precisely diagnose each beam as a routine part of laser facility operations. On the cover, Dr. William Donaldson, Sr. Scientist, reviews calibrated images of 30 one-nanosecond beam pulses acquired by the bank of cameras shown here. A second identical bank supports the other 30 OMEGA beams. The article "A Self-Calibrating, Multi-channel Streak Camera for Inertial Confinement Fusion Applications" (p. 109) describes this system in detail.



This report was prepared as an account of work conducted by the Laboratory for Laser Energetics and sponsored by New York State Energy Research and Development Authority, the University of Rochester, the U.S. Department of Energy, and other agencies. Neither the above named sponsors, nor any of their employees, makes any warranty, expressed or implied, or assumes any legal liability or responsibility for the accuracy, completeness, or usefulness of any information, apparatus, product, or process disclosed, or represents that its use would not infringe privately owned rights. Reference herein to any specific commercial product, process, or service by trade name, mark, manufacturer, or otherwise, does not necessarily constitute or imply its endorsement, recommendation, or favoring by

the United States Government or any agency thereof or any other sponsor. Results reported in the LLE Review should not be taken as necessarily final results as they represent active research. The views and opinions of authors expressed herein do not necessarily state or reflect those of any of the above sponsoring entities.

The work described in this volume includes current research at the Laboratory for Laser Energetics, which is supported by New York State Energy Research and Development Authority, the University of Rochester, the U.S. Department of Energy Office of Inertial Confinement Fusion under Cooperative Agreement No. DE-FC03-92SF19460, and other agencies.

Printed in the United States of America
Available from
National Technical Information Services
U.S. Department of Commerce
5285 Port Royal Road
Springfield, VA 22161

Price codes: Printed Copy A04
Microfiche A01

For questions or comments, contact Thomas H. Hinterman,
Editor, Laboratory for Laser Energetics, 250 East River Road,
Rochester, NY 14623-1299, (716) 275-0866.

Worldwide-Web Home Page: <http://www.lle.rochester.edu/>

LLE Review

Quarterly Report



Contents

In Brief	iii
A Self-Calibrating, Multichannel Streak Camera for Inertial Confinement Fusion Applications	109
Evolution of Shell Nonuniformities Near Peak Compression of a Spherical Implosion	122
Multibeam Stimulated Brillouin Scattering from Hot Solid-Target Plasmas	128
Hot-Electron Effect in Superconductors and Its Applications for Radiation Sensors	134
Scaling Law for Marginal Ignition	153
Publications and Conference Presentations	

In Brief

This volume of the LLE Review, covering April–June 2001, features “A Self-Calibrating, Multichannel Streak Camera for Inertial Confinement Fusion Applications” by Dr. W. R. Donaldson, R. Boni, R. L. Keck, and P. A. Jaanimagi. This article (p. 109) describes the 60-beam streak camera system used on OMEGA and focuses on the hardware and software calibration techniques that maximize its utility. The system can diagnose each of the beams on every target shot and can measure beam energies with 8% accuracy and timing at 7 ps rms. Beam-to-beam power variations of less than 5% can be detected.

Additional highlights of research presented in this issue include the following:

- V. A. Smalyuk, V. N. Goncharov, J. A. Delettrez, F. J. Marshall, D. D. Meyerhofer, S. P. Regan, and B. Yaakobi (p. 122) present modeling and shot data showing the evolution of shell modulations near the point of peak compression in spherical, direct-drive implosions. The effect of two different levels of beam smoothing is described. Both the model and the experiment show that modulations in the shell areal density decrease during compression and increase during decompression.
- W. Seka, H. A. Baldis, J. Fuchs, S. P. Regan, D. D. Meyerhofer, C. Stoeckl, B. Yaakobi, R. S. Craxton, and R. W. Short (p. 128) report on the first multibeam laser–plasma interaction experiments with a critical density surface present at all times. These plasma conditions are tailored to resemble future direct-drive laser fusion implosions on the NIF. The results show strong evidence of electromagnetic (EM) wave seeding of SBS backscatter as well as evidence of strongly driven, common, symmetrically located ion waves. The expected SBS scattering levels for NIF direct-drive ignition experiments are well below 1%. This gives confidence that good direct-drive target performance will be achieved.
- A. D. Semenov, G. N. Gol’tsman, and R. Sobolewski (p. 134) survey the main aspects of nonequilibrium hot-electron phenomena in superconducting films. Various theoretical models developed to describe the hot-electron effect are presented. The article describes a number of radiation-sensing devices that have been fabricated and tested and demonstrate significantly improved performance over conventional implementations.
- K. Anderson, R. Betti, and V. N. Goncharov address the issues associated with determining the minimum drive energy needed to achieve ignition in inertial confinement fusion implosions (p. 153). A new model that consistently incorporates two competitive scaling approaches is developed. Topics covered in this article include hot-spot dynamics, two approaches to shell modeling, derivations of ignition scaling, and verification of initial assumptions. Good agreement with other published results is shown.

Thomas H. Hinterman
Editor

A Self-Calibrating, Multichannel Streak Camera for Inertial Confinement Fusion Applications

Introduction

The OMEGA laser at LLE uses 60 symmetrically aimed laser beams to compress direct-drive inertial confinement fusion (ICF) targets.¹ The ICF targets are, typically, deuterium-tritium (DT)-filled microballoons. The laser beams heat and compress the target, causing the DT fuel to undergo nuclear fusion, which releases energy in the form of neutrons. The fuel must be highly compressed for this process to proceed efficiently.² The shape of the laser pulse, which typically has a length of 1 to 3 ns, can be adjusted to optimize the compression and produce a hot core of DT fuel;³ however, optimal compression will happen only if the driving force imparted by the lasers beams to the spherical target is uniform. If one laser beam is more energetic than its neighbors, it can seed hydrodynamic instabilities that can prevent the formation of the highly compressed core.⁴ Because these hydrodynamic instabilities can be seeded in about 100 ps, it is necessary to ensure that the driving force imparted by the laser be uniform on the 100-ps time scale. This defines the period over which power balance must be achieved. To achieve the best target performance, the OMEGA laser must ultimately achieve 1% irradiation uniformity during each 100-ps time slice of the pulse. Achieving this goal is aided by the fact that several different beamlines illuminate any single point on the target. The averaging effect of the overlapping beams reduces the requirement for beam-to-beam power balance to 5%.⁵

Several factors affect power balance: In theory, if all of the optical components and all of the electrical power-conditioning units in each beamline are identical, every beamline should have the same energy and pulse shape. In practice, not all flash lamps are equal and not all optical components are equal, especially after being exposed to many shots at high optical fluences. The result is that when the laser is fired, the beams are currently energy balanced on target to 3% rms.

Equalizing the beam energies does not guarantee equal pulse shapes. The gains and losses of each beamline must be equal if the system is to be power balanced, which is not necessarily true for energy balance because the system is

nonlinear. For example, increasing the gain in an amplifier farther downstream can compensate for a poorly performing optic in a beamline. Although this would allow the system to be energy balanced, it will likely change the temporal shape of the optical pulse. Power balance requires that the pulse shape of all 60 beamlines be measured.

Another major factor affecting the pulse shape is the spatial-smoothing technique employed on OMEGA. Smoothing by spectral dispersion (SSD) is used to rapidly shift the speckle pattern produced at the focus of the laser.⁶ The rapid shifting of the speckle pattern produces a uniform, time-integrated illumination profile on the ICF target. SSD works by modulating the laser frequency across the spatial and temporal profiles of the beam. Each frequency propagates at a slightly different angle with respect to the optic axis of the laser. The speckle pattern produced at the target then shifts rapidly in time. Misalignment of the SSD system, however, can cause the frequency modulation (FM) of the laser pulse to be converted into amplitude modulation (AM) at SSD drive frequencies of 3 and 10 GHz as well as at the harmonics and sum and difference frequencies. The AM can damage optical components as well as adversely affect power balance.

All of these factors can be adjusted, but only if their impact is measured. Any system that is used to measure pulse shapes on OMEGA must meet several stringent requirements. The temporal bandwidth must be able to detect temporal features in the pulse shape with frequencies as high as 10 GHz. The bandwidth is high for two reasons: First, the recorded pulse shapes are fed into theoretical models of the implosion dynamics. Higher-bandwidth signals allow more-faithful models of the implosion dynamics. Second, the 10-GHz bandwidth allows us to see any FM-to-AM conversion, which could be specific to a single beamline. The recorded signal should span a range of pulse intensities of over 1000:1. Much of the interesting implosion physics happens during the initial “foot” portion of the pulse, which is at 27% of the peak for a typical shaped optical pulse (as shown in Fig. 87.1). The recorded intensity range should be sufficient to measure the pulse shape

with an accuracy of a few percent at the peak and within about 10% in the foot. The longest pulse that can be generated with the OMEGA laser is about 4.5 ns, with 1-ns to 2-ns pulses being the most typical. The instrument record length should be slightly longer to allow us to handle the case of deliberately delayed beams, so the total record length should be about 6 ns. The OMEGA laser operates at a wavelength of 351 nm; this defines the wavelength at which the streak cameras must operate. Since there are 60 beamlines in the OMEGA system, the acquisition system must support 60 simultaneous data-acquisition channels. This data must be recorded on all OMEGA system shots, which occur on a 1-h shot cycle, so reliable operation as well as the ability to recover from equipment failure on a 1-h shot cycle is essential.

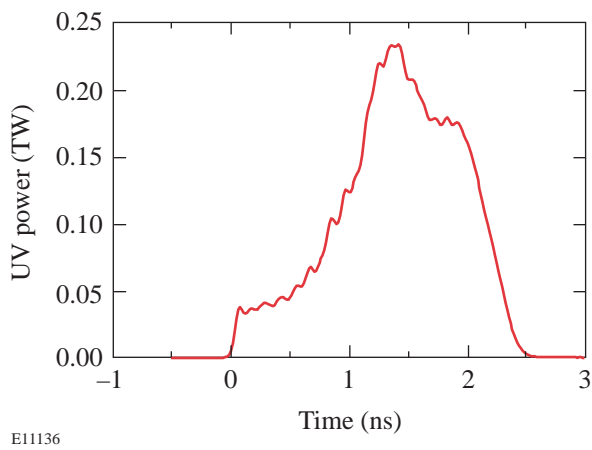


Figure 87.1

A typical shaped pulse used for ICF experiments has an initial, low-energy “foot,” followed by the more-intense main part of the pulse.

Two possible alternatives were considered for a measurement system that would meet these requirements. The first alternative was to use photodiodes and transient digitizers. When the OMEGA laser was first activated, the UV pulse shape was measured with a Tektronics SCD5000 transient digitizer and a Hamamatsu photodiode. The temporal resolution of this system was about 4 GHz, which was insufficient to see the modulation due to SSD, as shown in Fig. 87.2. We have also found that photodiodes, which are optimized to measure high-bandwidth pulses, experience a droop in the signal when measuring long pulses. With a cost approaching \$70,000 per channel, this was an inappropriate option for a 60-beam laser. By way of comparison, the National Ignition Facility (NIF) at Lawrence Livermore National Laboratory is planning to monitor the 192 beams of the NIF with vacuum photodiodes and transient digitizers.⁷ The NIF will use temporal and power multiplexing to reduce the number of digitizers and detectors

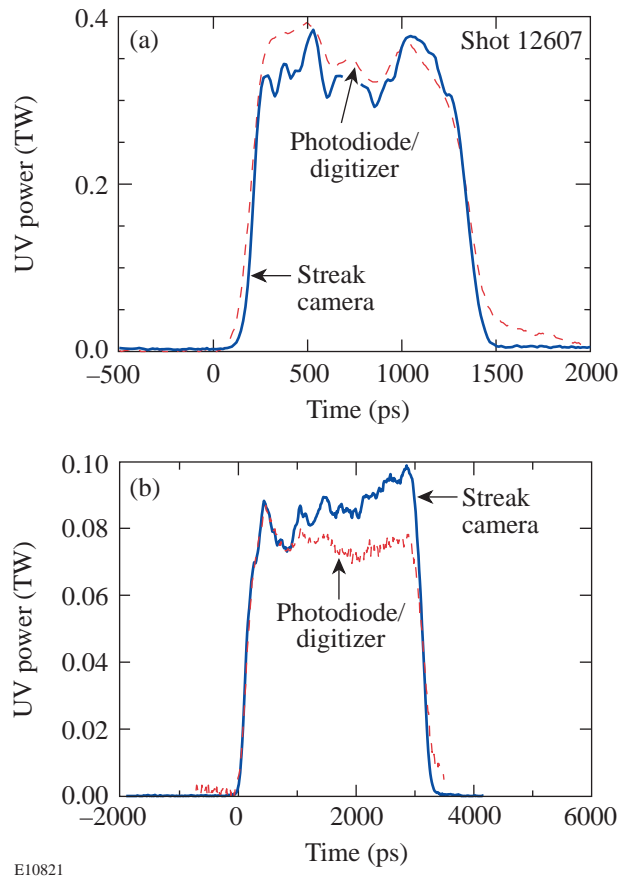


Figure 87.2

A comparison of a 4-GHz diode/digitizer to a 10-GHz streak camera. (a) The photodiode (dashed trace) was unable to reproduce the high-frequency structure measured with the streak camera (solid line). (b) One of the problems with the transient digitizer and diode measurement system (dashed trace) is a tendency for the signal to droop when measuring long pulses. This results in a distorted pulse shape as compared to the streak camera data (solid line).

to 48. The multiplexing scheme is designed to achieve a dynamic range of 5000:1 at 1 GHz with a cost per channel of \$6200. Such a system would not meet the requirements of the OMEGA laser system as stated above.

The second alternative, which is the one described in this article, uses six streak cameras to measure the UV pulses shapes in each of the 60 OMEGA beamlines. The photocathode of each streak camera is illuminated by a small portion of the light from ten OMEGA beamlines. A typical image is shown in Fig. 87.3. This system can measure all 60 beams of OMEGA with a bandwidth of 10 GHz and a per-beam dynamic range of over 10³:1. The cost per channel is about \$12,000, plus in-house labor.

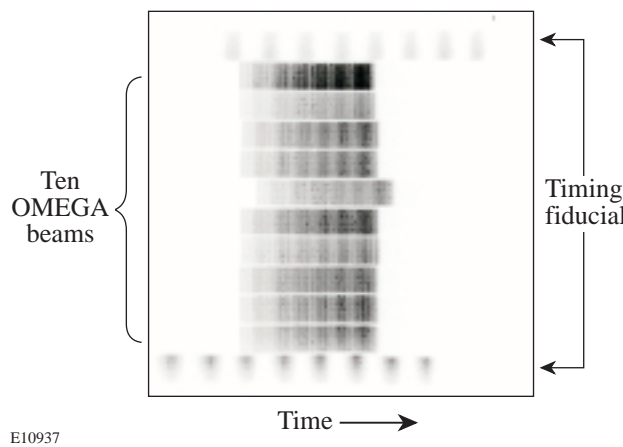


Figure 87.3

The corrected image of the cluster 5 streak camera showing ten multiplexed beams and two fiducial traces. All of the beams are actually nominally co-timed. The apparent delays are due to differences in the fiber OPD to the cameras. The striations are due to FM-to-AM conversion of the 10-GHz SSD.

The System

Multichannel streak cameras are not new. A number of research groups have used them for a variety of measurements.^{8–10} What is unique about this system is the enhanced signal-to-noise ratio (SNR) of the recorded data and the suite of autocalibration modules. These allow accurate, photometrically calibrated measurements over a period of months. OMEGA's pulse-shape-measurement system is composed of six major subsystems: the fiber launcher assembly, the optical-fiber bundles, the fiber-bundle imaging optics, the streak tube, the tube electronics, and the charge-coupled-device (CCD) camera. Each of these subsystems (illustrated in Fig. 87.4) must be optimized to meet the specifications listed above. Figure 87.5 shows the layout of the streak camera.

Each OMEGA beamline can deliver about 550 J of 351-nm light to the target. An uncoated glass surface (4% reflection) is inserted into each beam for diagnostic purposes. After three additional 4% reflections, part of the diagnostic energy is delivered to the streak camera's fiber launchers. One consequence of SSD is that each beam is about 300 times diffraction limited with an instantaneous spatial profile that has 100% speckle modulation. It is impossible to couple this light into the UV gradient-index fibers available at the time the system was constructed. The time-varying speckle coupled with angular deviation of each frequency would result in coupling losses, which would manifest themselves as AM at the output of the fiber. To overcome this problem, a system of lenses and diffusers was used to uniformly sample the spatial profile of the beam with a seven-fiber bundle. The light passes through a lens

with a 20-cm focal length, then immediately passes through a precision diffractive-optics diffuser, which spreads the light into a 2° cone angle. A second diffuser, with a 0.5° cone angle, is placed at the focus of the first lens. Finally, a 1-cm lens focuses the light into the fiber bundle. This arrangement produces a weakly modulated 2-mm-FWHM Gaussian profile at the fiber input plane at a wavelength of approximately 351 nm.

To accurately reproduce the waveform, the beam must be sampled at several points over the central portion of the 2-mm spot. The use of a 1-mm-diam-core, step index fiber would be incompatible with the required bandwidth of the system, so an alternative method was used. The 351-nm light must propagate through the 15 m of fiber from the launcher to the streak camera. The 15 m allows for equal optical path lengths from the pickoff to the camera, as well as transport through the radiation shield wall that surrounds the target chamber. To maintain the

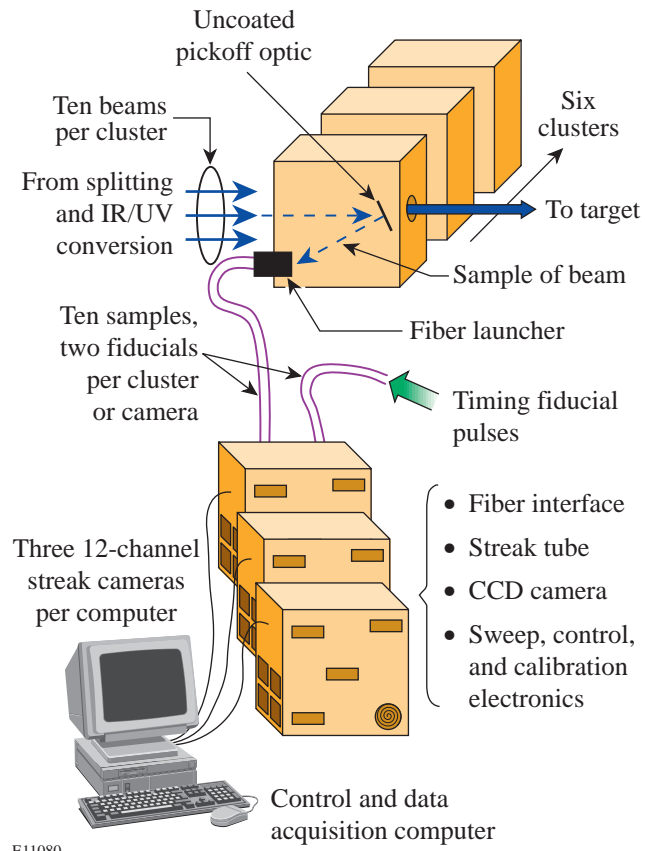


Figure 87.4

The OMEGA pulse-shape-measurement system consists of six streak cameras, each measuring a single cluster. Optical fibers transport a small portion of the energy from each beamline to the streak cameras.

highest-possible bandwidth, a 100- μm -core UV fiber was chosen. This high-bandwidth, UV-transmitting, graded-index optical fiber was developed by the Vavilov State Optical Institute, St. Petersburg, Russia, for use in laser diagnostics on the National Ignition Facility.¹¹ This fiber has a dispersion of 1 ps/m at 351 nm, giving a maximum bandwidth of 11 GHz. Since one fiber is inadequate to sample the entire beam, a bundle of seven fibers is used with six fibers hexagonally packed around a seventh fiber. The fiber lengths are matched such that broadening due to optical path differences (OPD's) in the bundle is negligible. To verify that the OPD's were the same, the output of a single fiber, injected with a 20-ps pulse at 351 nm, was compared with the output of a fiber bundle injected with the same pulse. The measured pulse lengths were 28 and 29 ps, respectively. The impulse response of the input fiber is therefore 21 ps, assuming the broadening and pulse width add in quadrature.

When the light emerges from the fiber bundle, it is coupled into a homogenizer bar, which produces a uniform rectangular spot from the seven-fiber hexagonal bundle by multiple surface reflections. This maximizes the fill factor on the photocathode. Ten bars are arranged in a linear array as shown in Fig. 87.6. At either end of the array are two additional homogenizer bars, which are fed by a fiducial laser operating at 527 nm. The fiducial laser is co-timed with the UV pulse from the OMEGA laser and consists of eight pulses separated by 548 ps. The fiducial pulses enable cross-timing between the six

UV streak cameras and other diagnostics in the system. An off-axis Offner triplet is used to image the optical signals onto the linear photocathode, as shown in Fig. 87.7. The mirrors are metallic, thus reducing chromatic defocus. This particular arrangement was chosen so that a variety of illumination fixtures could be placed on a computer-controlled motorized stage and individually selected to be focused onto the photocathode. The other illumination fixtures are used for *in-situ* calibration of the streak camera, which will be described later.

The streak tube is a standard commercial tube—a Philips P510—with an S-20 photocathode at the input. The electron optic terminals were biased as follows: photocathode –15 kV, slot –12.5 kV, and focus –14.5 kV. These voltages were adjusted for each tube to produce the sharpest image in the time dimension of the photocathode at the CCD with the sweep voltages held at 0 V. Figure 87.8 shows that at best focus the FWHM of the photocathode image varies as a function of both position on the photocathode and signal intensity. A low signal near the center of the image induces a broadening that has an equivalent effective bandwidth of 13.5 GHz. At the other extreme, an intense signal near the edge of the photocathode induces a broadening equivalent to 10.5 GHz. The intense signal result represents the worst possible case. The signal level was near the CCD's full well capacity. The bandwidth was limited by both saturation of the CCD and diffusive scattering in the fiber-optic coupling of the light into the CCD. This signal level is ten times what is used in normal operation.

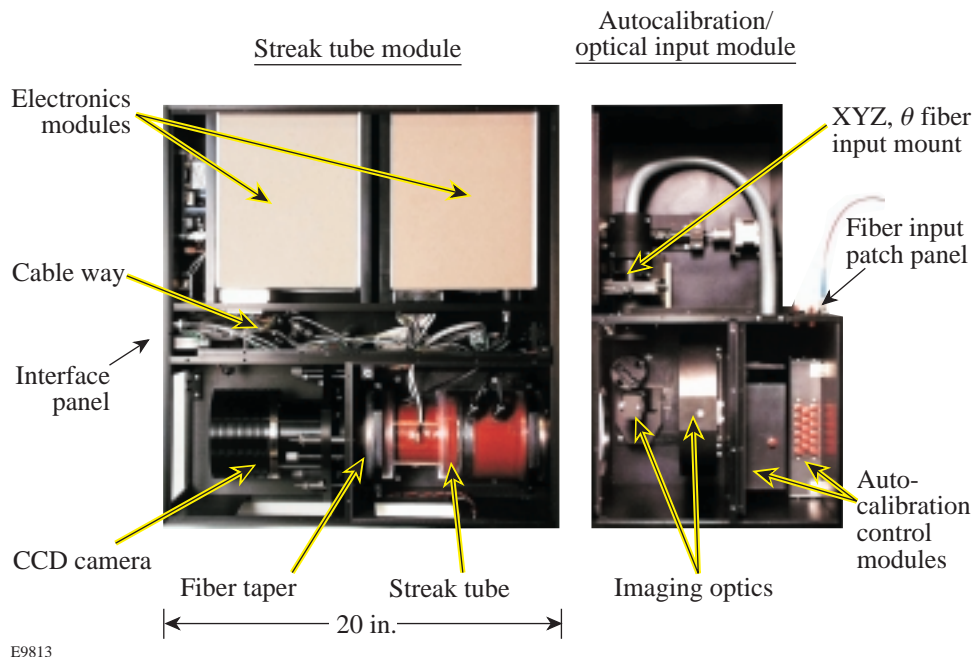


Figure 87.5
The layout of the self-calibrating, multi-channel streak camera employed on the OMEGA laser.

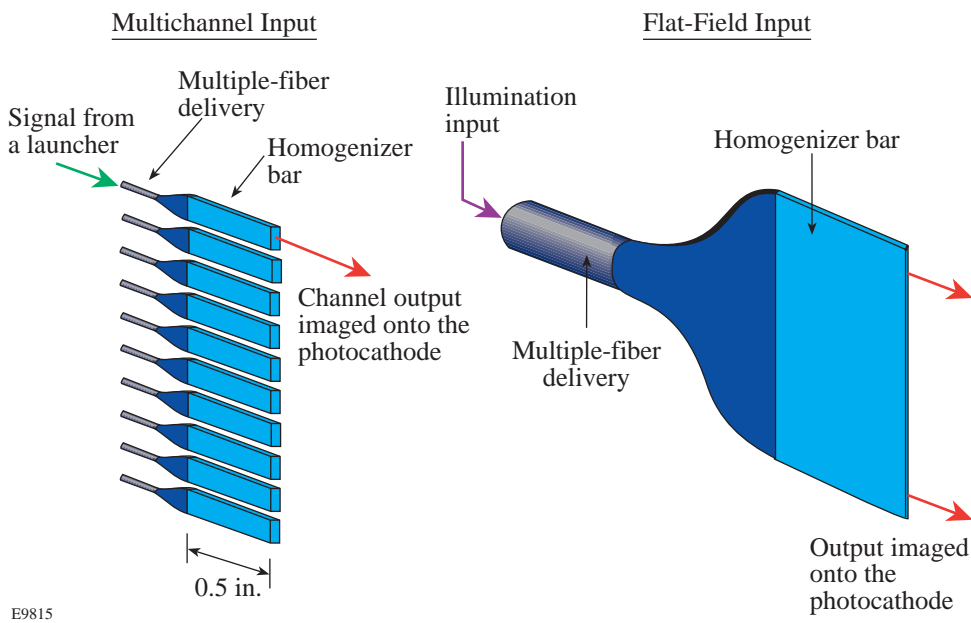


Figure 87.6

A mechanical translation stage allows several different illumination heads to be placed at the object plane of the Offner triplet. Layouts of two illumination heads are shown here. Multiple reflections from the edges of the glass homogenizer bars produce a uniform illumination source.

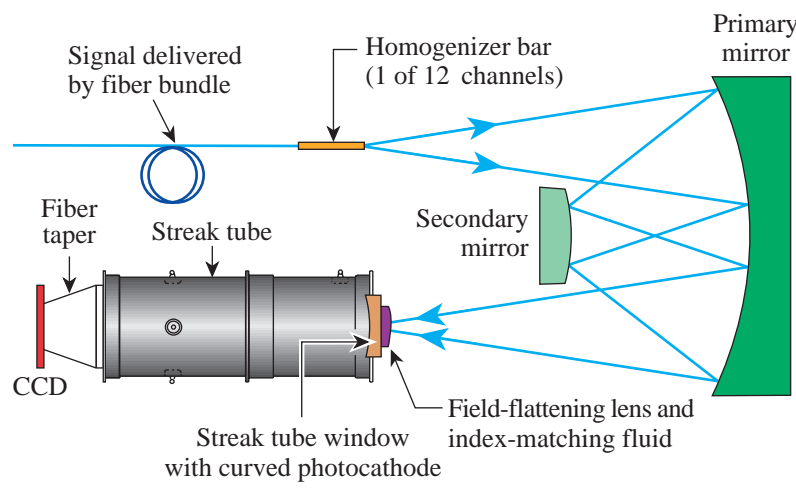


Figure 87.7

The optical input to the streak camera uses an Offner triplet to image the fiber bundle onto the streak tube photocathode. The streak tube window is curved, and a field-flattening lens is attached to it with index-matching fluid.

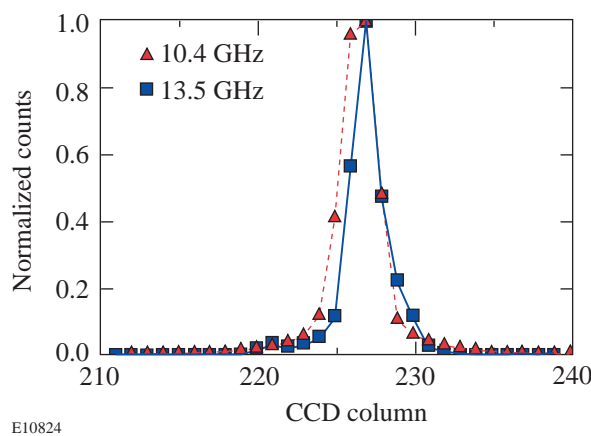


Figure 87.8

In focus mode, the image of the photocathode is adjusted to give the sharpest line at the CCD. The width of the line varies with position and intensity. The solid line shows the best focus at the center on the streak tube axis at low intensity. The FWHM is 2.5 superpixels (binned 2×2) giving a bandwidth of 13.5 GHz. Off-axis and with an intense signal, the line width degrades to 3.4 pixels, corresponding to a bandwidth of 10.4 GHz.

The output fiber-optic faceplate of the tube has a P20 phosphor screen, which is reasonably well matched to the spectral sensitivity of the back-thinned CCD used to acquire the image. To match the image size at the P20 phosphor to the CCD camera, a 1.3:1 fiber-optic taper is used. Index-matching fluid is used at the mating surface between the fiber-optic taper and the streak tube to prevent the formation of Newton rings in the image recorded by the CCD camera. The CCD camera is a Roper Instruments Series 300 with a fiber-coupled 1024×1024 CCD array using a back-thinned SITe003AB chip. There are only passive optical components between the phosphor and the CCD; no image intensifiers are used in the system. The large format of the array allows us to keep the image compression ratio of the fiber taper small, which reduces transport losses. Typically the output of this camera is binned 2 by 2 to give a 512×512 image. This allows a rapid, low-noise readout of the array without compromising the data. At the best focus of the electron optics, the width of the photocathode image is about 2.5 superpixels wide; thus we gain no additional information by unbinning the pixels. For the remainder of this article these superpixels will be used as the standard CCD row and column unit.

The electronics for controlling the streak tubes were designed at LLE. Each camera has four interchangeable modules. The modules control the high-voltage bias, the sweep voltages, triggering, and external communications. The external communications module uses a RS-232 serial port to tell the onboard processor to read and set voltage levels, optical head positions, and sweep speeds. The high-voltage bias module sets a single high-voltage level that biases the cathode, slot, and focusing electrodes of the tube through a resistive divider. The electron optics of the tube are such that the focusing conditions are relatively insensitive to the absolute magnitude of these three voltages but very sensitive to their ratios. Thus, small variations in the power supply do not significantly affect the final image quality. In normal operation, the deflection plates of the tube are driven by a filter network, which, in turn, is driven by a MOSFET/avalanche transistor stack.¹² This arrangement produces a ramp that sweeps the electron beam across the phosphor screen in 6 ns and has a deviation from linearity of less than 12%. This is the standard operating sweep speed for these cameras; however, three additional sweeps of 2-ns, 20-ns, and 45-ns duration can be selected electronically. It is also possible to sweep the electron beam very slowly by ramping the voltage with a high-voltage digital-to-analog ramp. The slow ramp is used for the flat-field and geometric-distortion corrections, which are discussed in the next section.

Calibration

The six streak cameras that measure OMEGA's 60 beams are essential to acquiring data reliably on a 1-h shot cycle. If a camera should fail, the modular design of the electronics allows us to rapidly repair the camera before the next shot. Simply acquiring data, however, is not sufficient. The data must be well calibrated and give meaningful results. *In-situ* calibration fixtures facilitate rapid recalibration of the streak cameras. It is insufficient to calibrate the streak cameras only at installation time. To ensure valid measurements at the 1% level, the streak cameras are recalibrated weekly.

A unique feature of the streak camera is the ability to slowly and uniformly ramp the electron beam across the phosphor in about 1 s. The slow ramp was designed to facilitate the acquisition of flat-field images with a large signal-to-noise ratio at very low tube currents. The slow ramp is also used to acquire images that are used to correct geometric distortions.

Several sources of geometric distortion exist in the streak camera images. The system has a set of several optic or electron-optic axes defined by the fiber-bundle array, the photocathode-electron optics, and the CCD camera. Ideally all of these axes should be aligned, but variations in tube construction cause misalignment in the electron optics. The CCD is aligned such that the image of the photocathode in focus mode (no voltage on the sweep plates) is parallel to the column axis. When voltage is applied to the streak plates, the streaked image may not move parallel to the row axis of the CCD. Fringing fields at the edges of the sweep electrodes cause pincushion distortion in the image. Also, the electron optics produce a curved image that is recorded on a flat phosphor screen. These effects must be removed from the image.

To correct these distortions, the motorized translation stage in the input optics assembly is set to the geometric distortion position. In this position, a fiber array, fed by a light-emitting diode (LED), is coupled to a homogenizer bar that uniformly illuminates the photocathode (see Fig. 87.6). A uniform wire mesh in front of the homogenizer modulates the light in the spatial direction. In this configuration, the slow ramp is used to sweep the electron beam. It takes about 1 s for the signal to sweep across the CCD. During this time, the current to the LED is modulated with a 30-Hz square wave. The resulting image consists of a uniform grid of bright rectangles (Fig. 87.9). The rectangles should be uniformly separated in space and time; however, the distortion mentioned above causes irregularities in the grid. A deconvolution algorithm is used to find the

position of each of the rectangles in the image. Next, an indexing routine assigns each rectangle its correct location in a uniform grid. The indexing of approximately 2000 points defines a mapping from the distorted to the undistorted image. Using standard image-processing techniques, the mapping can be described as an n th-order polynomial.¹³ This procedure does not use the Jacobian of the coordinate transformation to conserve the total CCD analog-to-digital units (ADU) count. Future software upgrades will include this feature; however, when a typical geometric distortion correction is applied, the total ADU count between the corrected and uncorrected image differs by less than 0.5%, which gives acceptable results for the current implementation. Polynomial fits up to the fourth order are calculated for each mapping. The undistorted images are cross-correlated with an ideal grid to determine which polynomial degree gives the best distortion correction. The undistorted

image consists of uniformly spaced rectangles in vertical columns and horizontal rows.

Once the geometric-distortion correction has been calculated, the streak camera can be flat fielded. A traditional flat field of a CCD is insufficient because we are mapping a line to a 2-D image. Each point on the photocathode maps to a trajectory on the CCD. The geometric-distortion correction maps the trajectory of a single point on the photocathode to a single row of pixels in the undistorted image. Variations of the photocathode efficiency and the homogenizer mean that different rows are essentially illuminated with different light sources. It is important to correct the geometric distortion before correcting the flat field to guarantee that the entire row derives from the same point on the photocathode. Each pixel in a row is subjected to variations in the phosphor screen, the fiber taper, and the sensitivity of each CCD element, so the first operation in calculating the flat-field image is to normalize each pixel with respect to all the other pixels in the row. Next, the sum of the pixels in each row is normalized to all the other rows. This procedure ignores regions of the image illuminated by the edges of the photocathode where the sensitivity of the system drops down to the noise level. The flat-field illuminator is similar to the geometric-distortion fixture, but the light source is continuous and the wire grid is removed. The slow-ramp module is used to sweep the electron beam across the phosphor. In this configuration, the illumination level can be adjusted so that only a few (<10) photoelectrons are in the tube at any time during the sweep. As a result, the electron current will not distort the electric field of the focusing optics, and the signal can be collected at a larger fraction of the CCD's full well capacity than is possible in pulse mode.

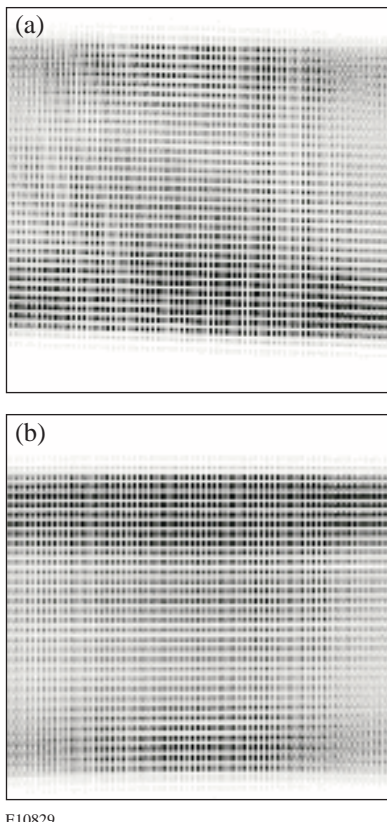


Figure 87.9

Calibration image produced by the geometric distortion source and the slow sweep. (a) The electron optics produce a skewed and distorted image at the CCD. (b) The modulation in the distorted image is removed by a transformation that maps the image to a regular grid.

Aberrations in the electron optics cause some vignetting of the electron beam at the ends of the aperture. This causes a roll-off of about 20% to 30% in the sensitivity near the edges of the sweep, as shown by the lineout of a single row (see Fig. 87.10). The slight upturn at the very edge is due to scattered photoelectrons in the tube when the beam is outside the viewing area. This creates an uncalibrated region at the edges of the tube, so trigger timing should be set to keep the signal away from the edges of the image in normal operation. The high signal levels provided by the calibration source give excellent signal to noise in the flat-field image. Additionally, the signal to noise is enhanced by averaging 120 flat-field images. These flat-field images are acquired automatically in 10 min, so the volume of calibration data greatly exceeds the volume of signal data. The slow sweep is vulnerable to stray magnetic fields at

the power line frequency, which causes a ripple at the 1% level. Since the sweeps are not synchronous with the power line frequency, the ripples are averaged to zero when the 120 flat fields are averaged. In normal operation these stray fields are not a problem because their oscillation period is 10^8 times greater than the duration of the sweep. When the camera is operated in the fast-sweep mode, these stray fields would manifest themselves as a small, uniform dc offset in the flat field. A planned upgrade to these cameras will include the addition of μ -metal shielding to the cameras to decrease the susceptibility to magnetic fields.

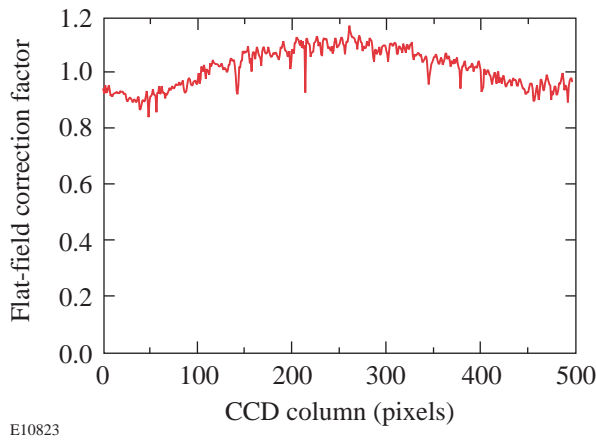


Figure 87.10

The flat-field correction factor is an image the same size as the CCD image. After geometric-distortion correction, each row in the image can be mapped to a single point on the photocathode. A lineout of one of the flat-field rows is shown. The roll-off toward the edges is due to the focusing optics obscuring part of the electron beam. The high-spatial-frequency structures are correlated with adjacent rows and are associated with dead spots in the hexagonal grid of the fiber-optic taper.

Next, the sweep speed must be calibrated. A square optical pulse is modulated with a 1.824-GHz sine wave to produce a train of eight pulses separated by 548 ps. The pulse train is injected into a fiber, and, using a 1:16 commercial fiber-optic splitter, it is divided into 12 fibers that feed a third calibration illuminator head on the streak camera. When this illuminator is placed at the object plane of the Offner triplet, the pulse train is fed to all 12 channels of the streak camera. Approximately 120 images are acquired with different trigger timing delays. The midpoint of each pulse pair in the image is assigned the derivative $\Delta\tau(\text{ps})/\Delta x(\text{pixel})$, which gives about 700 independent measurements of the sweep speed for each channel distributed over the 512 pixel positions. The sweep speed cannot be calibrated at points within 274 ps of the edges. A best-fit interpolation is used to calculate dt/dx . This function is

integrated to determine time as a function of position in the CCD image. The constant of integration is chosen to assign a time of 60 ns to the center pixel. This prevents the uncalibrated region near the ends of the sweep from affecting beam-to-beam timing for all sweep speeds. The sweep speed is calculated independently for each channel. The geometric-distortion correction ensures that the sweep speed for each channel deviates from a linear fit by less than 20 ps over 5 ns, as shown in Fig. 87.11. The distortion correction should also guarantee that the sweep speeds of all the channels are identical; in practice this is not the case. Residual errors are due to uncorrected higher-order geometric distortions, resulting in slightly different sweep speeds for each channel. Finally, the sweep speed data is used to correct the recorded pixel values for the electron beam's dwell time (dt/dx) on the pixels by dividing the recorded CCD analog to digital units (ADU) by the relative dwell time on each pixel.

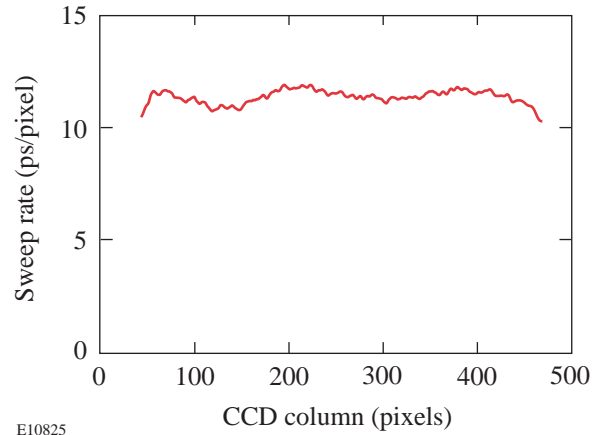


Figure 87.11

The sweep rate of a streak camera channel typically has about a 10% variation from perfect linearity. Roughly 40 channels at either end of the trace cannot be calibrated properly because of the spacing of the fiducial pulses used to calibrate the system. Most of this uncalibrated region lies in the dead zone of the flat-field image.

Operational Considerations

Once the streak cameras are calibrated, they are approved for operation during OMEGA system shots. The calibration procedures listed above are carried out with specific voltage levels applied to the various electrodes within the streak tube. If those voltages change, the calibration is no longer valid. To guarantee that the streak cameras remain in calibration, all of the voltages applied to the streak tube are recorded at the time of the laser shot. The image acquired on the shot is stored in Hierarchical Data Format (HDF). This format allows the image, voltage settings, and background frames to be saved in

the same platform-independent computer file. We have observed that the on-shot voltages do change with time. Typically they exhibit a slow drift, which appears to be associated with the aging of components. While a feedback loop partially compensates for this drift, weekly recalibrations are still required to keep the on-shot voltage values within 1% from the average values recorded during the calibration measurements. The acceptable range is arbitrarily set at 1.5 standard deviations of the variations recorded during the calibration measurements. If more than a week elapses since the last calibration, this condition may not hold and the software will report the voltages as being out of specification.

Two positions of the motorized illumination fixture can be used to acquire streak optical data. The first illuminates the entire photocathode with the light from a single optical-fiber bundle. The second is the standard configuration, which will be discussed exclusively in the remainder of this article. The standard configuration has ten OMEGA beamlines multiplexed onto each camera along with two fiducial pulse trains, as shown in Fig. 87.3. The fiducial laser pulses serve two purposes: First, they verify the integrity of the calibration. The fiducial laser signal consists of eight pulses evenly spaced in time. On each shot, we can measure the fiducial spacing and verify that time-axis calibration is within acceptable limits. On a typical shot, the average measured period of the fiducial pulses over all six streak cameras will be 550 ps with a standard deviation of about 8 ps. The average time displacement between two binned 2×2 superpixels is 12 ps. Thus, the timing of events with separations of the order of 0.5 ns can be determined with subpixel resolution. If, for some reason, the voltages on a streak camera go out of specification on a shot, the streak waveforms from that shot can be rescaled along the time axis by the ratio of the average fiducial period to the true fiducial period. This has been found to reduce timing errors on the distorted streak traces by 60%.

The second function of the fiducial pulse train is to determine the timing of the OMEGA beamlines. A separate instrument is used to guarantee that all beams are co-timed at target chamber center to within 10 ps. The instrument utilizes a cw mode-locked laser to check the path length of all the OMEGA beamlines and cannot operate when the main laser is fired. Data from a series of laser shots are acquired, and the timing of all the beams relative to the fiducial pulses is determined. Typically the rms timing difference between any one beam and the fiducial laser is about 15 ps averaged over 20 laser shots. Once this on-shot calibration has been completed, the streak cameras become the primary diagnostics for determining the

delay between beams and the fiducial. The OMEGA laser is often shot with some beamlines intentionally delayed. The streak cameras allow the fine adjustment of the delay. The fiducial pulse is also fed to many other target diagnostics such as x-ray streak cameras. By cross-timing with respect to the ultraviolet streak cameras, the absolute timing of any signal with respect to the laser pulse can be determined for consecutive system shots to about 10 ps rms. Over a period of several months, the jitter between the UV streak cameras and any instrument using a fiducial is less than 50 ps.

One of the primary uses of the streak cameras on OMEGA is monitoring power balance on the system, i.e., to ensure that all of the beams have the same instantaneous power.⁵ A separate diagnostic, using a calibrated pickoff, measures the energy in each beamline to $\pm 1\%$ precision.¹⁴ The integral under the power curve measured on the streak cameras is normalized to equal the measured energy of the beamline. A plot of the streak-integrated CCD ADU versus measured UV energy is a straight line over the usable operating range of the streak cameras as shown in Fig. 87.12. This shows that not only are the streak cameras photometrically calibrated, but the response is linear over the range of typical signal levels measured on the OMEGA system. If the images show signifi-

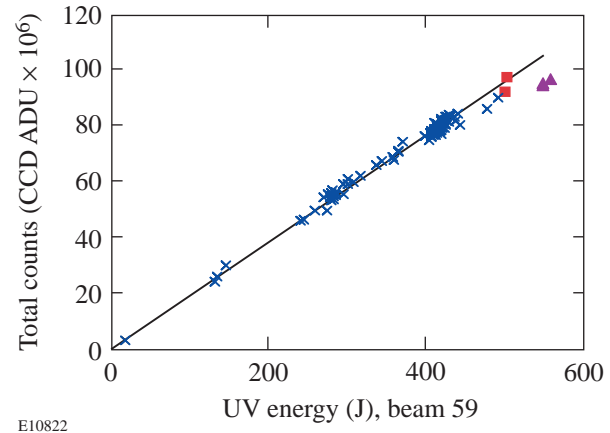


Figure 87.12

The responses of the streak cameras are photometrically calibrated. The total number of CCD counts associated with channel 59 is plotted against the measured UV energy in the beam in joules. The total number of counts is multiplied by the installed filtration. The response is linear up to 500 J UV (x's) over many different pulse shapes. The points above 500 J were 1-ns square pulses (triangles). The filtration on these shots was insufficient to prevent distortion of the streak camera image. The amount of distortion in the image depends on the number of active beams. The two points denoted by squares illustrate that the photometric calibration depends on the total streak tube current.

cant distortion, the linearity of the response breaks down, as indicated by the points designated with triangles. The ambiguity of the maximum-allowed signal level is illustrated by the two points labeled with squares at the 500-J level, which differ by about 10%. On both shots, the signal level in the channel exceeded the maximum-allowed counts. In one case, ten beams were active on the camera and the imaged was distorted. In the other case, only one beam was active for that shot and the image showed no distortion. The linearity of the sensitivity was also preserved in the latter case. Thus, it is possible for the local current density extracted from the photocathode to exceed the threshold for distortion as long as the average current density for distortion is not exceeded.

The measurable range of signal levels is determined by the optical filtration placed in front of the optical-fiber launchers. In addition to the fixed filters, two filters are on removable shuttles. These filters have attenuations of 1.75 and 5.75 and can be inserted separately or jointly, giving four possible intensity levels at the photocathode. The filtration level is chosen to get the maximum performance from the streak camera. The peak signal detected at the CCD camera is limited by the current in the electron tube. As the number of electrons in the tube increases, the image at the phosphor becomes distorted. Initially the distortion manifests itself as a spreading of the signal in both the space and time directions. As the distortion becomes more severe, the image starts to compress and bend. The maximum-acceptable level of distortion has been arbitrarily set in terms of the crosstalk between the channels in the spatial direction. When all beams on a given camera are active, the signal in the interstitial region between channels should not exceed 5% of the signal in the channel. This guarantees that the interchannel crosstalk is approximately 1% to 2% in the pixels adjacent to interchannel dead space and decays to zero in less than one-third of the channel width. Of course, this limit is flexible. If only one beam is present on a camera at a given signal level, the crosstalk distortion will be less than if all ten beams were present at the same level. The distortion is affected by both the local current density and total current in the tube. The 5% level was chosen to accept signals with 1% to 2% crosstalk between adjacent channels. At this level, the crosstalk is dominated by the decay characteristics of the streak tube phosphor and not the electron optics. Although most of the phosphorescence generated by the electron beam arrives at the CCD within a few hundred milliseconds, the phosphor will continue to emit light for as long as 10 s.⁹ To achieve the highest optical transfer efficiency, the coupling between the CCD and the phosphor is a fiber taper. This precludes putting a shutter between the phosphor and the

CCD. Thus, as the image in the CCD shifts from row to row, it acquires an exponentially decaying tail from the phosphor decay. The last channel to be read is most affected because it has been shifted through all residual images of the other channels. We have limited this effect by choosing long exposure times, which give the phosphor time to decay before the image starts to shift, but dark current in the CCD limits exposure times. The compromise of a 3-s exposure time generates a crosstalk of 1% to 2%.

Within these limitations the useful range of the streak camera has been quantified. Each of the 12 channels is defined by 512 individual measurements. The input optics are arranged such that each channel illuminates a 24-pixel-high column on the CCD with approximately uniform intensity; thus, each of the 6144 (= 512 × 12) individual intensity measurements is the average of 24 individual pixel measurements. Therefore, an average, standard deviation and the signal-to-noise ratio can be calculated for each point in the waveform. Figure 87.13 shows the standard deviation plotted against the average signal for a single image on the cluster 2 camera on a log-log scale. The solid line is fit to the data at signal levels greater than the read noise of the CCD. It has a slope equal to 0.4996 ± 0.0574 , which implies that the noise equals the square root of the signal times a gain factor. Thus, we are measuring a quantity that follows Poisson statistics, i.e., the photoelectrons in the streak tube. The x axis has units of CCD ADU. The dashed line is what would be expected if the streak tube photoelectrons were

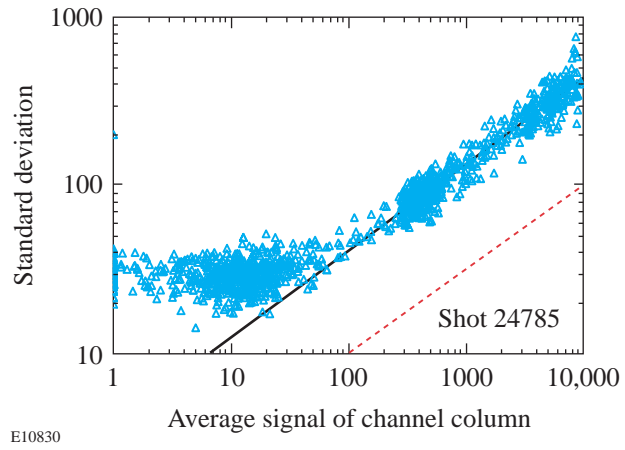


Figure 87.13

The standard deviation for 24×1 pixel regions on the cluster 2 streak camera. At signal levels above about 30 ADU, the signal obeys Poisson statistics. Below that level, the noise is dominated by a constant read noise in the CCD electronics. The solid line is a fit of the form $\ln(\text{std. dev.}) = Ae^{[B \ln(\text{signal})]}$, where $B \sim 0.5$, implying Poisson statistics. This represents the expected standard deviation if gain is removed from the system.

measured directly. The ratio or horizontal shift between the two lines is the gain of the system from streak tube photoelectrons to CCD ADU. In this case the gain is 19.2 ADU/photoelectron. In operation the optical signal was adjusted using the filters mentioned above to produce the maximum tube current that would not introduce distortion at the peak of the optical pulse. Under these conditions, the peak tube current produced 9000 CCD ADU per pixel on the cluster 2 camera. Inserting this value into the fitted equation, we find the ratio of the signal to the standard deviation at the peak to be 36. Since 24 pixels are averaged, the signal-to-noise ratio, defined as the signal times the square root of the number of averaged points divided by the standard deviation, is about 100. The signal-to-noise ratio and the peak current varied somewhat from camera to camera. The averaging time for this measurement is 12 ps. The signal-to-noise ratio drops to 1 at a signal level of 6.2 ADU.

From Fig. 87.13 the dynamic range can be estimated. At the peak, the total signal is 9000 ADU, so the dynamic range is about $9000/6.2 = 1453$. The noise floor is the signal level where the SNR = 1 times the number of rows in a column divided by the gain, which gives a noise level of 7 photoelectrons. The noise is equivalent to about 0.3 photoelectrons per pixel. The power-balance specification for OMEGA, as well as for the NIF, requires a minimum acceptable bandwidth of 3 GHz, which corresponds to a resolution element of about 100 ps or about eight columns, so the dynamic range would increase to about 4.1×10^3 . Quoting a dynamic range, however, is misleading. It is more important to state how the dynamic range is defined in terms of the signal-to-noise ratio. The signal-to-noise ratio is not constant over the dynamic range, and it is possible to have a very large dynamic range with a very small signal-to-noise ratio at the peak. The lower end of the dynamic range is defined as the point where the signal-to-noise ratio is equal to 1 for 12-ps averaging. At the high end of the range, tube current is just below the distortion level and the signal-to-noise ratio varies from 90:1 to 110:1. Thus at the peak of the optical pulse, measurements can be made with about 1.0% accuracy. At intensities equal to 1% and 10% of peak, the respective signal-to-noise ratios are approximately 2.3% and 7.1%. If the pulse shape being measured has regions of temporally uniform intensity, it is possible to average over longer times and get better accuracy; however, this cannot be done in regions where the pulse shape is rapidly changing in time. At the peak of this pulse the average rms error was 1.0%, which is less than the 5% error budget allotted to each beam for establishing the 1% irradiation uniformity required by OMEGA. On the rising edge, the beam timing is usually determined by the 2% threshold level. Here the signal had a 30% rms error.

Dividing the error in the power by the derivative of the power with respect to time, the error in determining the 2% point was found to be less than one CCD superpixel. These measurements show that this streak camera-based optical power measurement system is meeting the power-balance requirements of the OMEGA laser system, and in its present configuration it exceeds the specifications for the proposed NIF power-balancing system.

It is instructive to look at a single beamline to gauge how well it can be characterized. Figure 87.14 shows a beamline with a nominal, 1-ns flattop pulse with SSD. The measured pulse shape showed that both 3- and 10-GHz modulations were present. This indicated that some of the SSD bandwidth was being clipped in the amplifiers or tripling crystals. This analysis

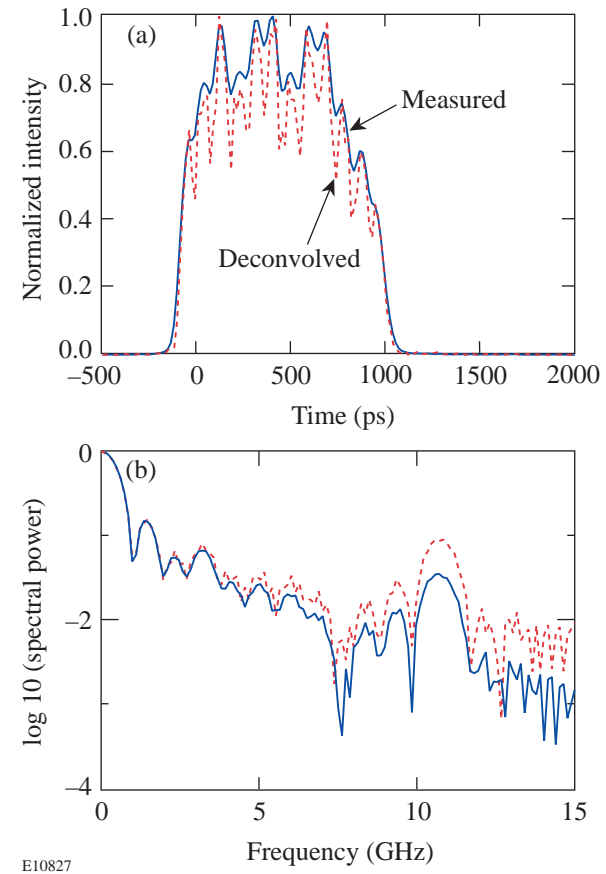


Figure 87.14
(a) The bandwidth limitation of the streak camera masks the true modulation on the pulse (solid curve). Using the measured response of the streak camera to the effects of focusing and the optical fibers, it is possible to deconvolve the bandwidth limitations (dashed curve). (b) Taking the FFT of the traces in (a), the modulation at 10 GHz is found to be three times greater in the deconvolved data than in the raw data.

sis did not take into account the bandwidth limitation of the optical-fiber bundle or the electron focusing optics discussed above. The impulse function of the camera was calculated by convolving the impulse response of the fiber bundle with the measured line spread of the focus image (see Fig. 87.8) mapped onto the sweep-speed time base. Deconvolving both of these responses from the measured signal indicated that the modulation at 10 GHz was three times higher than was being displayed.

Figure 87.15 illustrates how the streak cameras measure the power balance on the OMEGA system. The solid curve represents the normalized average pulse shape. All the beams recorded on the shot were mapped onto a uniform time base, temporally aligned, and averaged together pointwise for one of the standard OMEGA pulse shapes. The standard deviation was also calculated at each point and divided by the average, giving the dashed curve in Fig. 87.15, which is the percent of imbalance at any given time. Near the peak of the pulse, the power imbalance drops below 5%, which is the goal of the OMEGA system. The single-beam measurements indicate that the peak power of any given beamline is known with an accuracy of 1.0%. In the foot portion of the pulse, where the power is 15% to 20% of the peak, the imbalance in the system is about 10%. Here, depending on which camera is used, the single-beam measurements indicate that the power can be measured with 2% to 4% accuracy. Thus, at both the foot and the peak of this particular pulse shape, the single-beam mea-

surements have a smaller error than the measured beam-to-beam imbalance. As a result we have an instrument that can measure power balance on the OMEGA system and provide feedback to the engineering staff. This information can be used to modify the system, which will improve power balance. It should also be noted how well the average pulse shape of the system can be characterized. When the average shape falls to 0.1% of the peak, the average imbalance or percent error in the signal goes to 100%, implying that the SNR equals 1; thus the average pulse shape is well characterized over a 1000:1 range of powers.

Conclusion

The design and operation of a multiplexed streak camera system have been described. The unique feature of this system is its built-in self-calibration ability. The geometric distortions, flat field, and sweep speed of each channel can be measured and adjusted on a routine basis. By maintaining a strict regime of weekly calibrations, accurate power-balance measurements on the OMEGA laser can be obtained. Over 12-ps time intervals, a single beam can be measured with 1.0% accuracy; the beam-to-beam power imbalance has been measured at less than 5%. The timing of the beams can be measured to 7-ps rms. This set of high-precision instruments is proving very useful in establishing power balance on the 60-beam OMEGA laser.

ACKNOWLEDGMENT

This work was supported by the U.S. Department of Energy Office of Inertial Confinement Fusion under Cooperative Agreement No. DE-FC03-92SF19460, the University of Rochester, and the New York State Energy Research and Development Authority. The support of DOE does not constitute an endorsement by DOE of the views expressed in this article.

REFERENCES

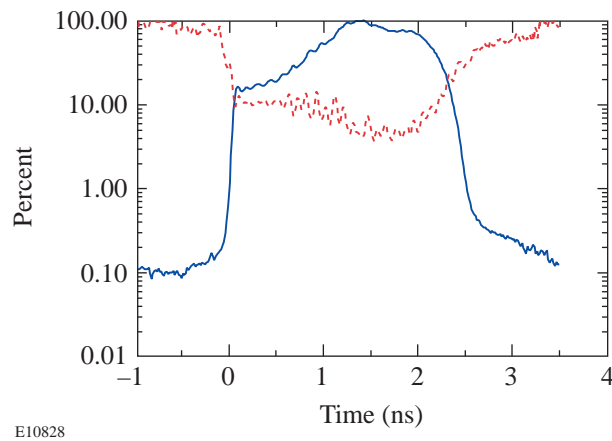


Figure 87.15

The solid curve is the average pulse shape for OMEGA shot 22708 normalized to 100% UV power at the peak averaged over 50 beams. The dashed curve is the measured standard deviation at each point across 50 beams.

1. T. R. Boehly, R. S. Craxton, T. H. Hinterman, P. A. Jaanimagi, J. H. Kelly, T. J. Kessler, R. L. Kremens, S. A. Kumpan, S. A. Letzring, R. L. McCrory, S. F. B. Morse, W. Seka, S. Skupsky, J. M. Soures, and C. P. Verdon, *Fusion Technol.* **26**, 722 (1994).
2. J. M. Soures, R. L. McCrory, C. P. Verdon, A. Babushkin, R. E. Bahr, T. R. Boehly, R. Boni, D. K. Bradley, D. L. Brown, R. S. Craxton, J. A. Delettrez, W. R. Donaldson, R. Epstein, P. A. Jaanimagi, S. D. Jacobs, K. Kearney, R. L. Keck, J. H. Kelly, T. J. Kessler, R. L. Kremens, J. P. Knauer, S. A. Kumpan, S. A. Letzring, D. J. Lonobile, S. J. Loucks, L. D. Lund, F. J. Marshall, P. W. McKenty, D. D. Meyerhofer, S. F. B. Morse, A. Okishev, S. Papernov, G. Pien, W. Seka, R. Short, M. J. Shoup III, M. Skeldon, S. Skupsky, A. W. Schmid, D. J. Smith, S. Swales, M. Wittman, and B. Yaakobi, *Phys. Plasmas* **3**, 2108 (1996).
3. A. Okishev, M. D. Skeldon, S. A. Letzring, W. R. Donaldson, A. Babushkin, and W. Seka, in *Superintense Laser Fields*, edited by A. A. Andreev and V. M. Gordienko (SPIE, Bellingham, WA, 1996), Vol. 2770, pp. 10–17.

4. D. K. Bradley, J. A. Delettrez, R. Epstein, R. P. J. Town, C. P. Verdon, B. Yaakobi, S. Regan, F. J. Marshall, T. R. Boehly, J. P. Knauer, D. D. Meyerhofer, V. A. Smalyuk, W. Seka, D. A. Haynes, Jr., M. Gunderson, G. Junkel, C. F. Hooper, Jr., P. M. Bell, T. J. Ognibene, and R. A. Lerche, *Phys. Plasmas* **5**, 1870 (1998).
5. W. R. Donaldson, R. Boni, R. L. Keck, and P. A. Jaanimagi, in *Optical Pulse and Beam Propagation*, edited by Y. B. Band (SPIE, Bellingham, WA, 1999), Vol. 3609, pp. 121–127.
6. S. P. Regan, J. A. Marozas, J. H. Kelly, T. R. Boehly, W. R. Donaldson, P. A. Jaanimagi, R. L. Keck, T. J. Kessler, D. D. Meyerhofer, W. Seka, S. Skupsky, and V. A. Smalyuk, *J. Opt. Soc. Am. B* **17**, 1483 (2000).
7. S. W. Thomas *et al.*, in *Solid State Lasers for Applications to Inertial Confinement Fusion: Second Annual International Conference*, edited by M. L. Andre (SPIE, Bellingham, WA, 1997), Vol. 3047, pp. 700–706.
8. J. Chang *et al.*, in *Digest of Technical Papers, Fifth IEEE Pulsed Power Conference*, edited by P. J. Turchi and M. F. Rose (IEEE, New York, 1985), pp. 1–4.
9. R. A. Lerche, D. S. Montgomery, and J. D. Wiedwald, in *Ultrahigh- and High-Speed Photography, Videography, and Photonics '91*, edited by P. A. Jaanimagi (SPIE, Bellingham, WA, 1992), Vol. 1539, pp. 68–75.
10. G. A. Kyrala *et al.*, *Rev. Sci. Instrum.* **68**, 664 (1997).
11. A. V. Okishev, R. Boni, M. Millecchia, P. A. Jaanimagi, W. R. Donaldson, R. L. Keck, W. Seka, K. V. Dukelsky, M. A. Eronyan, V. S. Shevandin, G. A. Ermolaeva, G. Nikolaev, and V. B. Shilov, “Unique High-Bandwidth, UV Fiber Delivery System for the OMEGA Diagnostic Applications,” to be published in the IEEE Journal on Selected Topics in Quantum Electronics.
12. Laboratory for Laser Energetics LLE Review **73**, 6, NTIS document No. DOE/SF/19460-212 (1997). Copies may be obtained from the National Technical Information Service, Springfield, VA 22161.
13. E. L. Hall, *Computer Image Processing and Recognition*, Computer Science and Applied Mathematics (Academic Press, New York, 1979), pp. 186–188.
14. Laboratory for Laser Energetics LLE Review **63**, 110, NTIS document No. DOE/SF/19460-91 (1995). Copies may be obtained from the National Technical Information Service, Springfield, VA 22161.

Evolution of Shell Nonuniformities Near Peak Compression of a Spherical Implosion

Introduction

In inertial confinement fusion (ICF), a spherical target is imploded by either direct illumination of laser beams (direct drive)¹ or x rays produced in a high-Z enclosure (hohlraum).² Target perturbations can result from imperfections in the target itself or from drive nonuniformities. In direct-drive ICF, these include imprinted modulations from laser nonuniformities. These target perturbations can be amplified by hydrodynamic instabilities to disrupt the implosion and degrade target performance. The unstable growth of target perturbations has been extensively studied in planar geometry with preimposed modulations using indirect drive^{3,4} and both preimposed and imprinted modulations using direct drive.^{5–8} Experiments in cylindrical⁹ and spherical¹⁰ geometry have studied effects of convergence on the unstable growth. The modulation growth is typically measured by backlighting the driven target with x rays.¹¹ The backscatterer x rays are attenuated while passing through the target, allowing measurements of the target-areal-density modulations.

Near peak compression in a spherical-target implosion, when the maximum density and temperature occur, the hot, compressed core and inner surface of the shell produce strong x-ray emission. These emissions can be used as a backscatterer to probe the outer, colder shell.¹² The first shell-integrity measurements based on this method were time integrated over the duration of peak compression (~200 to 300 ps) of the implosion.^{12,13} They used shells with titanium-doped layers and imaging at photon energies above and below the titanium *K* edge. Core images at photon energies below the *K* edge (not absorbed by the shell) provide the spatial shape of the backscatterer, while core images at photon energies above the *K* edge (highly absorbed by the shell's titanium) contain information about the structure of shell-areal-density modulations in the titanium-doped layer.

The experiment described in this article, based on the techniques developed in time-integrated experiments,^{12,13} is the first measurement of the evolution of shell nonuniformities near peak compression of a spherical-target implosion using

targets with titanium-doped layers. The growth of shell modulations in the deceleration phase is measured for the first time in ICF implosion experiments. The core emission, temperature, and shell-areal-density histories are also measured. Areal-density modulations in a titanium-doped layer have been determined from the intensity ratios of time-resolved, two-dimensional (2-D) core images taken above and below the titanium *K* edge. The average areal density has been measured using streak spectroscopy of titanium absorption of core radiation above the titanium *K* edge.

Experimental Configuration

Spherical targets with an initial diameter of about 920 μm filled with 15 atm of D₂ gas were imploded using direct-drive, 351-nm laser illumination on the 60-beam OMEGA laser system.¹⁴ The pulse shape was a 1-ns square with total on-target energy of about 23 kJ. The target shells had 1.9- μm -thick, titanium-doped (6% by atom) CH inner layers and ~18- μm -thick, pure-CH outer layers. The initial areal density of titanium in the shell was about 0.05 mg/cm². All laser beams were smoothed with distributed phase plates (DPP's);¹⁵ 1-THz, 2-D smoothing by spectral dispersion (2-D SSD);¹⁶ and polarization smoothing (PS)¹⁷ using birefringent wedges. The average beam-to-beam energy imbalance was about 3.8%. The target emission was imaged on a four-strip framing camera^{18,19} by a 6- μm -diam pinhole array, protected by a 200- μm -thick beryllium filter. The upper two strips of the framing camera were filtered with a 75- μm -thick titanium filter, and the lower two strips by a 50- μm -thick iron filter to image core radiation at photon energies below (~4.8 keV) and above (~6.5 keV) the titanium *K* edge (4.966 keV), simultaneously.¹⁹ The two x-ray energy channels had spectral bandwidths ($\Delta E/E$) of about 20%. Each image taken with the framing camera had a temporal resolution of ~40 ps and a spatial resolution of about 6 μm . The framing camera output was captured on a charge-coupled-device (CCD) camera with a 9- μm pixel size²⁰ and a magnification of 12.

The spectral evolution of the core emission was captured on an x-ray streak camera²¹ with a temporal resolution of ~20 ps.

The streaked spectrum was calibrated by a time-integrated spectrum measured with an ammonium di-hydrogen phosphate (ADP) crystal. Figure 87.16 shows a spectral evolution of core emission as a function of photon energy near peak compression (~2.0 ns) for one of the three similar shots, integrated over the core size for times 1.77, 1.82, 1.92 ns [Fig. 87.16(a)], and 1.97, 2.02, 2.07 ns [Fig. 87.16(b)]. Core images for the same six times on the same shot captured with the framing camera are shown in Fig. 87.17, with the upper six images corresponding to photon energy channel below the titanium *K* edge, and the lower six images to the channel above the *K* edge. These images have each been normalized to their highest intensities.

The measured spectra shown in Fig. 87.16 contain information about (1) the evolution of He _{α} , H _{α} and He _{β} line emission of titanium ions mixed with the core fuel, (2) 1s–2p absorption lines (near ~4.6 keV) of warm titanium with temperatures

$T \sim 500$ to 700 eV in the shell, (3) absorption above the *K* edge (at 4.966 keV) of cold titanium ($T < 500$ eV) in the shell,^{12,13} and (4) hot core continuum emission. The effective electron temperature in the emission region T_e and average cold titanium areal density have been calculated by fitting the function

$$I(E) = I_0 e^{\{-E/T_e - \mu_{Ti}(E) \cdot [\rho d]_{Ti}\}}$$

to the measured spectra (outside the absorption area of warm titanium near ~4.6 keV, and the shifting *K* edge), where E is the photon energy, $\mu_{Ti}(E)$ and $[\rho d]_{Ti}$ are the cold titanium mass absorption coefficient and average areal density, respectively, and I_0 is the constant. The effect of CH absorption was negligible compared to titanium absorption in these experiments because all time-resolved images below and above the *K* edge were always identical within experimental noise in shots with CH-only shells (containing no titanium) taken at similar drive conditions.

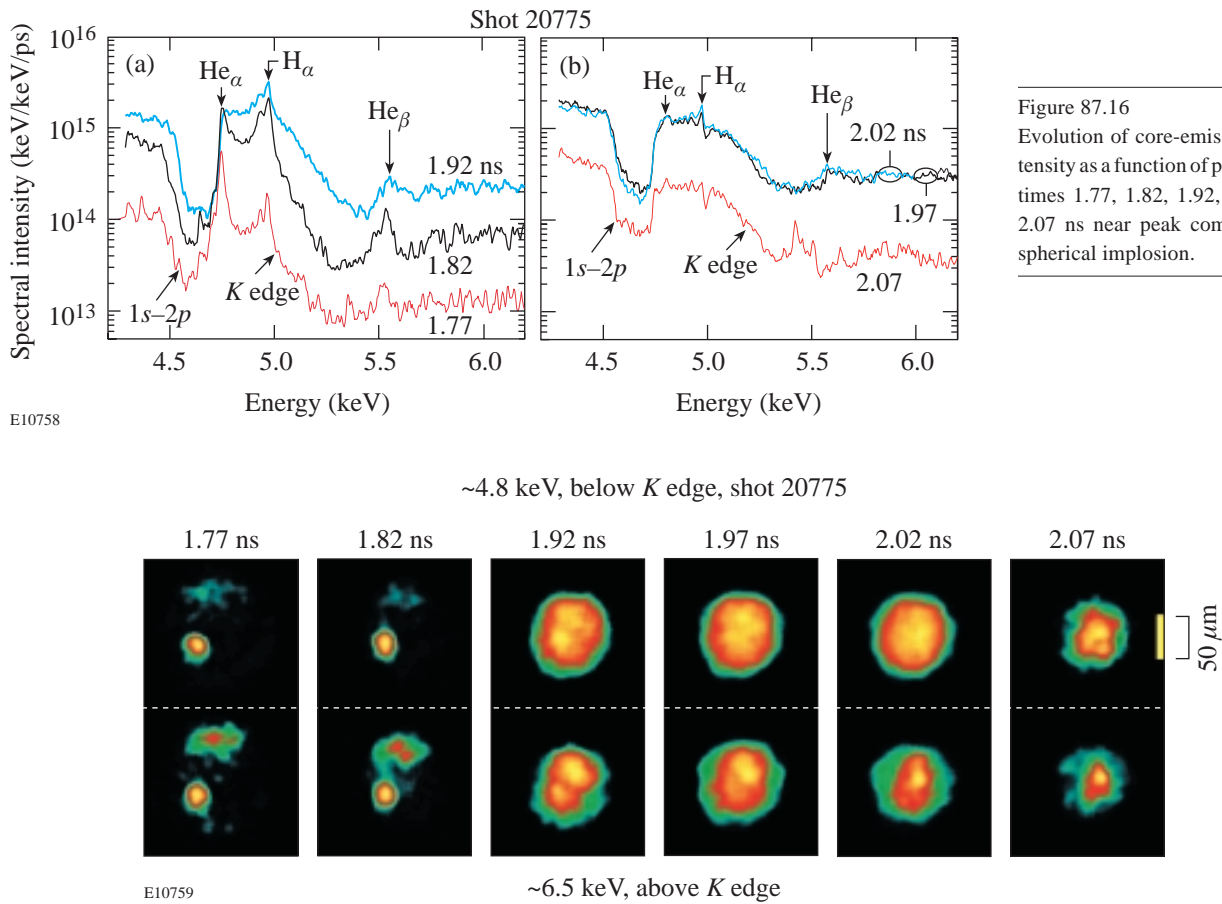


Figure 87.16
Evolution of core-emission spectral intensity as a function of photon energy for times 1.77, 1.82, 1.92, 1.97, 2.02, and 2.07 ns near peak compression of the spherical implosion.

Figure 87.17

“Raw” core images near peak compression at energies below (~4.8 keV, upper row of images) and above (~6.5 keV, lower row of images) the titanium *K* edge for times 1.77, 1.82, 1.92, 1.97, 2.02, and 2.07 ns.

Figure 87.18 shows a temporal evolution of the electron temperature T_e of the core and the shell-emitting regions [circles connected by a thin solid line in Fig. 87.18(a)] and areal density of the cold titanium in the shell [ρd]_{Ti} [triangles connected by a thin solid line in Fig. 87.18(b)]. The measured areal density of titanium has been normalized to the initial titanium areal density of the undriven target and represents the amount of compression in the layer. The thick solid lines in Figs. 87.18(a) and 87.18(b) show the evolution of continuum emission intensity in arbitrary units at photon energies of 4.8 to 4.9 keV below the titanium K edge. These were calculated using core emission spectra measured with the streak camera. The diamonds in Figs. 87.18(a) and 87.18(b) show the intensity evolution (in arbitrary units) for the six images (Fig. 87.17) measured with the framing camera, also below the titanium K edge.

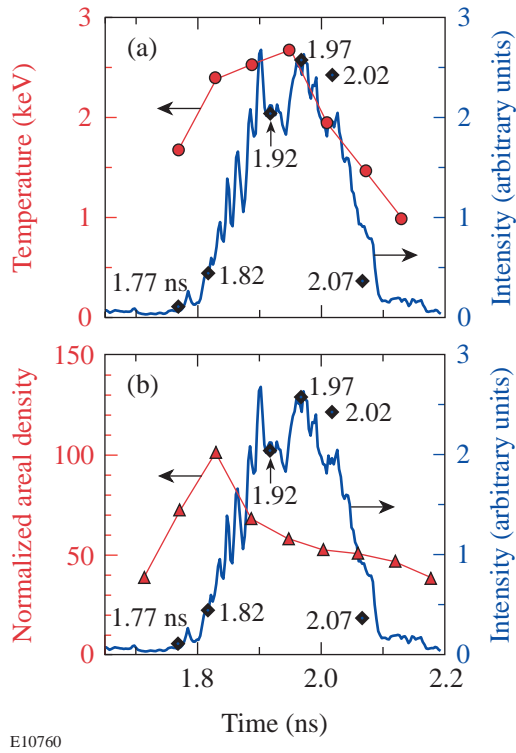


Figure 87.18
 (a) Evolution of core continuum emission temperature (circles), core continuum emission intensity (at 4.8 to 4.9 keV, thick solid line), and emission intensity in images below the K edge (diamonds) for the same times as in Fig. 87.17. (b) Evolution of normalized areal density of titanium (triangles) together with core continuum emission intensity and emission intensity in images below the K edge from (a).

The modulations in the cold, or absorbing, part of the shell areal density $\delta[\rho d](\mathbf{r},t)$ at time t (\mathbf{r} is the spatial coordinate) are proportional to the modulation in the logarithm of the ratio of intensities of the two images at photon energies above (highly absorbing by the shell) $I_{>K}(\mathbf{r},t)$ and below (weakly absorbing by the shell) the titanium K edge, $I_{<K}(\mathbf{r},t)$:

$$\delta[\rho d](\mathbf{r}) = \frac{\delta \{ \ln[I_{<K}(\mathbf{r})/I_{>K}(\mathbf{r})] \}}{(\mu_{>K} - \mu_{<K})}, \quad (1)$$

where $\mu_{>K} = 0.37 \pm 0.02 \text{ cm}^2/\text{mg}$ and $\mu_{<K} = 0.11 \pm 0.02 \text{ cm}^2/\text{mg}$ are the spectrally weighed mass absorption coefficients of cold titanium at photon energies above and below the K edge, respectively.¹³ The absorption coefficients have been calculated for each time t using the measured x-ray spectra shown in Fig. 87.16 and filter functions of beryllium, titanium, and iron filters.¹³ Images $I_{<K}(\mathbf{r},t)$ and $I_{>K}(\mathbf{r},t)$ have been obtained from “raw” images (shown in Fig. 87.17) using the Wiener-filtering technique,^{13,19} which was based on the measured system resolution ($\sim 6 \mu\text{m}$)¹⁹ and the system noise (determined by the photon statistics of core x rays).¹⁹ All approximations and assumptions made in deriving Eq. (1) have been presented and discussed in detail in Refs. 12, 13, and 19.

Results and Discussion

Figure 87.19(a) shows the evolution of areal-density modulations calculated using core images at 1.92, 1.97, 2.02, and 2.07 ns, shown in Fig. 87.17 and Eq. (1), and normalized to their measured (with the streak camera) average areal densities, shown in Fig. 87.18(b). The images at early times 1.77 and 1.82 ns do not have sufficient backscatterer area (first two images at $\sim 4.8\text{-keV}$ channel) to probe the nonuniformities in the cold shell. The spatial scale of modulations decreases from time 1.92 ns to time 2.02 ns (as evident from the motion of the red “circular” structure in corresponding images), and then shorter-scale modulations start to grow in the image at 2.07 ns. The image size at 2.07 ns is smaller than images at early times because the level of backscatterer emission drops late in the implosion. The effect of titanium line emission on the spatial shape of images below the K edge was negligible because core images, routinely measured with a pinhole-array spectrometer,¹² always had the same spatial shapes at photon energies of titanium (He_{α} , H_{α}) lines and photon energies outside these lines below the K edge. The minimum level of modulations with $\sigma_{\text{rms}} = 18 \pm 8\%$ occurs near 2.0 ns. The modulation σ_{rms} decreases by about 20% from time 1.92 ns to time 2.02 ns,

when the maximum core emission intensity and temperature occur (see Fig. 87.18); then it grows by about 60% during decompression while emission intensity and temperature drop.

The shell modulation level at peak compression depends on the initial modulation level at the beginning of the implosion and the amount of unstable growth during implosion. In direct-drive ICF the initial target modulations come primarily from the imprinting^{5–8} of laser-beam nonuniformities. Beam-smoothing techniques such as DPP's,¹⁵ SSD,¹⁶ and PS¹⁷ are applied on OMEGA¹⁴ to minimize initial target modulations. To check the sensitivity of shell modulations at peak compression to the initial target modulations, two implosions with similar targets and drive conditions but with different levels of beam smoothing are compared: one shot was taken at best smoothing conditions, including 1-THz, 2-D SSD and PS; the other shot had 3-color-cycle, 0.35-THz, 2-D SSD and no PS. Figure 87.19(b) compares minimum levels of shell modulations near peak compression for these two shots. The level of shell modulation is significantly higher with less-uniform drive using 0.35-THz SSD and no PS ($\sigma_{\text{rms}} = 43 \pm 12\%$) than with 1-THz SSD and PS ($\sigma_{\text{rms}} = 18 \pm 9\%$). Implosions driven with more-uniform beams (1-THz SSD and PS) have primary neutron yields and fuel areal densities ~70% higher than with 0.35-THz SSD and no PS.²²

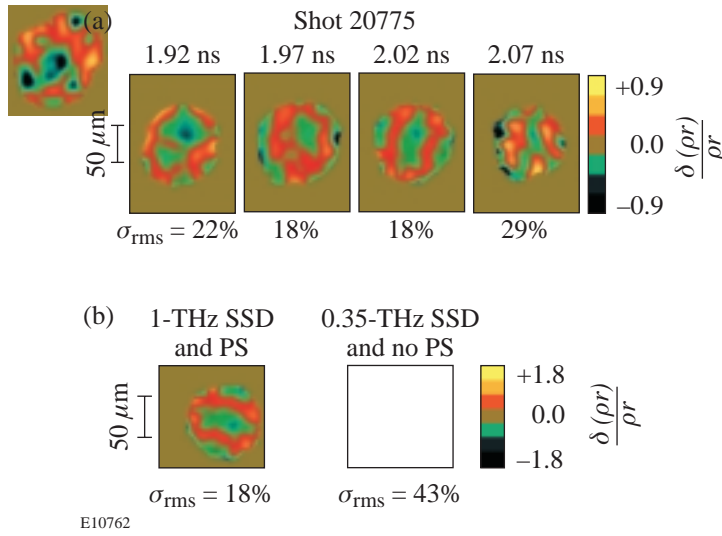


Figure 87.19
(a) Normalized areal-density modulations at 1.92, 1.97, 2.02, and 2.07 ns for shot 20775. (b) Normalized areal-density modulations for two shots: one with 1-THz SSD and PS from (a) at 2.02 ns; the other at peak compression with 3-color-cycle, 0.35-THz SSD and no PS.

A spherical-implosion postprocessor²³ to the one-dimensional (1-D) hydrocode *LILAC*²⁴ was applied to qualitatively explain the experimental data. This postprocessor uses a sharp-boundary model to study the perturbation evolution in the shell. During the acceleration phase of implosion, when the shell is driven by the laser beams, the shell nonuniformities grow due to the Rayleigh–Taylor (RT) instability.^{2–10} When the 1-ns laser drive is turned off, the shell slows down while converging inward to the target center, stops at stagnation, and then moves outward. Since the higher-density shell is slowed down by the lower-density D₂ gas, the inner surface of the shell is subject to the RT instability during the deceleration phase. The shell-areal-density modulation (the quantity measured in the experiment) can be written in the following form: $\delta(\rho d) \approx \pi\eta_f + \pi\eta_b$, where ρ is the average shell density, η_f and η_b are the amplitudes of the front- and back-surface distortions, and d is the shell thickness. During the shell acceleration, when the front surface is RT unstable, the first term $\rho\eta_f$ gives the dominant contribution to $\delta(\rho d)$. In addition, the front-surface perturbations feed through the shell ($\eta_b \sim \eta_f e^{-kd}$, where k is the modulation wave number), seeding the deceleration-phase RT instability on the inner surface. After the laser is turned off and the shell starts to decelerate, the ablation front becomes stable and perturbation η_f oscillates. One can estimate the period of such oscillations $T \sim 2\pi\sqrt{R/(\ell g)}$, where $R \approx 60 \mu\text{m}$ is the shell radius, ℓ is the mode number, and $g \approx 10^3 \mu\text{m/ns}$ is the deceleration. Substituting results of the 1-D *LILAC*²⁴ simulation to the above formula gives $T = 600 \text{ ps}$ for the dominant in the experiment mode $\ell = 6$ (which corresponds to a modulation wavelength of about 60 μm). Therefore, during the time of measurement $\Delta t = 300 \text{ ps}$, the front-surface modulation changes its sign. Thus, there are two competing effects: first, the reduction of front-surface modulations $\eta_f \sim \eta_0 \cos(2\pi t/T)$ due to phase change, and, second, an increase in back-surface modulations $\eta_b \sim \eta_0 \exp(\gamma t - kd)$ due to the RT growth, where γ is the instability growth rate. Initially, $\eta_f > \eta_b$, and the reduction in the front-surface amplitude leads to the reduction in the areal-mass modulation. Later, when η_b becomes dominant, growth in shell-areal-density modulation $\delta(\rho d)$ is caused by the exponential growth of the back-surface modulation. An additional reduction in cold $\delta(\rho d)$ could be due to the heating of the inner titanium-doped layer of the shell.

Figure 87.20(a) shows the profiles of target density and temperature in the deceleration phase of the implosion at peak compression (simulated by the 1-D code *LILAC*). The bulk of the shell is dense and relatively cold with an electron temperature less than 1 keV, while the core is hotter and less dense. The

solid line in Fig. 87.20(b) shows the evolution of shell-areal-density modulations calculated with the model for the dominant mode $\ell = 6$ based on the 1-D LILAC simulation. The modulations of total shell areal density $\delta(\rho d)$ decrease, while they are dominated by sinusoidally decreasing modulations at the outer surface. When exponentially growing modulations at the inner surface become higher than outer-surface modulations, the total shell-areal-density modulations grow. The circles in Fig. 87.20(b) show that σ_{rms} of measured shell-areal-density modulations [shown in Fig. 87.19(a)] follows the model prediction well. The results of the model were normalized to experimental point at $t = 1.97$ ns. The experimental points have been averaged using data from three shots taken at similar conditions. Since the measured spectrum of shell-areal-density modulations is located in the vicinity of the mode

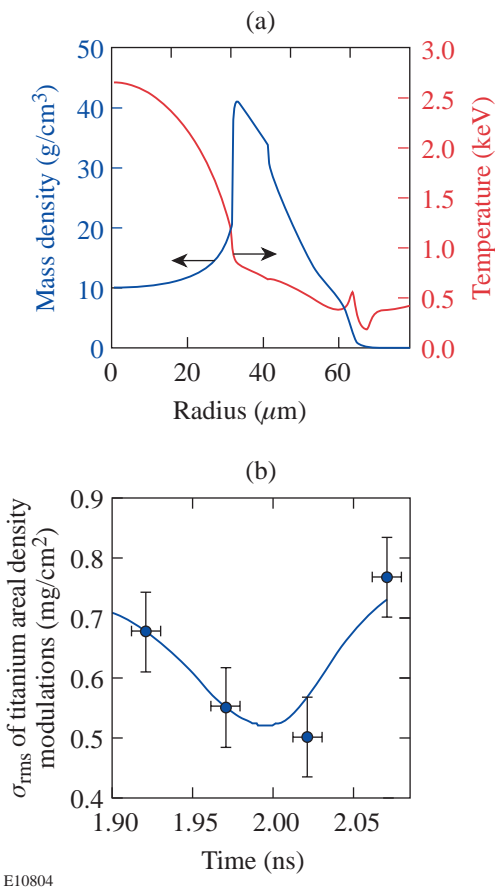


Figure 87.20

(a) The simulated profiles of target density and temperature during the deceleration phase of the implosion. (b) The evolution of titanium areal-density modulations in the shell calculated by the model (solid line) and measured (circles).

$\ell = 6$ (similar to previous time-integrated measurements^{12,13}), the comparison of measured modulation σ_{rms} with the calculated amplitude of dominant spectral mode becomes qualitatively reasonable.

Figure 87.18 shows that average cold-shell areal density increases up to ~ 1.8 ns and then starts to decrease gradually while peak compression is measured to be near 2.0 ns. This indicates that some part of the inner shell mixes with the core fuel and/or heats up to ~ 2 keV when it stops absorbing core radiation at photon energies above the titanium K edge. Such an increase in shell temperature and the reduction of measured cold-shell areal density are expected in targets with titanium-doped layers because of the additional absorption of core radiation by titanium above the titanium K edge. As a result, the cold-shell average areal density and areal-density modulations may be reduced. This effect may be partially responsible for the decrease of measured areal-density modulations [shown in Fig. 87.20(b)] for times up to ~ 2.0 ns. The increase of measured areal-density modulation after 2.0 ns, however, should be due to the unstable RT growth in the deceleration phase of the implosion, as predicted by the model.

Conclusion

The evolution of shell modulations near peak compression of a spherical implosion has been presented. The minimum level of areal-density modulations, with $\sigma_{\text{rms}} = 18\%$, occurs at the peak of core emission with a laser drive that included 1-THz SSD and PS. In implosions using the less-uniform irradiation produced by 3-color-cycle, 0.35-THz SSD and no PS, the level of modulations was significantly higher, with $\sigma_{\text{rms}} = 43\%$. The level of measured shell-areal-density modulations decreases when it is dominated by the decreasing modulations at the stable outer surface, then increases when it is dominated by growing modulations at the unstable inner surface, as expected.

ACKNOWLEDGMENT

This work was supported by the U.S. Department of Energy Office of Inertial Confinement Fusion under Cooperative Agreement No. DE-FC03-92SF19460, the University of Rochester, and the New York State Energy Research and Development Authority. The support of DOE does not constitute an endorsement by DOE of the views expressed in this article.

REFERENCES

1. J. Nuckolls *et al.*, *Nature* **239**, 139 (1972).
2. J. D. Lindl, *Inertial Confinement Fusion: The Quest for Ignition and Energy Gain Using Indirect Drive* (Springer-Verlag, New York, 1998), Chap. 6, pp. 61–82.

3. S. G. Glendinning, S. N. Dixit, B. A. Hammel, D. H. Kalantar, M. H. Key, J. D. Kilkenny, J. P. Knauer, D. M. Pennington, B. A. Remington, R. J. Wallace, and S. V. Weber, Phys. Rev. Lett. **78**, 3318 (1997).
4. M. M. Marinak *et al.*, Phys. Rev. Lett. **80**, 4426 (1998).
5. C. J. Pawley *et al.*, Phys. Plasmas **6**, 565 (1999).
6. H. Azechi *et al.*, Phys. Plasmas **4**, 4079 (1997).
7. R. J. Taylor *et al.*, Phys. Rev. Lett. **76**, 1643 (1996).
8. D. H. Kalantar, M. H. Key, L. B. Da Silva, S. G. Glendinning, B. A. Remington, J. E. Rothenberg, F. Weber, S. V. Weber, E. Wolfrum, N. S. Kim, D. Neely, J. Zhang, J. S. Wark, A. Demir, J. Lin, R. Smith, G. J. Tallents, C. L. S. Lewis, A. MacPhee, J. Warwick, and J. P. Knauer, Phys. Plasmas **4**, 1985 (1997).
9. D. L. Tubbs, C. W. Barnes, J. B. Beck, N. M. Hoffman, J. A. Oertel, R. G. Watt, T. Boehly, D. Bradley, P. Jaanimagi, and J. Knauer, Phys. Plasmas **6**, 2095 (1999).
10. S. G. Glendinning *et al.*, Phys. Plasmas **7**, 2033 (2000).
11. S. G. Glendinning *et al.*, in *Applications of Laser Plasma Radiation II*, edited by M. C. Richardson and G. A. Kyrala (SPIE, Bellingham, WA, 1995), Vol. 2523, pp. 29–39.
12. B. Yaakobi, V. A. Smalyuk, J. A. Delettrez, F. J. Marshall, D. D. Meyerhofer, and W. Seka, Phys. Plasmas **7**, 3727 (2000).
13. V. A. Smalyuk, B. Yaakobi, J. A. Delettrez, F. J. Marshall, and D. D. Meyerhofer, Phys. Plasmas **8**, 2872 (2001).
14. T. R. Boehly, D. L. Brown, R. S. Craxton, R. L. Keck, J. P. Knauer, J. H. Kelly, T. J. Kessler, S. A. Kumpan, S. J. Loucks, S. A. Letzring, F. J. Marshall, R. L. McCrory, S. F. B. Morse, W. Seka, J. M. Soures, and C. P. Verdon, Opt. Commun. **133**, 495 (1997).
15. Y. Lin, T. J. Kessler, and G. N. Lawrence, Opt. Lett. **20**, 764 (1995).
16. S. P. Regan, J. A. Marozas, J. H. Kelly, T. R. Boehly, W. R. Donaldson, P. A. Jaanimagi, R. L. Keck, T. J. Kessler, D. D. Meyerhofer, W. Seka, S. Skupsky, and V. A. Smalyuk, J. Opt. Soc. Am. B **17**, 1483 (2000).
17. T. R. Boehly, V. A. Smalyuk, D. D. Meyerhofer, J. P. Knauer, D. K. Bradley, R. S. Craxton, M. J. Guardalben, S. Skupsky, and T. J. Kessler, J. Appl. Phys. **85**, 3444 (1999).
18. C. J. Pawley and A. V. Deniz, Rev. Sci. Instrum. **71**, 1286 (2000).
19. V. A. Smalyuk, T. R. Boehly, L. S. Iwan, T. J. Kessler, J. P. Knauer, F. J. Marshall, D. D. Meyerhofer, C. Stoeckl, B. Yaakobi, and D. K. Bradley, Rev. Sci. Instrum. **72**, 635 (2001).
20. R. E. Turner *et al.*, Rev. Sci. Instrum. **72**, 706 (2001).
21. D. H. Kalantar *et al.*, Rev. Sci. Instrum. **72**, 751 (2001).
22. D. D. Meyerhofer, J. A. Delettrez, R. Epstein, V. Yu. Glebov, V. N. Goncharov, R. L. Keck, R. L. McCrory, P. W. McKenty, F. J. Marshall, P. B. Radha, S. P. Regan, S. Roberts, W. Seka, S. Skupsky, V. A. Smalyuk, C. Sorce, C. Stoeckl, J. M. Soures, R. P. J. Town, B. Yaakobi, J. D. Zuegel, J. Frenje, C. K. Li, R. D. Petrasso, D. G. Hicks, F. H. Séguin, K. Fletcher, S. Padalino, M. R. Freeman, N. Izumi, R. Lerche, T. W. Phillips, and T. C. Sangster, Phys. Plasmas **8**, 2251 (2001).
23. V. N. Goncharov, P. McKenty, S. Skupsky, R. Betti, R. L. McCrory, and C. Cherfils-Clérouin, Phys. Plasmas **7**, 5118 (2000).
24. J. Delettrez and E. B. Goldman, Laboratory for Laser Energetics Report No. 36, University of Rochester (1976).

Multibeam Stimulated Brillouin Scattering from Hot Solid-Target Plasmas

Introduction

We report on the first multibeam laser-plasma interaction experiments with a critical density surface present at all times. Six interaction beams are incident on a preformed plasma, tailored to resemble future direct-drive-ignition laser fusion implosions. Stimulated Brillouin scattering (SBS) was observed using two full-aperture backscattering stations. The results show strong evidence of electromagnetic (EM) wave seeding of SBS backscatter and may also indicate strongly driven, common, symmetrically located ion waves. The latter could provide for efficient sidescattering that provides the EM seed for SBS backscattering. Quenching SBS before the peak of the interaction beam is seen in all the experiments. For NIF direct-drive ignition experiments the expected SBS levels are well below 1%.

The details of laser coupling to the hot coronal plasma of direct-drive inertial confinement fusion (ICF) targets are extremely important since the laser provides the drive energy for the implosion.¹ Measurement and understanding of power (or energy) loss due to SBS are essential. Over the past 30 years, many detailed reports^{2–12} of SBS experiments have been published; however, few, if any, have investigated conditions relevant to direct-drive ICF plasma implosions.⁴ In direct-drive implosions, many individual laser beams are overlapped on the target. This allows multibeam interactions that may change the SBS instability characteristics.^{13,14} In particular, SBS instability can grow from an EM wave seed provided by other beams reflected near the critical-density surface, or common (shared) ion waves can reduce the instability threshold. Previous multibeam SBS experiments^{3,15} have been performed in plasmas with peak densities significantly lower than critical density and are, thus, not directly applicable to direct-drive ICF conditions. Those experiments indicated a redistribution of the scattered light but no significant increase in the overall SBS losses.¹⁵

In future direct-drive-ignition experiments on the National Ignition Facility (NIF),¹⁶ the conditions most vulnerable to SBS will occur before the laser reaches its peak power¹ and

will correspond to plasmas with $T_e \gtrsim 2$ keV and density and velocity scale lengths of ~ 0.5 mm. These will be irradiated with 351-nm laser light with laser-beam smoothing¹⁷ by spectral dispersion (SSD) at ~ 1 THz and polarization smoothing (PS). The corresponding single-beam irradiation intensities are $\leq 10^{14}$ W/cm² (four beamlets, or one quad, of the NIF¹⁶).

The full plasma and intensity evolution of a NIF direct-drive implosion cannot be simulated with present laser systems, but a good approximation to the conditions that are most susceptible to SBS can be achieved using OMEGA. Past single-beam interaction experiments on OMEGA have shown that SBS is unlikely to represent a significant energy loss during the high-intensity portion of the NIF pulse.⁴ The present multiple-beam SBS experiments are the first reported in the literature with a critical-density surface present at all times and plasma conditions close to those expected on the NIF. Six interaction beams are symmetrically arrayed around the target normal. These interaction beams are overlapped on a plasma produced from a thick CH target by heater beams that strike the target in advance of the interaction beams.

Experiments

The experiments were carried out on the OMEGA laser system¹⁸ using a subset of its 60 UV (351-nm) beams. The experimental arrangement is shown schematically in Fig. 87.21. The CH targets were 100 μm thick and 5 mm in diameter (semi-infinite) with their normal pointed toward the center of the six symmetrically arranged interaction beams (see Figs. 87.21 and 87.22). These targets were sequentially irradiated with nine primary beams, followed in 1-ns intervals by six secondary heater beams and six interaction beams. The six interaction beams are identified with their beam numbers inside the circles in Fig. 87.22 and are located at $\sim 23^\circ$ to the target normal. The primary and secondary beams are at $\sim 62^\circ$ and 48° to the target normal, respectively.

All of the beams were equipped with distributed phase plates¹⁹ (DPP's) and were operated with 2-D SSD (1 THz) and PS.¹⁷ The phase plates in the primary and secondary beams

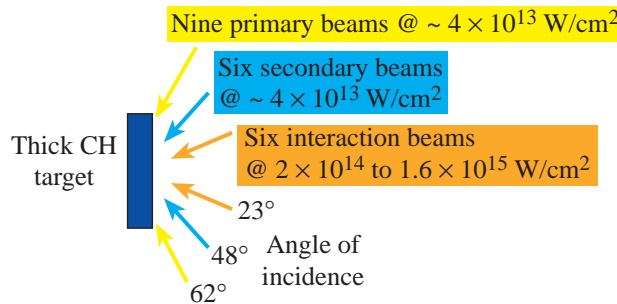
were standard OMEGA “SG3” phase plates (nominally Gaussian spots of 0.5-mm FWHM at best focus). These beams were defocused to produce a 2-mm-diam spot (~1-mm FWHM) with peak intensities (averaged over the speckle pattern) of $\sim 4 \times 10^{13} \text{ W/cm}^2$. Two alternative configurations were used on the six interaction beams: All were outfitted with either six standard phase plates with the target at best focus (nominal single-beam peak intensity of $2 \times 10^{14} \text{ W/cm}^2$) or three pairs of phase plates that produced smaller spots. In the latter case, the corresponding average single-beam peak intensities were 4, 8, and $16 \times 10^{14} \text{ W/cm}^2$. The beam energy for all shots was $\sim 365 \text{ J} (\pm 5\%)$. The laser pulse shapes were a close approximation of those shown schematically in Fig. 87.21, i.e., a 0.5-ns linear rise followed by a 0.9-ns flattop.

Similar preformed plasmas have been diagnosed extensively using time-resolved x-ray spectroscopy, time-resolved stimulated Raman scattering (SRS) spectroscopy,⁴ and schlieren photography.^{5,20} Those experiments have been simulated with the two-dimensional hydrodynamic code *SAGE*.²¹ Because

the *SAGE* simulations have generally closely replicated the measurements, we are confident that the *SAGE* predictions for the present experiments are equally valid: electron temperatures of ~ 2 to 3 keV with electron density and velocity scale lengths of ~ 1 mm.

Two full-aperture backscatter (FABS) stations were used to measure the SBS energies and the time-resolved SBS spectra. These stations collected the light propagated from the target in the direction opposite to the incoming high-energy beam path through the f/6 OMEGA focusing lens. This was accomplished using an uncoated, wedged, fused quartz optic ahead of the focusing lens. The arrangement allows the incoming high-energy beam to pass onward to the target while a full-aperture, reduced-energy sample of any outbound light is delivered to the FABS setup. Beams 25 and 30 (in Fig. 87.22) were instrumented in this manner. Within the FABS, the energies were measured with appropriately filtered and cross-calibrated calorimeters. The light for the time-resolved spectra was focused through an engineered diffuser (2° scattering angle)

(a) Beam geometry and intensity



(b) Pulse shape and timing of beam groups

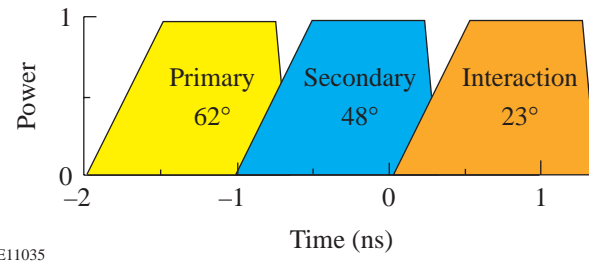


Figure 87.21

Schematic representation of solid-target illumination with three sets of laser beams. Pulse sequence, pulse shapes, and approximate angles of incidence are indicated. The irradiation intensity of each primary and secondary beam is $\sim 4 \times 10^{13} \text{ W/cm}^2$; the interaction-beam intensities vary from 2×10^{14} to $1.6 \times 10^{15} \text{ W/cm}^2$.

Beam number	25	30	12	23	14	50
$I_{14} (10^{14} \text{ W/cm}^2)$	4	16	4	8	16	8

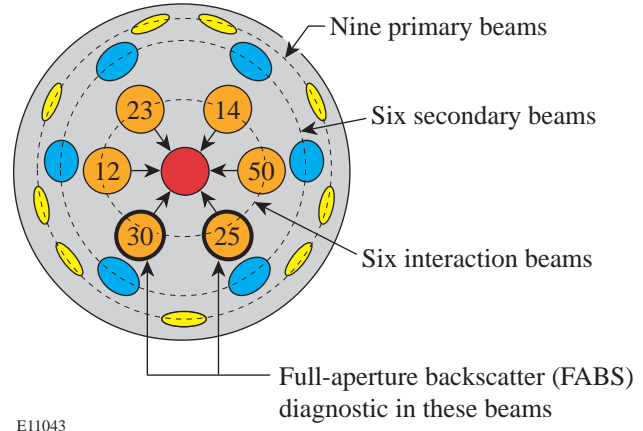


Figure 87.22

Schematic representation of the plasma-producing and interaction beams on the target chamber surface. The numbers inside the circles are the beam numbers for the interaction beams. Beams 25 and 30 are outfitted with full-aperture backscatter (FABS) stations. All beam energies are nominally 365 J. The intensities (in units of 10^{14} W/cm^2) shown in the boxes below the beam numbers result from three different sets of phase plates. Standard OMEGA phase plates also permitted interaction intensities of $2 \times 10^{14} \text{ W/cm}^2$ in any or all of the beams.

into 435- μm gradient-index fibers and sent to a 1-m grating spectrometer coupled to an S20 streak camera. The fibers from both FABS stations were time-multiplexed at the input to the spectrometer. The measured time resolution was 80 ps and the dynamic spectral resolution was $\sim 0.4 \text{ \AA}$.

Results

The multibeam, time-integrated SBS reflectivity is shown in Fig. 87.23 as a function of the interaction beam intensity. Data from both FABS stations are shown. The average peak intensities of the various interaction beams ranged from $2 \times 10^{14} \text{ W/cm}^2$ to $1.6 \times 10^{15} \text{ W/cm}^2$, depending on the phase plates used. The average peak intensity I_{95} is defined such that 95% of the laser energy has intensities at or below I_{95} . Thus, most shots yielded simultaneous multibeam backscatter data at two intensities. The squares in Fig. 87.23 represent through-the-lens reflectivities with all beams at nominal energy. The diamonds represent shots without interaction beams (e.g., without beam 25 for FABS25), while the circles represent shots without the beams opposing the interaction beams [beam 23 for FABS25, beam 14 for FABS30 (see Fig. 87.22)].

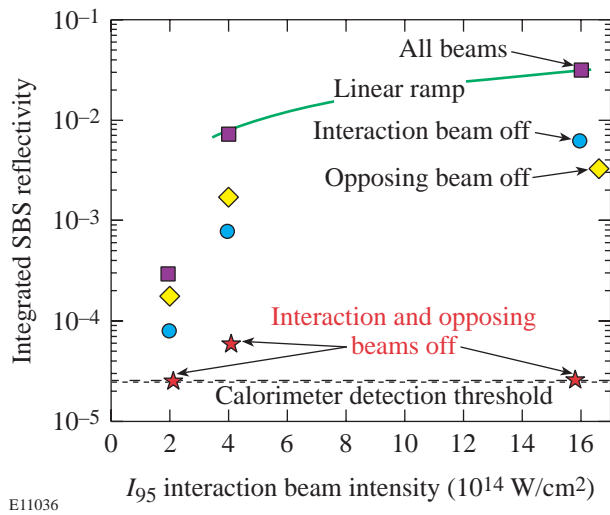


Figure 87.23

Multibeam, time-integrated SBS reflectivity measured by the calorimeters in two different locations (FABS25 and FABS30) for beam smoothing with 1-THz, 2-D SSD and PS. Squares represent measurements with all beams as indicated in Fig. 87.22, diamonds indicate shots without interaction beams (either beam 25 for FABS25 or beam 30 for FABS30), circles indicate shots without beams opposing the interaction beams (beam 23 for FABS25, beam 14 for FABS30). The stars indicate FABS energy measurements normalized to the mean beam energy with beams 25 and 23 (or 30 and 14) turned off. The linear ramp is shown to guide the eye and is indicative of saturation at intensities in excess of $\sim 3 \times 10^{14} \text{ W/cm}^2$. Each point plotted represents several actual shots with the shots clustered within the symbols shown.

The possible interplay and synergistic enhancement between specular reflection at the turning point, SBS sidescattering, and SBS backscattering are depicted in Fig. 87.24. Given the geometry of the interaction beams, the “opposing” beams (e.g., 23 and 14) are reflected at their respective turning points near the critical density ($n_e \sim 0.88 n_c$) and counter-propagate into beams 25 and 30. (Note: In this discussion, the term “opposing beam” means the beam on the opposite side of the circle of interaction beams. This is not the beam on the opposite side of the OMEGA target chamber that has a coincident optical axis, which was not used in these experiments.) These reflections can provide EM seed waves for SBS backscattering in beams 25 and 30. This is reminiscent of external EM-wave-seeding experiments by Baldis³ and Fernandez.⁶ In addition, the specular reflections can also provide EM seeds for SBS sidescattering in that direction.

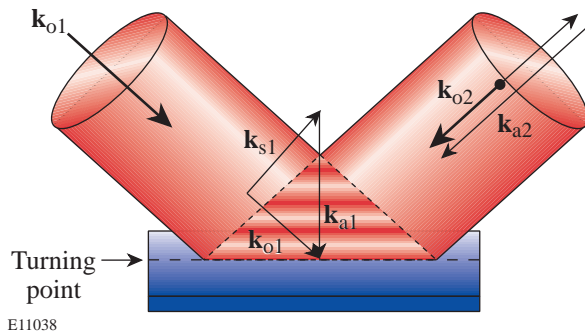


Figure 87.24

Schematic visualization of the interplay between SBS sidescattering and SBS backscattering on flat targets irradiated with symmetrically positioned interaction beams. The specular reflection at the turning point provides an EM seed for SBS sidescattering. That, in turn, provides an efficient EM seed for SBS backscattering of the “opposing” beam. These processes are most effective near the sonic point where the SBS wavelength shifts vanish.

The overall, multibeam reflectivities (squares in Fig. 87.23) saturate at a few percent for average irradiation intensities of 3 to $4 \times 10^{14} \text{ W/cm}^2$. Selectively turning off one of the interaction beams (beam 25 or 30—circles) or one of their opposing beams (beam 23 or 14—diamonds) leads to a significant drop in reflectivity. Furthermore, if both the interaction beam and its opposing beam are turned off, the residual reflectivities (stars) drop to the detection threshold for all but the point at $4 \times 10^{14} \text{ W/cm}^2$. For this point, the high-intensity beams 30 and 14 cause measurable sidescatter signal. For the other two intensities, the four remaining beams are too low in intensity to produce measurable SBS sidescattering into either

FABS25 or FABS30. Pure SBS backscattering for oblique incidence (circles) is observed if the beam opposing the interaction beam (e.g., beam 23) is turned off. In this case SBS grows from either noise or any existing seed (e.g., stars in Fig. 87.23).

The measured reflectivity in FABS25 is roughly twice that measured for pure backscattering when beam 25 is removed while the opposing beam 23 is left on. This signal (diamonds) represents SBS sidescattering of beam 23, which may be enhanced through ion-wave seeding by the symmetrically located ion waves produced by cooperative multibeam SBS side scattering from the other four interaction beams (see Fig. 87.24). In addition, this sidescatter SBS may also be EM-seeded by its own reflection at the turning point. As a result, the two processes cannot be separated by this measurement alone. As will be discussed later, both the sidescattering and backscattering power reflectivities peak before the maximum of the laser pulse and have essentially identical power histories.

When all beams are turned on (squares in Fig. 87.23), the signal is much stronger than a linear superposition of the backscatter and sidescatter signals. The backscatter signal by itself (circles) is negligible, while the sidescatter signal (diamonds) provides the main EM seed for backscattering when all beams are turned on.

Representative time-resolved power reflectivities are shown in Fig. 87.25 for two experimental conditions. The power reflectivities at other intensities as well as the sidescatter power reflectivities (corresponding to the diamonds in Fig. 87.23) show similar temporal behaviors: they peak well before the laser pulse reaches its maximum. This rules out a linear scattering (or reflection or refraction) process that would peak toward the end of the laser pulse due to the heating of the plasma by the interaction beams. These power reflectivities show that the SBS backscatter and sidescatter signals are quenched before the peak of the laser pulse, possibly due to filamentation. A similar suppression of SBS forward scattering due to filamentation has been observed recently in experiments by Fuchs *et al.*¹¹ and in simulations by Tikhonchuk.^{10,12}

The measured multibeam reflectivities in FABS25 (squares in Fig. 87.23) are principally EM-seeded backscattering of beam 25 with the seed provided by SBS sidescattering of the opposing beam 23. The ion waves involved in this process are the same as those involved in the cooperative multibeam SBS process of beams 14 and 30, 12 and 52 (see Fig. 87.22). To check whether these common ion waves indeed play a role in

the sidescattering of beam 23, the intensities of several of the four beams were varied; the resulting FABS25 reflectivities are shown in Fig. 87.26 as a function of overlapped intensity. The sidescatter reflectivity declined with decreasing overlapped intensity of the four beams while the energies and intensities in beams 25 and 23 were kept constant. Thus, the differences in measured FABS25 reflectivities are clearly associated with the four asymmetrically located interaction beams. These same beams provide only a negligible EM seed to the SBS backscatter signal in FABS25 (stars in Fig. 87.23), but they do heat the plasma. These observations are consistent with the existence of common, symmetrically located ion waves produced by these four beams; these ion waves contribute significantly to the sidescattering of beam 23 into beam 25. Since the SBS reflectivities in Fig. 86.26 are well into the saturated regime, we estimate that the ion-wave amplitudes decline roughly by the same factor as the reflectivities. Alternatively, the change in electron temperature with increasing overlapped irradiation intensity may increase the EM seed for sidescattering, and consequently, also the total seed provided for backscattering. In this case no common ion waves would be involved. Our present experiments cannot rule out this scenario.

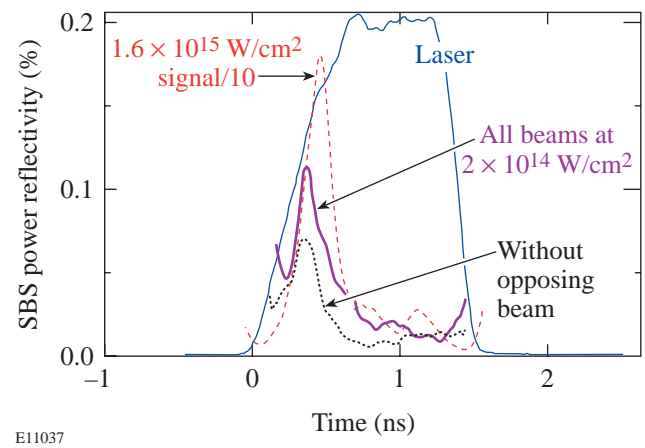


Figure 87.25
Measured multibeam SBS reflectivities for three different irradiation conditions along with a typical laser pulse shape. The dashed line is the backscatter signal in FABS30 for the irradiation conditions shown in Fig. 87.22. The dotted line and the thick solid line represent backscattering at low irradiation intensities with all interaction beams at $2 \times 10^{14} \text{ W/cm}^2$. For the dotted line the opposing beam 23 was turned off, resulting in pure backscattering of beam 25.

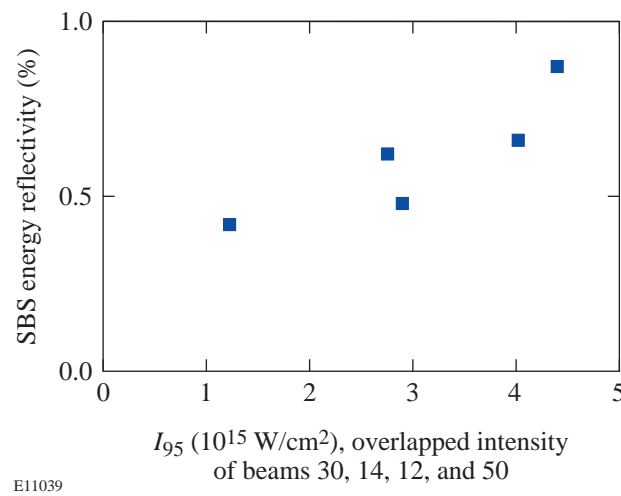


Figure 87.26

Backscatter reflectivities measured with FABS25 for the general irradiation conditions shown in Fig. 87.22 with some variations in beam energies of beams 30 and 14. The beam energies in beams 25 and 23 were kept constant. The increase in reflectivity with increasing overlapped intensity may be associated with a change in the common ion-acoustic-wave amplitudes generated by beams 30, 14, 12, and 50. Alternatively, the increase may be a consequence of decreased absorption as the plasma temperature increases with increasing overlapped intensity on target.

Conclusions

Multibeam interaction experiments were carried out in NIF-type, hot, long-scale-length plasmas on OMEGA using thick, planar CH targets. A symmetrical arrangement of six interaction beams with beam smoothing is consistent with strongly driven common ion waves located along the axis of symmetry of the six interaction beams. The present experiments, however, cannot rule out alternative interpretations that do not involve common ion waves. In either case, SBS sidescattering provides a large EM seed for SBS backscattering. These experiments have shown for the first time the synergistic enhancement of SBS sidescattering and backscattering. The fact that backscatter levels well below 1% are expected for typical NIF direct-drive irradiation conditions provides confidence in the expected direct-drive target performance on the NIF.²²

ACKNOWLEDGMENT

This work was supported by the U.S. Department of Energy Office of Inertial Confinement Fusion under Cooperative Agreement No. DE-FC03-92SF19460, the University of Rochester, and the New York State Energy Research and Development Authority. The support of DOE does not constitute an endorsement by DOE of the views expressed in this article.

REFERENCES

1. S. E. Bodner, D. G. Colombant, J. H. Gardner, R. H. Lehmberg, S. P. Obenschain, L. Phillips, A. J. Schmitt, J. D. Sethian, R. L. McCrory, W. Seka, C. P. Verdon, J. P. Knauer, B. B. Afeyan, and H. T. Powell, *Phys. Plasmas* **5**, 1901 (1998).
2. C. J. Walsh, D. M. Villeneuve, and H. A. Baldis, *Phys. Rev. Lett.* **53**, 1445 (1984).
3. D. M. Villeneuve, H. A. Baldis, and J. E. Bernard, *Phys. Rev. Lett.* **59**, 1585 (1987).
4. S. P. Regan, D. K. Bradley, A. V. Chirokikh, R. S. Craxton, D. D. Meyerhofer, W. Seka, R. W. Short, A. Simon, R. P. J. Town, B. Yaakobi, J. J. Carroll III, and R. P. Drake, *Phys. Plasmas* **6**, 2072 (1999).
5. W. Seka, R. E. Bahr, R. W. Short, A. Simon, R. S. Craxton, D. S. Montgomery, and A. E. Rubenchik, *Phys. Fluids B* **4**, 2232 (1992).
6. J. C. Fernández *et al.*, *Phys. Rev. Lett.* **81**, 2252 (1998).
7. J. C. Fernández *et al.*, *Phys. Plasmas* **4**, 1849 (1997).
8. J. A. Cobble *et al.*, *Phys. Plasmas* **7**, 323 (2000).
9. C. Labaune *et al.*, *Phys. Rev. Lett.* **85**, 1658 (2000).
10. V. T. Tikhonchuk *et al.*, *Phys. Plasmas* **8**, 1636 (2001).
11. J. Fuchs *et al.*, *Phys. Plasmas* **7**, 4659 (2000).
12. J. Myatt *et al.*, “Nonlinear Propagation of a Randomized Laser Beam Through an Expanding Plasma,” to be published in *Physical Review Letters*.
13. D. F. DuBois, B. Bezzeridels, and H. A. Rose, *Phys. Fluids B* **4**, 241 (1992).
14. H. A. Rose and D. F. DuBois, *Phys. Fluids B* **4**, 252 (1992).
15. H. A. Baldis *et al.*, *Phys. Rev. Lett.* **77**, 2957 (1996).
16. J. D. Lindl, *Inertial Confinement Fusion: The Quest for Ignition and Energy Gain Using Indirect Drive* (Springer-Verlag, New York, 1998), Chap. 6, pp. 61–82.

17. S. Skupsky and R. S. Craxton, Phys. Plasmas **6**, 2157 (1999).
18. T. R. Boehly, R. S. Craxton, T. H. Hinterman, P. A. Jaanimagi, R. L. Keck, J. H. Kelly, T. J. Kessler, R. L. Kremens, S. A. Kumpan, S. A. Letzring, R. L. McCrory, S. F. B. Morse, W. Seka, S. Skupsky, J. M. Soures, and C. P. Verdon, in *Proceedings of the IAEA Technical Committee Meeting on Drivers for Inertial Confinement Fusion*, edited by J. Coutant (IAEA, Vienna, 1995), pp. 79–86.
19. T. J. Kessler, Y. Lin, L. S. Iwan, W. P. Castle, C. Kellogg, J. Barone, E. Kowaluk, A. W. Schmid, K. L. Marshall, D. J. Smith, A. L. Rigatti, J. Warner, and A. R. Staley, in *Second Annual International Conference on Solid State Lasers for Application to Inertial Confinement Fusion*, edited by M. L. André (SPIE, Bellingham, WA, 1997), Vol. 3047, pp. 272–281.
20. W. Seka, R. S. Craxton, R. E. Bahr, D. L. Brown, D. K. Bradley, P. A. Jaanimagi, B. Yaakobi, and R. Epstein, Phys. Fluids B **4**, 432 (1992).
21. R. S. Craxton and R. L. McCrory, J. Appl. Phys. **56**, 108 (1984).
22. P. W. McKenty, V. N. Goncharov, R. P. J. Town, S. Skupsky, R. Betti, and R. L. McCrory, Phys. Plasmas **8**, 2315 (2001).

Hot-Electron Effect in Superconductors and Its Applications for Radiation Sensors

Introduction

The term “hot electrons” was originally introduced to describe nonequilibrium electrons (or holes) in semiconductors (for a review see, e.g., Ref. 1). The term encompasses electron distributions that could be formally described by the Fermi function but with an effective elevated temperature. The concept is very fruitful for semiconductors, where the mobility of carriers can be shown to depend on their effective temperature. In metals, however, electrons do not exhibit any pronounced variation of the mobility with their energy. As a result, heating of electrons in a metal does not affect the resistance,² unless the change in the effective temperature is comparable with the Fermi temperature.

Schklovski³ was the first to discuss the idea of combining the steady-state electron heating with the strong dependence of the resistance on the effective electron temperature in a metal film undergoing the superconducting transition. In the steady-state regime, however, electron heating is always masked by the conventional bolometric effect; therefore, experimental results on the heating of electrons by the dc current were not very convincing. The regime of dynamic electron heating by external radiation was studied in a series of experimental and theoretical works.^{4–6} It was immediately realized that the very short relaxation time of electron excitations would make it feasible to design extremely fast radiation sensors with a sensitivity much better than that of conventional bolometers.

During the last decade, a new generation of hot-electron superconducting sensors has been developed. These include submillimeter and THz mixers, direct detectors, and photon counters for the broad spectral range from microwaves to optical radiation and x rays. Activity in the field of hot-electron superconducting sensors is growing rapidly. These sensors have already demonstrated performance that makes them devices-of-choice for many far-infrared (THz), infrared, and optical wavelength applications, such as plasma diagnostics, laser studies, ground-based and airborne heterodyne astronomy, and single-photon-detection and quantum communications. Parallel development of compact cryocoolers and THz radia-

tion sources opens hot-electron sensors for satellite astronomy and communication applications. This article reviews the physical background of the hot-electron phenomenon in superconducting films and discusses various technical realizations of hot-electron radiation sensors.

Physics of Hot Electrons

Thermal dynamics in a superconducting film on a dielectric substrate can be thought of in terms of four co-existing subsystems: Cooper pairs, quasiparticles (electrons from broken Cooper pairs), phonons in the film, and phonons in the substrate. Thermal equilibrium exists when all of these can be described by equilibrium distribution functions with the same temperature. If any distribution does not satisfy these conditions, the situation is considered nonequilibrium. General treatment of a nonequilibrium state requires solution of the integral kinetic equations for space- and time-dependent distribution functions. To avoid the above complexity, various simplifying assumptions are used to reduce the general problem to analytically solvable rate equations.

1. Hot-Electron Cooling and Diffusion

The hot-electron model is most relevant for nonequilibrium superconductors maintained at temperature T near the superconducting transition T_c , where quasiparticles and phonons can be described by thermal, normal-state distribution functions, each with its own effective temperature. The electron and phonon effective temperatures (T_e and T_p) are assumed to be established instantly and uniformly throughout the whole specimen. This assumption implies that a rapid thermalization mechanism exists inside each subsystem.

The main steps of the hot-electron phenomenon that lead to the global equilibrium are depicted in Fig. 87.27. Introducing characteristic times of the energy exchange between subsystems reduces the problem of the global equilibrium recovery to a pair of coupled heat-balance equations for T_e and T_p . The intrinsic thermalization time τ_T should be short compared to energy exchange times. This two-temperature (2-T) approach was used for the first time by Kaganov *et al.*² to describe

steady-state electron heating in metals. Below T_c , the electron specific heat exhibits an exponential temperature dependence that makes equations nonlinear for even small deviations from equilibrium. The description can, however, be simplified in the vicinity of T_c . At this temperature the superconducting energy gap is strongly suppressed, concentration of Cooper pairs is very small, and unpaired electrons exhibit no significant superconducting peculiarities: they are regarded as normal electrons having the ordinary Fermi distribution function. In the normal state, the specific heat of electrons has a much weaker temperature dependence, which can be neglected for small deviations of T_e from the equilibrium. With these assumptions, the equations describing the hot-electron effect in superconductors become linear and can be written as

$$\frac{dT_e}{dt} = -\frac{T_e - T_p}{\tau_{ep}} + \frac{1}{C_e} W(t), \quad (1a)$$

$$\frac{dT_p}{dt} = \frac{C_e}{C_p} \frac{T_e - T_p}{\tau_{ep}} - \frac{T_p - T_0}{\tau_{es}}, \quad (1b)$$

where $W(t)$ represents the external perturbation (i.e., the power per unit volume absorbed by the electron subsystem); τ_{ep} and τ_{es} are the electron energy relaxation time via electron–phonon interaction and the time of phonon escape into the substrate; C_e and C_p are the electron and phonon specific heats, respectively;

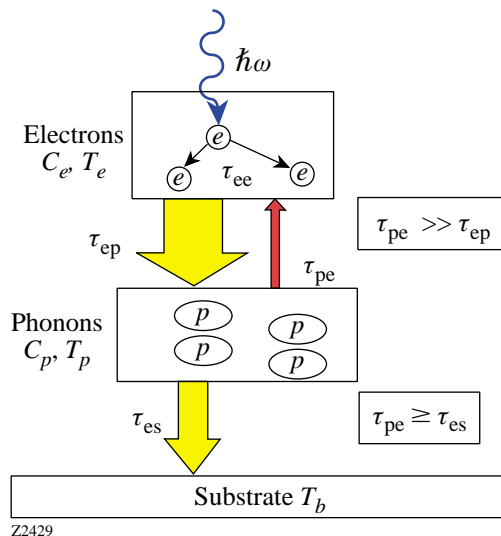


Figure 87.27

Thermalization scheme showing various channels of the energy transfer in a hot-electron device that relaxes toward global equilibrium.

and T_0 is the ambient (substrate) temperature. To derive the 2-T equations we used the condition of the energy-flow balance in equilibrium $\tau_{pe} = \tau_{ep}(C_p/C_e)$, where τ_{pe} is the phonon–electron energy relaxation time.

The first implementation of the electron-heating model to superconductors was made by Shklovski,³ who used a more general, nonlinear form of the heat-balance equations to describe hysteresis of the critical current in a thin lead film. An analytical solution of Eq. (1) was first obtained for sinusoidal perturbations by Perrin and Vanneste⁴ and for an optical pulse excitation by Semenov *et al.*⁵ In the latter case, thermalization of electrons was interpreted as an increase of T_e . The increase was assumed to occur during a time interval that depended on both the duration of the optical pulse and the intrinsic thermalization time τ_T . The model was used to describe the response of superconducting NbN and $\text{YBa}_2\text{Cu}_3\text{O}_{7-\delta}$ (YBCO) films in the resistive state to near-infrared and visible radiation.^{5,7} Figures 87.28 and 87.29 show a good agreement between experimental signals and the theoretical simulation.

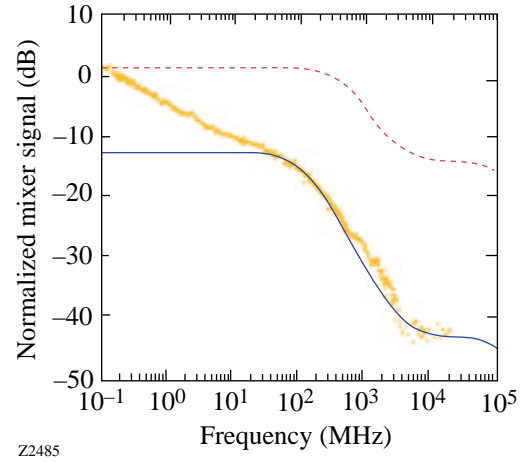


Figure 87.28

Response of a YBCO hot-electron photodetector (HEP) to optical radiation (dots) versus modulation frequency (Ref. 7). The solid line was calculated using Eqs. (1). The discrepancy at low frequencies is due to phonon diffusion in the substrate that was not accounted for in the model. The dashed line represents the thermal model.

Figure 87.30 presents the detailed thermalization diagrams for both YBCO [Fig. 87.30(a)] and NbN [Fig. 87.30(b)] thin films excited by 100-fs-wide optical pulses. The diagrams depict the process in the same manner as Fig. 87.27 but now include the actual values of the characteristic time constants for both materials. The values were obtained from the 2-T model via the fit of Eqs. (1) to the experimental photoresponse

data. The measurements were performed using the electro-optic sampling system, which allowed obtaining the intrinsic, time-resolved dynamics of the electron thermalization process in 3.5-nm-thick NbN⁸ and 100-nm-thick YBCO films.⁹ We note that, in general, the dynamic of the YBCO thermalization is roughly one order of magnitude faster than that of NbN. In both cases, the energy flow from electrons to phonons dominates the energy backflow due to reabsorption of nonequilibrium phonons by electrons; however, while the energy backflow in YBCO can be neglected because of the very large ratio $C_p/C_e = 38$, in NbN it constitutes a non-negligible 15% ($C_p/C_e = 6.5$) of direct electron–phonon energy relaxation. Consequently, in YBCO film excited on the femtosecond time scale, the nonthermal (hot-electron) and thermal, bolometric (phonon) processes are practically decoupled, with the former totally dominating the early stages of electron relaxation. On the other hand, the response of NbN devices is determined by the “average” electron cooling time τ_e , which is given by $\tau_{ep} + (1 + C_e/C_p)\tau_{es}$ ^{4,5} and corresponds to the time that elapses from the peak response until the magnitude of the response declines to $1/e$ of the maximum value. If the external perturbation is substantially longer than τ_{pe} (that is, >100 ps for YBCO films), the YBCO response is dominated by the bolometric process, as was shown by the bulk of the early photoresponse measurements.¹⁰ The very large difference in the τ_{es} values for YBCO and NbN is mainly due to the drastic difference in thickness of the tested films. Additionally, ultrathin NbN films are a better acoustical match to the substrate. This significantly reduces τ_{es} .

Electron heating in the limiting case of a very short phonon escape time, $\tau_{es} \ll \tau_{ep}$, τ_{pe} , was first studied by Gershenson *et al.*⁶ for Nb films. Although for this material¹¹ $C_p/C_e \approx 0.25$ and, consequently, $\tau_{ep} > \tau_{pe}$, the effective escape of phonons to

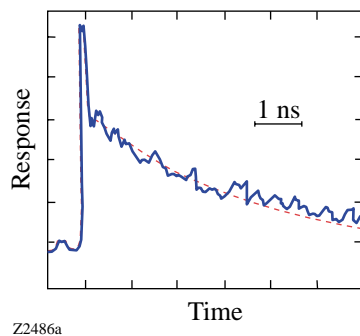


Figure 87.29

Response of a YBCO HEP to a femtosecond infrared pulse: experimental data (solid line) (Ref. 5) and simulations (dashed line) based on the 2-T model.

the substrate prevents energy backflow to electrons. As a result, τ_{ep} alone controls the response of ultrathin (<10-nm) Nb films. Typical electron relaxation time in Nb is ≈ 1 ns at 4.2 K, which is over an order of magnitude larger than in NbN.

The 2-T model represented by Eqs. (1) is essentially the small-signal model. Deviations of the effective temperatures from equilibrium due to both the joule power dissipated by the bias current and absorbed radiation power are assumed small compared to their equilibrium values. The theory of operation of a hot-electron photodetector (HEP) was developed on the basis of this model by Gershenson *et al.*,¹² and a novel hot-electron mixer (HEM) was proposed.^{12,13}

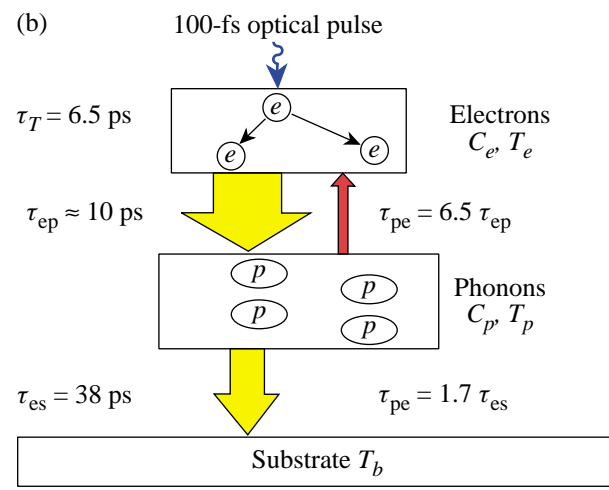
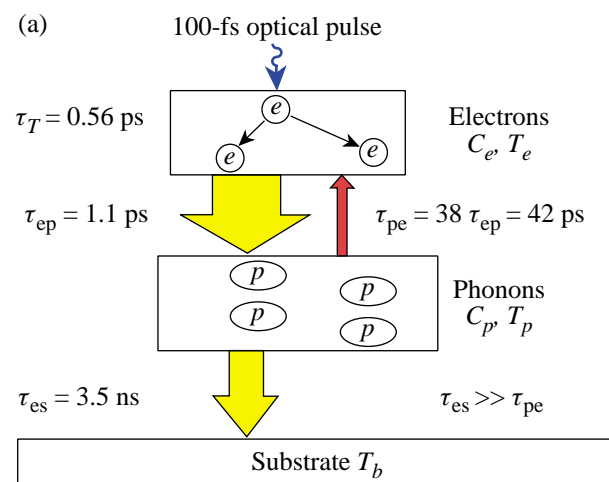


Figure 87.30

Hot-electron relaxation diagrams and characteristic times for (a) thin-film YBCO (Ref. 9) and (b) ultrathin NbN film (Ref. 8).

The 2-T approach neglects, however, diffusion of electrons and assumes that the effective temperatures remain uniform within the whole device. A different approach was proposed by Prober,¹⁴ who considered diffusion of hot electrons out of the active area, rather than the energy transfer to phonons, as the main mechanism of the electron cooling. If the device length L is short compared to the thermal diffusion length $L_{\text{th}} = (D\tau_e)^{1/2}$, where τ_e is the electron cooling time and D is the electron diffusivity, relaxation of T_e is controlled by the electron out-diffusion time $\tau_d = (L^2/\pi^2 D)$. In the limiting case $L \ll L_{\text{th}}$, T_e remains almost uniform through the device length. The device can then be described by Eq. (1a), in which τ_{ep} and T_p should be substituted for τ_d and T_0 , respectively. For longer devices, both the actual distribution of T_e along the device length and the phonon contribution to the electron relaxation should be taken into account.

2. Large-Signal Models

The common disadvantage of the small-signal model described above is that the optimal values of the bias current (for

HEP's) and power of the local oscillator (for the HEM theory) are not derived in the framework of the model, but rather taken from the experiment or independently estimated. To include the bias current and the local oscillator (LO) power in a consistent manner, one should specify the structure of the resistive state and account for the dependence of the electron-cooling rate on the deviation from the equilibrium. For large deviations from equilibrium, heat-balance equations become nonlinear.

The large-signal mixer theory was developed by Nebosis *et al.*¹⁵ for the uniform resistive state (which is, of course, a very crude approximation). The authors assumed a finite value of τ_{es} and introduced the superconducting critical current. Reasonable quantitative agreement (see Fig. 87.31) was found between the experimental data for NbN mixers and the theoretical results. Karasik *et al.*¹⁶ implemented a similar approach for modeling a bolometric mixer fabricated from a high-temperature superconducting material. Floet *et al.*¹⁷ considered the nonuniform resistive state of a hot-electron bolometer in the small-signal regime for $\tau_{\text{es}} = 0$, while Merkel *et al.*¹⁸ developed the large-signal nonlinear model for a finite, non-zero value of τ_{es} . Both models described the resistive state of the mixer at optimal operation conditions in terms of a normal hot spot, maintained by self-heating. The hot spot occupies only a portion of the device length, thus assuring a mixer resistance between zero and the normal-state value. In this approach, the LO power is assumed to be uniformly absorbed in the mixer, whereas the joule power dissipation due to the bias current appears in the hot-spot region only. Since the diffusion of electrons is introduced in the basic equations, this model naturally covers all intermediate cases between the extreme diffusion cooling ($L \ll L_{\text{th}}$) and phonon-cooling ($L \gg L_{\text{th}}$) regimes. Neglecting phonons ($\tau_{\text{es}} = 0$) and simulta-

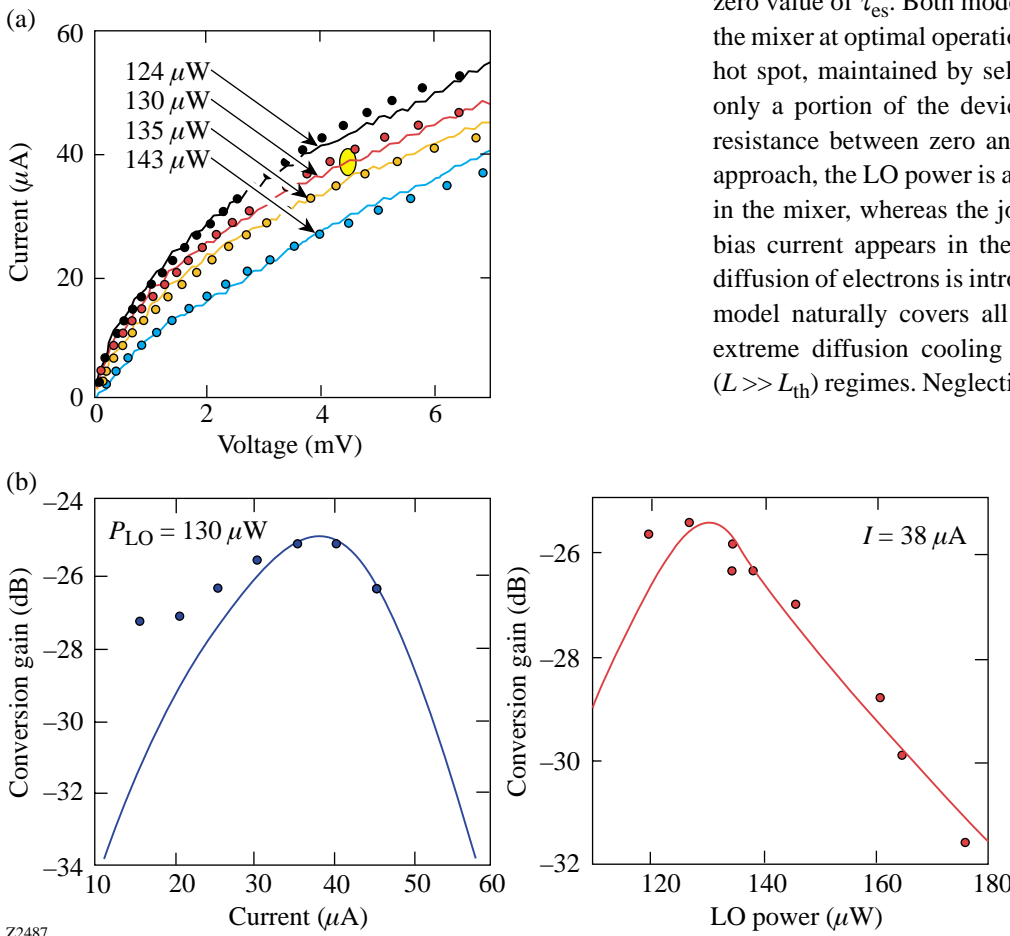


Figure 87.31
(a) Current–voltage characteristics for different LO power values. (b) Conversion gain curves for a NbN HEM compared with results of the uniform model (solid lines) (Ref. 15).

neously assuming $\tau_T = 0$, one can reduce the problem to the following system of equations¹⁷ for T_e :

$$\begin{aligned} -K \frac{d^2 T_e}{dx^2} + \frac{C_e}{\tau_e} (T_e - T_0) &= j^2 \rho_n + P_{RF} \quad (\text{inside hot spot}), \\ -K \frac{d^2 T_e}{dx^2} + \frac{C_e}{\tau_e} (T_e - T_0) &= P_{RF} \quad (\text{outside hot spot}), \end{aligned} \quad (2)$$

where K is the thermal conductivity, j is the bias current density, ρ_n is the resistivity of the mixer in the normal state, and P_{RF} is the LO power absorbed per unit volume. This description allows for an analytical solution, which returns the bias current as a function of the hot-spot length, and, thus, a voltage drop across the device. Results of simulations¹⁷ are in good agreement with the experimental current–voltage (I – V) characteristics, especially for large P_{RF} values, which drive the mixer almost into the normal state. Surprisingly, results based on not only Eq. (2), but even on the more-accurate numerical model¹⁸ shown in Fig. 87.32, do not differ much from simulations based on the uniform 2-T model (Fig. 87.31). With the appropriate set of fitting parameters, both approaches describe fairly well the I – V characteristics of the HEM and predict reasonable values of the conversion efficiency and noise temperature.

A nonthermal regime of the diffusion-cooled HEM was described by Semenov and Gol'tsman.¹⁹ The authors considered a short device made from a clean material, in which τ_T is larger than τ_d . The device operated in the nonthermal regime

and had the advantage of a short response time (or, equivalently, a large bandwidth) in the heterodyne mode. On the other hand, incomplete thermalization hampered the responsivity and increased the relative contribution of the Johnson noise to the total electric noise of the device. Compared to HEM's operated in the thermal regime, the nonthermal mixer required more power from LO. At low temperatures, however, the nonthermal regime of operation provided almost quantum-limited sensitivity.

The electric noise of a hot-electron sensor is comprised of the same components as the noise of any conventional bolometer: shot noise, Johnson noise, thermal noise, and flicker noise. To our knowledge, there is no consistent theory for flicker noise, so its contribution may be determined only experimentally. Unless the sensitivity of the bolometer reaches the quantum limit, the noise due to fluctuations in the background radiation can be neglected. The typical length of hot-electron devices studied so far was much larger than the diffusion length associated with the electron–electron scattering. In this limiting case, the superposition of Johnson noise and shot noise reduces to the Nyquist form, i.e., the spectral density of the voltage noise is $S_V = 4 k_B T R$, where R is the resistance of the device. This noise has a “white” spectrum up to very high frequencies. The corresponding contribution to the system-noise temperature in the heterodyne regime increases rapidly when the conversion efficiency rolls off at intermediate frequencies (IF's) larger than $1/\tau_e$.

Thermal noise contributes to the total spectral density the amount $4 k_B T^2 I^2 \tau_e (\partial R / \partial T_e)^2 / (C_e v)$, where I is the bias current and v is the volume of the sensor. Since the conversion efficiency is proportional to $I^{-2} \tau_e^2 P_{RF} (\partial R / \partial T_e)^2 / (C_e v)^2$ and

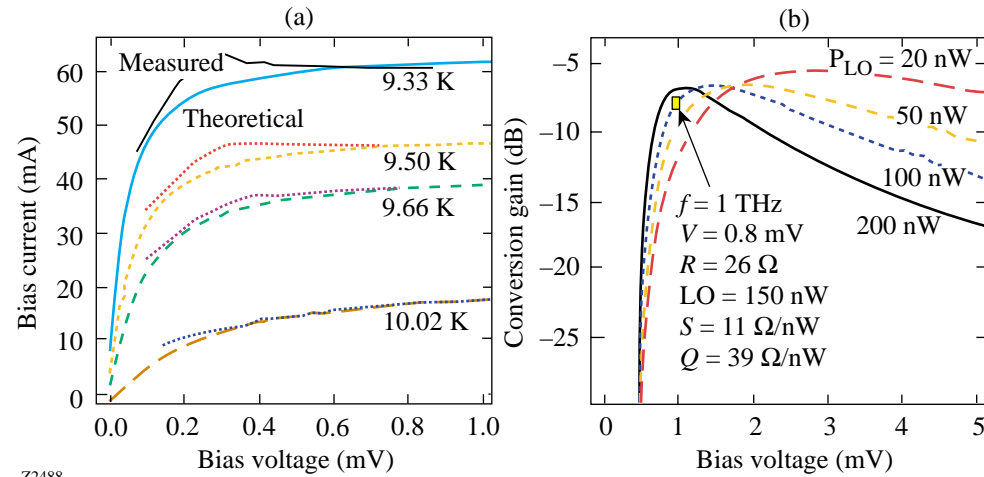


Figure 87.32
(a) Current–voltage characteristics and (b) conversion gain of a NbN HEM simulated in the framework of the hot-spot model (Ref. 18). Experimental characteristics are shown for comparison.

has the same roll-off frequency, the noise temperature of the mixer due to thermal fluctuations is given by $T_N \approx T_e^2 C_e v / (\alpha \tau_e P_{RF})$, where α is the optical coupling efficiency. The contribution to the noise temperature due to thermal fluctuations does not depend on the intermediate frequency; neither does the corresponding noise-equivalent power (NEP) in the direct-detection mode,

$$\text{NEP} \approx (T_e / \alpha) (k_B C_e v / \tau_e)^{1/2}.$$

On the contrary, the contribution due to the Nyquist term increases rapidly at IF's larger than $1/\tau_e$ and usually limits the IF noise bandwidth of the mixer.

Though the above simple treatment of the bolometer noise explains the main features, it does not provide an appropriate tool for computations. To obtain exact results, one should take into account the positive feedback via the load resistor and self-heating by the bias current. The former enhances the system output noise because the bolometer rectifies part of its own noise voltage drop across intrinsic resistance. The latter effect typically increases the IF bandwidth in the heterodyne regime and decreases the response time in the direct-detection mode. It is of little practical use, however, because operation in the vicinity of the thermal roll-off requires very precise stabilization of the ambient temperature. For a HEM with dc resistance R at the operation point and connected to the IF load with the impedance R_L , the dependence of the conversion efficiency $\eta(\omega)$ and single-sideband noise temperature $T_{SSB}(\omega)$ on the IF was derived in the framework of the uniform model¹⁵

$$\eta(\omega) = \frac{2\alpha}{I^2} \frac{R_L}{(R_L + R_\infty)^2} \frac{C^2 P_{RF}}{\left(C \frac{R - R_L}{R_L + R_\infty} + \xi\right)^2 + \varphi^2}, \quad (3)$$

$$T_{SSB}(\omega) = \frac{2T_e R_\infty I^2}{\alpha C^2 P_{RF}} \left(\xi^2 + \varphi^2 \right) + \frac{2T_e^2 \tau_e}{C_e V \alpha P_{RF}}, \quad (4)$$

where

$$C = I^2 \tau_e \frac{\partial R / \partial T_e}{C_e V},$$

$$\xi(\omega) = \frac{1 + \omega^2 (\tau_1 \tau_3 + \tau_2 \tau_3 - \tau_1 \tau_2)}{1 + (\omega \tau_3)^2},$$

$$\varphi(\omega) = \frac{\omega (\tau_1 + \tau_2 - \tau_3) + \omega^3 \tau_1 \tau_2 \tau_3}{1 + (\omega \tau_3)^2},$$

$$\tau_{1,2}^{-1} = \frac{1}{2} \left(\frac{1}{\tau_{ep}} + \frac{C_e}{C_p \tau_{ep}} + \frac{1}{\tau_{es}} \right)$$

$$\times \left[1 \pm \sqrt{\frac{\frac{4}{\tau_{ep} \tau_{es}}}{\left(\frac{1}{\tau_{ep}} + \frac{C_e}{C_p \tau_{ep}} + \frac{1}{\tau_{es}} \right)^2}} \right],$$

and

$$\tau_3 = \frac{\tau_{ep} \tau_{es}}{\tau_e}.$$

In the above equations, R_∞ is the impedance of the bolometer at very high IF, and $\partial R / \partial T_e$ is the slope of the superconducting transition at the operation point on the scale of the electron temperature. The slope of the transition cannot be derived from first principles in the framework of the uniform model. Its temperature dependence should be calculated in a phenomenological manner (see, e.g., Ref. 15), or the value at the specific operation regime should be concluded from the experiment. Ekström *et al.*²⁰ showed that the magnitude of the parameter C in Eqs. (3) and (4) can be determined from the experimental dc I - V characteristic as

$$C = \frac{\frac{dV}{dI} - R}{\frac{dV}{dR} + R}, \quad (5)$$

where dV/dI is the differential resistance of the HEM at the operation point. The advantage of the hot-spot model¹⁸ is that it allows for numerical computation of the superconducting

transition slope for arbitrary values of the LO power, bias current, and ambient temperature.

3. Cooper-Pair, Kinetic-Inductive Photoresponse

Although the response of a superconductor that is kept well below T_c to external radiation cannot be adequately treated in the framework of the hot-electron approximation, we decided to include superconducting detectors operating at $T \ll T_c$ in our review. Rothwarf and Taylor²¹ were the first to successfully develop the phenomenological description for non-equilibrium Cooper-pair recombination and breaking processes (so-called the RT model). At low temperatures, when energies of nonequilibrium quasiparticles after thermalization are spread over a narrow interval above the superconducting energy gap 2Δ , the appropriate parameters to characterize this nonequilibrium state are the number Δn_q of excess quasiparticles and the number Δn_p of excess, so-called, 2Δ phonons. The 2Δ phonons are emitted in the Cooper-pair recombination process and, since they have the energy of at least 2Δ , they are responsible for secondary breaking of Cooper pairs. For small perturbations, concentrations of Δn_q and Δn_p are given by the following linearized RT rate equations:

$$\frac{d}{dt} \Delta n_q = -\frac{\Delta n_q}{\tau_R} + \frac{2\Delta n_p}{\tau_B}, \quad (6a)$$

$$\frac{d}{dt} \Delta n_p = -\frac{\Delta n_p}{\tau_B} - \frac{\Delta n_p}{\tau_{es}} + \frac{2\Delta n_q}{\tau_R}, \quad (6b)$$

where τ_R and τ_B are the quasiparticle recombination time and the time of breaking Cooper pairs by 2Δ phonons, respectively. We note that Eqs. (6) are mathematically analogous to the 2-T model [Eqs. (1)]. Like the 2-T model, the RT approach assumes that there is a quick, intrinsic thermalization mechanism inside both the quasiparticle and phonon subsystems.

When photons with energy typically much larger than 2Δ are absorbed by a superconducting film maintained at $T \ll T_c$, they produce a time-dependent population $\Delta n_q(t)$ of nonequilibrium quasiparticles, leading to a temporary decrease in the superconducting fraction of electrons, $f_{sc} = (n_0 - n_q)/n_0$, where $n_q = n_q(0) + \Delta n_q(t)$ is the instant concentration of the quasiparticles, $n_q(0)$ is their equilibrium concentration, and n_0 is the total concentration of electrons. Because the pairs are characterized by non-zero inertia, this process can be modeled as time-varying kinetic inductance:^{22,23}

$$L_{kin}(t) = \frac{L_{kin}(0)}{f_{sc}}, \quad (7)$$

where $L_{kin}(0) = \mu_0(\lambda_L)^2/d$ is the equilibrium value per unit area of the film, λ_L is the magnetic penetration depth, and d is the film thickness. The change in time of L_{kin} in a current-biased superconducting film leads to a measurable voltage signal across the film edges.

For the limiting case of very fast thermalization, i.e., when τ_T is small compared to both τ_R and τ_B , the kinetic-inductive response was described by Semenov *et al.*²⁴ as the product of the analytical solution of Eqs. (6) and a fitting factor exponentially growing in time. The latter parameter corresponded to the multiplication cascade of quasiparticles during thermalization. The kinetic-inductive model describes well the experimental results obtained with pulsed and modulated cw excitations, for both the low-temperature superconductor (LTS) films (Fig. 87.33 and Ref. 24) and the high-temperature superconductor (HTS) films (Fig. 87.34 and Refs. 9 and 25).

4. Single-Photon-Detection Mechanisms

So far this discussion has been limited to integrating detectors in which the energy of a large number of absorbed photons is distributed among an even larger number of elementary thermal excitations in the detector. That is, individual photons cannot be distinguished, and only the average radiation power absorbed by the detector is measured. In the particular case of a thermal detector, e.g., a bolometer or a hot-electron detector near T_c , this average absorbed radiation power corresponds to enhanced effective temperatures of phonons and electrons, respectively. In a quantum (photon) detector, a single photon creates excitations that are collected and counted before they relax and before another photon is absorbed. Thus, the detector registers each absorbed photon, while the number of collected excitations measures the energy of absorbed photons.

The hot-electron quantum detector was first proposed by Kadin and Johnson.²⁶ In this model, a photon absorbed somewhere in the film initiates a growing hot spot. The resistance inside the hot spot is larger than in the surrounding area. Even if the size of the hot spot is much smaller than the size of the film, the voltage drop across the current-biased film “feels” the presence of the hot spot. The disadvantage of this approach for practical devices stems from the fact that the film is operated near its T_c and can withstand only a very small current density without being driven into the normal state. Since the

detector response is proportional to the bias current, the small operating current requires a complicated, SQUID-based read-out scheme.²⁷

Semenov *et al.*²⁸ proposed a different quantum detection regime in a superconducting stripe that is operated well below T_c and carries a bias current only slightly smaller than the critical value at the operating temperature. Generation of a hot spot at the position where the photon has been absorbed creates a local region with suppressed superconductivity (normal region). The supercurrent is forced to flow around the normal

(resistive) spot, through those parts of the film that remain superconducting. If the diameter of the resistive spot is such that the current density in the superconducting portion of the film reaches the critical value, a resistive barrier is formed across the entire width of the stripe, giving rise to a voltage pulse with the magnitude proportional to the bias current.

The physical difference of the quantum detection proposed in Ref. 28, as compared to Ref. 26, is that the resistive state and, thus, the response appear to be caused by the collaborative effect of the bias current and the hot-spot formation. In the hot

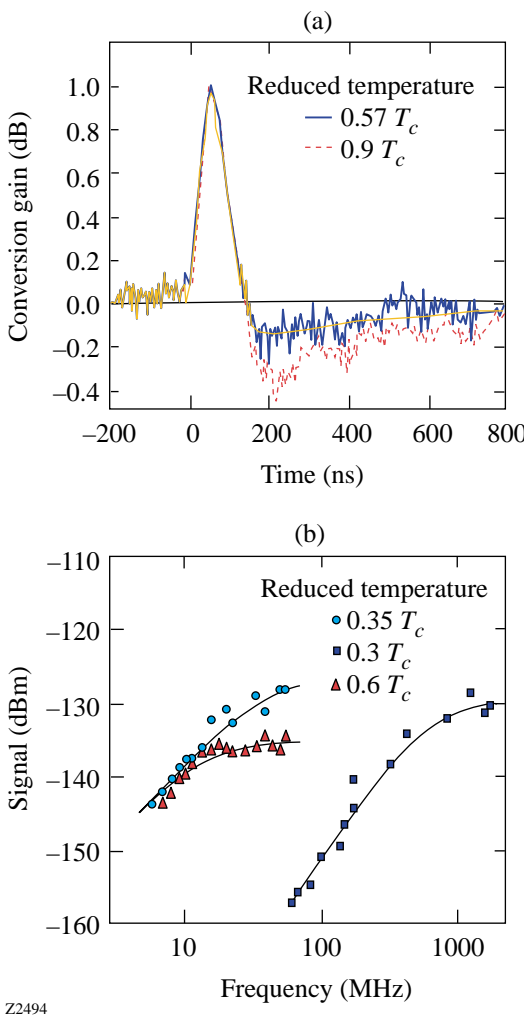


Figure 87.33
(a) Conversion gain and (b) signal response of a NbN HEP to pulsed and modulated cw optical radiation in comparison with model simulations based on Eqs. (6) (Ref. 24).

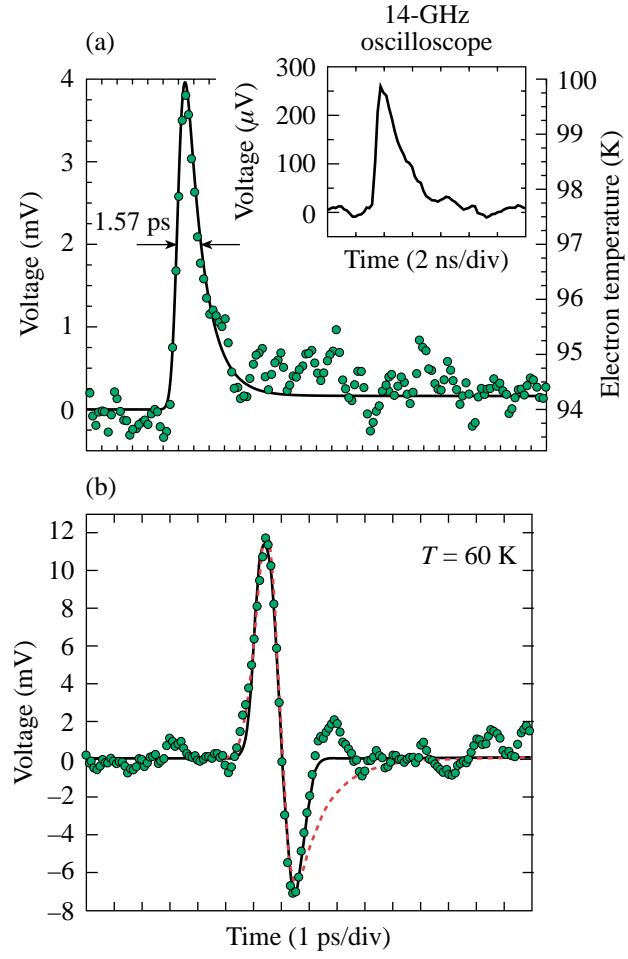


Figure 87.34
Experimental response (dots) of a YBCO HEP to 100-fs-wide optical pulses (Refs. 9 and 25). Simulated transients were obtained (a) with the uniform hot-electron model [Eqs. (1)] for the operation in the resistive state and (b) with the RT model [Eqs. (6)—solid line] and the 2-T model [Eqs. (1)—dashed line], for operation at low temperatures in the superconducting state. Inset in (a) shows a bolometric response.

spot, the nonequilibrium quasiparticle concentration increases due to hot-electron thermalization (multiplication) and decreases due to electron out-diffusion. The normal spot at the absorption site occurs when the concentration of nonequilibrium electrons exceeds the critical value corresponding to the local normal state. If the film thickness d is small compared to L_{th} , the concentration of nonequilibrium thermalized quasiparticles is given by

$$\frac{\partial}{\partial t} \Delta n_q = D \nabla^2 \Delta n_q + \frac{\Delta n_q}{\tau_e} + \frac{d}{dt} M(t), \quad (8)$$

where $M(t)$ is the multiplication factor and D is the normal-state electron diffusivity. The maximum value that $M(t)$ reaches during the avalanche multiplication process is called quantum yield or quantum gain; it is proportional to the energy of the absorbed quantum. Under assumptions that the $M(t)$ rate is much larger than the $1/\tau_e$ rate and that the photon is absorbed at $t = 0$ and $r = 0$, the solution for the time-dependent quasiparticle concentration profile takes the form

$$\Delta n_q(r,t) = \frac{M(t)}{4\pi D d} \frac{1}{t} e^{-t/\tau_e} e^{-r^2/4Dt}. \quad (9)$$

The diameter of the normal spot is determined from the condition $n_q(0) + \Delta n_q(r,t) > n_0$. The maximum diameter of the normal spot increases with the quantum energy. The model²⁸ predicts an almost-Gaussian response pulse with a magnitude that, up to a certain extent, does not depend on the photon energy. On the other hand, the pulse duration is a function of the maximum spot size, providing the basis for spectral sensitivity of the device. Finally, the single-quantum detection regime should have a cutoff wavelength that depends on operating conditions (bias current and temperature) and the detector size. Since such a detector counts individual photons, it should have ultimate background-limited sensitivity through the whole range of operation conditions.

Gol'tsman *et al.*²⁹ experimentally demonstrated the supercurrent-assisted, hot-spot-detection mechanism for single optical (790-μm-wavelength) photons. Figure 87.35 shows a collection of “snapshots” recorded by a 1-GHz-bandwidth oscilloscope for different energies per laser pulse, incident on the NbN quantum HEP. Each snapshot presents an 80-ns-long record of the response to six successive 100-fs-wide pulses and was randomly selected out of a real-time detector output data stream. Trace A in Fig. 87.35 corresponds to an average of 100

photons per pulse hitting the detector. In this case, the HEP responded to each optical pulse in the laser train. The same 100%-efficient response was observed (trace B) when there were approximately 50 photons per pulse. As the incident laser intensity was further decreased (with other experimental conditions unchanged), the quantum nature of the detector response emerged. Instead of the linear decrease of the signal amplitude with incident light intensity, which is characteristic of a classical integrating detector, the response amplitude of the single-photon HEP remained nominally the same. In addition, some of the response pulses were missing because of the limited quantum efficiency of the device as well as fluctuations in the number of photons incident on the detector. The quantum voltage response of the HEP is most apparent in the bottom two pairs of traces: C and D (five photons/pulse) and E and F (one photon/pulse). Each pair corresponds to two different randomly selected records obtained under exactly the same experimental conditions. Note that in each case the detector response is very different. Averaging over a long observation time, however, showed that both the average number of captured pulses and their magnitude remained constant if the pulse energy was unchanged. This unambiguously demonstrated the single-photon operation of the device.

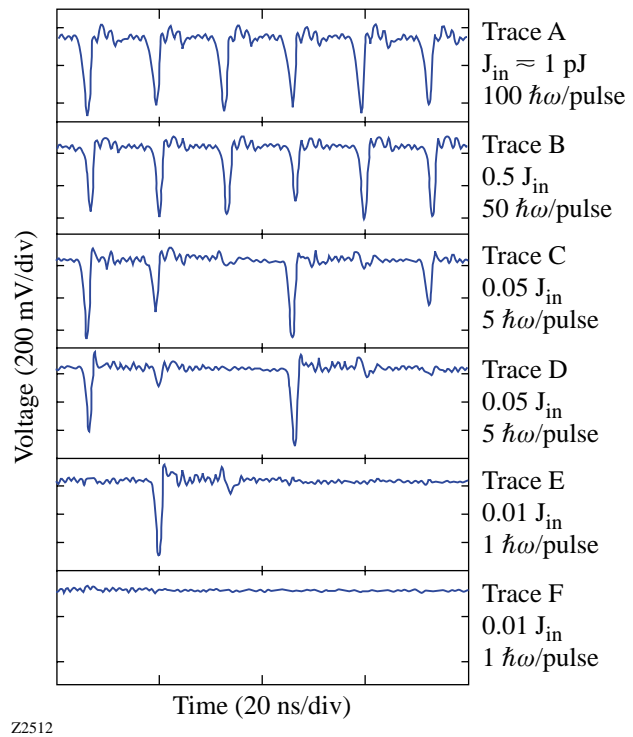


Figure 87.35
Response of a NbN quantum detector to trains of 100-fs optical pulses with a different number of photons per pulse (see text for details).

For a mean number of photons per pulse (m), the probability $P(n)$ of absorbing n photons from a given pulse is proportional to

$$P(n) \sim \frac{e^{-m}(m)^n}{n!}. \quad (10)$$

When the mean number of photons $m \ll 1$ (achieved, for example, by attenuating the radiation fluence to reduce the total number of photons incident on the detector to an average of much less than one photon per pulse),

$$P(n) \sim \frac{m^n}{n!}. \quad (11)$$

Consequently, for very weak photon fluxes, the probability of detecting one photon, two photons, three photons, etc., is

$$P(1) \sim m, P(2) \sim \frac{m^2}{2}, P(3) \sim \frac{m^3}{6}, \text{ etc.} \quad (12)$$

Figure 87.36 plots the probability of the detector producing an output voltage pulse as a function of the number of photons per pulse, incident on the device area for two different values of the bias current. The left vertical axis indicates the mean number of detector counts per second. The right vertical axis corresponds to the probability of detecting an optical pulse. Open squares correspond to the bias current $0.92 I_c$, where I_c is the critical current at the operation temperature. Saturation occurs at high incident photon fluxes. For smaller fluxes, as predicted by Eq. (11), the experimental data show the linear decrease of detection probability with the average number of incident photons over four orders of magnitude, clearly demonstrating the single-photon detection. At very low photon doses, experimental data points saturate at the level of 0.4-s^{-1} counts (probability 4×10^{-4}) since the experiment was performed in an optically unshielded environment. This level is regarded as the laboratory photon background. The solid squares in Fig. 87.36 correspond to the same device, operated under the same conditions as those for the solid-square data, but biased with $0.8 I_c$. Experimental data points now follow a quadratic dependence of detection probability [see Eq. (12)], showing the two-photon detection. As expected for a two-photon process, the quantum efficiency is significantly lower than for the single-photon detection. At the same time, photon background is no longer observed since the probability of two

uncorrelated, stray photons hitting the device within its response duration is negligibly small.

A nonequilibrium model of a single quantum x-ray detector with the readout via the superconducting tunneling junction was developed by Twerenbold.³⁰ Typically, a tunnel-junction detector consists of a relatively thick absorber film with an underlying thinner trapping layer, which forms one junction electrode. A photon captured in the absorber generates a high-energy photoelectron that relaxes via hot-electron multiplication into the energy gap of the absorber. Nonequilibrium quasiparticles excited during the cascade diffuse to the adjacent trapping layer, which has a smaller energy gap. There, quasiparticles scatter inelastically, reaching an energy level corresponding to the trapping-layer energy gap. The latter process is called “trapping” because it confines the charge to the region close to the tunnel barrier. The tunnel junction is externally biased in such a way that trapped quasiparticles can tunnel directly to the electrode characterized by the lower-energy gap. The same potential barrier prevents them from returning. They can, however, break Cooper pairs in the low-gap electrode and then form new pairs with unpaired electrons in their own electrode. Thus, the process returns unpaired electrons to the initial electrode, increasing the number of tunneling events per quasiparticle and providing intrinsic charge amplification. The time integral of the current transient

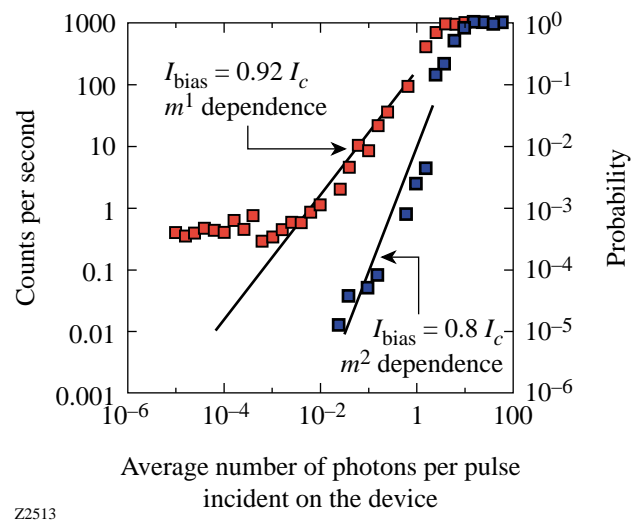


Figure 87.36
Count rates and the corresponding counting probability for a NbN quantum detector as a function of the radiation intensity. Depending on bias current, the detector can count single-photon (red squares) or two-photon (blue squares) events (Ref. 29).

gives, with no free parameters, the charge that has been transferred through the tunnel junction. This latter value is proportional to the number of quasiparticles created in the cascade and, consequently, to the x-ray quantum energy.

The theoretical energy resolution of the tunnel junction detector is given by $2.4[hv\Delta(F+1+1/n)]^{1/2}$, where hv is the quantum energy, n is the number of tunneling events per one quasiparticle, and F is the Fano factor that describes the statistical fluctuations of the charge-generation process. The Twerenbold model incorporates the two-dimensional diffusion equation for Δn_q and the general nonlinear form of the RT equations.

A more general approach, including time evolution of nonequilibrium distribution functions of quasiparticles and phonons, was developed by Nussbaumer *et al.*³¹ The authors solved the Chang-Scalapino equations numerically for the quasiparticle and phonon distribution functions in a spatially homogeneous situation and supplemented the solution by one-dimensional diffusion. The full theory includes the parameters that are important for the real detector, such as back tunneling and losses of quasiparticles at the edges of the device, resulting in good agreement between the calculated transient response signals and the experimentally measured pulse shapes.

Hot-Electron Detectors

A minor, but physically very important, difference exists between a superconducting HEP and a conventional superconducting bolometer when they are operated in the transition-edge regime. In the bolometer, thermal equilibrium between electrons and phonons is established instantly, whereas in the hot-electron detector these two systems are not in equilibrium. In this review, we restrict ourselves to publications where the nonequilibrium state between the electron and phonon subsystems was clearly observed. Basically, there are two ways to decouple electrons from phonons: nonequilibrium phonons should leave the detector at a time scale that is short compared to τ_{pe} , or the intensity of external radiation should vary faster than $1/\tau_{pe}$. Depending on the superconductor and experimental arrangement, a real hot-electron detector falls somewhere between these two extremes.

1. Transition-Edge Superconducting Detectors

Historically, the first HEP's were developed and studied in the early 1980s by Gershenzon *et al.*,³² using ultrathin Nb films as the detector body. Niobium is characterized by relatively long τ_{pe} , typically a few hundred nanoseconds at liquid helium temperature, so that $\tau_{es} < \tau_{ep}$ for films thinner than

10 nm.¹¹ Therefore, detectors based on thin Nb films belong to the first limiting case in that their response time is approximately equal to τ_{ep} . The best performance that the Nb HEP's can achieve³³ is $NEP = 3 \times 10^{-13} \text{ W/Hz}^{1/2}$, detectivity $D^* = 4 \times 10^{11} \text{ cm s}^{1/2} \text{ J}^{-1}$, and a response time of 4.5 ns. Thus, these devices are less sensitive, although much faster, than semiconductor bolometers. When the detector area was adjusted properly, Nb HEP's demonstrated a constant value of sensitivity in the range from microwaves (150 GHz) to ultraviolet (10¹⁵ Hz). This is actually their greatest advantage when compared to semiconductor counterparts. A Nb-based HEP was implemented to study the emission of a cyclotron *p*-germanium laser.³⁴ The combination of large sensitivity and short response time made it possible to identify the Landau levels responsible for lasing.

In the late 1990s, the Gershenzon group developed a HEP based on NbN superconducting films.³⁵ NbN has much shorter τ_{ep} and τ_{pe} than Nb; thus, even for 3-nm-thick films, NbN HEP's operate in the mixed regime (i.e., τ_{ep} and τ_{es} jointly determine the response time of the detector). Detectors made from ultrathin NbN films are much faster than Nb-based devices. The intrinsic $\tau_{ep} \approx 10 \text{ ps}$, while the overall response time is about 30 ps near T_c .⁸ The best-demonstrated $NEP \approx 10^{-12} \text{ W/Hz}^{1/2}$ (Ref. 36). In spite of a rather-complicated electronic band structure,³⁷ the quantum yield in NbN reaches above 300 for near-infrared photons,³⁸ which corresponds to one-third of the upper theoretical limit. Detectors fabricated from NbN were used to study the emission of optically pumped

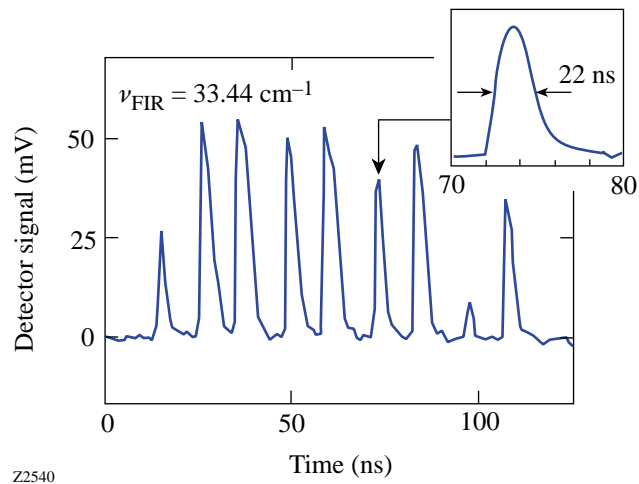


Figure 87.37

Pulses from a single-shot, optically pumped, far-infrared gas laser recorded with a NbN HEP (Ref. 39). The inset shows one of the pulses on an expended time scale.

infrared gas lasers, in particular, pulsed lasers.³⁹ Figure 87.37 shows far-infrared laser pulses recorded with a NbN hot-electron detector. The unique combination of response time and sensitivity made it possible to detect and identify very weak emission lines.

Miller *et al.*⁴⁰ have demonstrated a photon counter based on the transition-edge, hot-electron, direct detector. The device was a $20 \times 20\text{-}\mu\text{m}^2$ square of 40-nm-thick tungsten film (Fig. 87.38) having $T_c = 80\text{ mK}$ with a transition width of 1 mK. The device was operated at a bath temperature of 40 mK in a voltage-bias regime that maintained the sensor within the transition region via negative electrothermal feedback.⁴¹ This mode of operation was shown to increase the transition-edge sensor sensitivity and to decrease its time constant to $\tau_0/(1+\alpha/n)$. Here τ_0 is the intrinsic time constant of the sensor, n is the power of the temperature dependence of the thermal conductance between the film and substrate, and α is the dimensionless sharpness parameter of the superconducting transition.⁴¹ A photon absorbed in the sensor heats the electron system above its equilibrium temperature, leading to an increase of the sensor's resistance and, consequently, to the decrease of the bias current and dissipated joule power. The integral of the drop in current (read out by an array of dc SQUID's) gives the energy absorbed by the sensor with no free parameters. The detector described in Ref. 40 exhibited a time constant of about $60\text{ }\mu\text{s}$ and was able to register 0.3-eV (4- μm -wavelength) single photons with an energy resolution of 0.15 eV. To test the detector, the authors observed the planetary nebula NGC 6572, using the 8-in. telescope. The energy resolution was somewhat lower than in the laboratory, although it was high enough to detect the strong emission lines.

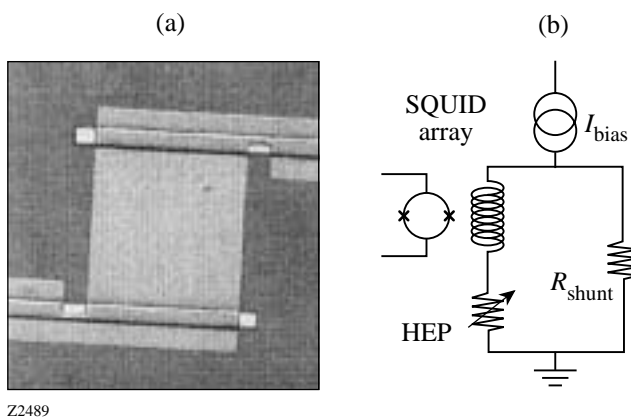


Figure 87.38
(a) Microphotograph of a transition-edge, hot-electron quantum detector and
(b) the corresponding equivalent circuit (Ref. 40).

A hot-electron microcalorimeter was developed by Nahum and Martinis.⁴² In this type of device, photon absorption gives rise to T_e in a metal absorber and is measured using the $I-V$ characteristics of a normal-insulator-superconductor tunnel junction, in which part of the absorber forms the normal electrode. Figure 87.39 shows a schematic of the tested device. The current through the junction was measured with a low-noise dc SQUID. The absorber had an area of $100 \times 100\text{ }\mu\text{m}^2$ and was deposited on a silicon nitride membrane. In this configuration, the phonons that escaped from the absorber were reflected back from the membrane and were further available for the energy exchange. Thus, the Si_3N_4 membrane prevented energy loss from the electron subsystem in the absorber. The microcalorimeter operated at 80 mK with a time constant of $15\text{ }\mu\text{s}$ and demonstrated an energy resolution of 22 eV for 6-keV photons.

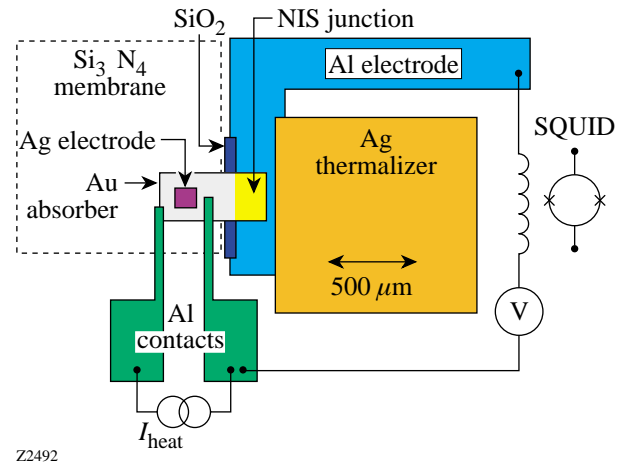


Figure 87.39
Detailed schematic of the hot-electron microcalorimeter developed by Nahum and Martinis (Ref. 42) (see text for explanation).

In another version, Nahum and Martinis⁴³ proposed a microbolometer that consisted of a normal metal stripe connected to superconducting electrodes (Fig. 87.40). The device relied on Andreev reflections of low-energy, thermal quasiparticles at the edges of the stripe and on weak electron–phonon coupling at low temperatures. Both effects confined the energy delivered by the photons, providing a large rise of T_e . This was subsequently read out by the superconductor-insulator-normal metal junction, for which the metal stripe formed the normal electrode. Projected responsivity and NEP of the device with the Cu absorber operated at 100 mK were about 10^9 V/W and $3 \times 10^{-18}\text{ W/Hz}^{1/2}$, respectively, which is at least a factor of 10 better than the performance of any currently available detectors. The time constant of the microcalorimeter is determined

by the rate of energy transfer from electrons to phonons that corresponds to τ_{ep} at the Fermi level. For the device under consideration in Ref. 43, the computed response time $\tau = 20 \mu\text{s}$. Since, for a bolometer, NEP scales as $\tau^{-1/2}$, the device performance can be further improved by increasing the response time up to a value only slightly less than that required by a specific application.

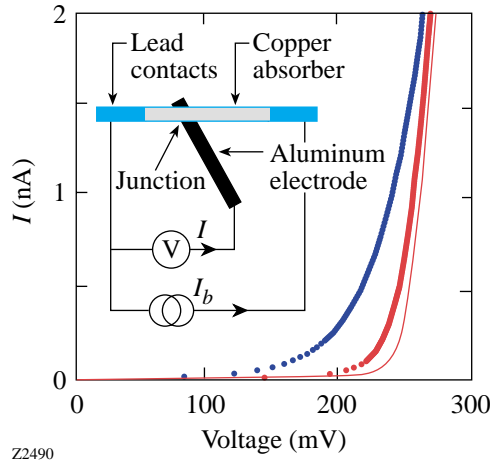


Figure 87.40

A hot-electron microbolometer using Andreev reflections of quasiparticles from superconducting contacts and the corresponding I - V characteristics (Ref. 43).

Finally, Karasik *et al.*⁴⁴ proposed the use of the dependence of the electron–phonon scattering time on the electron mean free path to control the intrinsic response time of a transition-edge detector. Increase of the intrinsic response time results in the decrease of the minimum detectable power, while at the same time, the device response time can be decreased to a reasonable value by exploiting the negative electrothermal feedback. According to estimates in Ref. 44, using this approach, a detector could be fabricated with $\text{NEP} = 10^{-20} \text{ W/Hz}^{1/2}$ and the millisecond τ at 100-mK bath temperature.

2. Superconducting Kinetic-Inductive Detectors

The detectors described in the preceding section produce a response when the device, or at least part of it, is in the resistive state. Kinetic-inductive integrating detectors represent their superconducting counterpart. The L_{kin} [see Eq. (7)] of a superconducting film makes it possible to monitor the concentration of Cooper pairs. In a constant current-biased superconducting film, after the destruction of a certain number of Cooper pairs, the remaining pairs accelerate to carry the same bias current. Because of non-zero inertia of pairs, or L_{kin} , acceleration requires an electric field. This intrinsically gener-

ated electric field is seen from the exterior as a voltage pulse developing across the film. Mathematically, this voltage transient is given by

$$V_{\text{kin}} = I \frac{dL_{\text{kin}}}{dt}. \quad (13)$$

Figure 87.34(b) presented earlier the V_{kin} transient, recorded for a YBCO microbridge excited by 100-fs optical pulses. The numerical fit was based on Eq. (13) and either Eqs. (1) or (6).

The main advantage of superconducting kinetic-inductive detectors is their low noise power. To realize this advantage, a SQUID readout should be used. Grossman *et al.*⁴⁵ described the design of a kinetic-inductive detector/mixer with an estimated $\text{NEP} = 2.5 \times 10^{-17} \text{ W/Hz}^{1/2}$ and a bandwidth of 5.5 MHz at 100 mK. Unfortunately, a laboratory prototype showed only $\text{NEP} = 4.4 \times 10^{-11} \text{ W/Hz}^{1/2}$ (Ref. 46). Sergeev and Reizer⁴⁷ performed thorough calculations for both *s*-wave and *d*-wave superconductors, including the appropriate quasi-particle distribution function and scattering times. They found NEP and D^* close to those reported in Ref. 45. Bluzer²³ proposed a balanced-bias scheme for a kinetic-inductive photodetector with directly coupled SQUID readout, intended to eliminate the losses inherent in inductively coupled readouts and increase the responsivity of the detector. Performance of the detector was simulated for a 0.1- μm -thick YBCO film at 9 K, resulting in $\text{NEP} = 2.5 \times 10^{-15} \text{ W/Hz}^{1/2}$ and 10- μs response time. It is believed that the use of a LTS material should result in a two- to three-orders-of-magnitude decrease in NEP .

3. Superconducting Quantum Detectors

A number of novel approaches proposed during the last decade have been aimed at the realization of detectors with ultimate quantum sensitivity. Kadin and Johnson²⁶ introduced the quantum detection regime in ultrathin resistive films. In the proposed mechanism, an absorbed photon induces a resistive hot spot, centered at the point where the photon hits the film. If the photon flux is sufficiently low, hot spots do not overlap until they disappear. Using material parameters of NbN, the authors estimated that a 0.1- μm^2 size sample should respond to 1-eV photons with 1-mV-amplitude pulses and 10-GHz bandwidth. For technological reasons, practical detectors would require significantly larger areas and, consequently, much smaller responsivities, forcing the implementation of a sophisticated readout scheme such as an array of SQUID's.²⁷

A photon counter using the quantum detection regime in a current-carrying superconducting film²⁸ was recently demonstrated by Gol'tsman *et al.*²⁹ The counting element consisted of a 1.3-μm-long, 0.2-μm-wide microbridge, formed from a 6-nm-thick NbN film deposited on a sapphire substrate. The detector was operated at 4.2 K, with a bias current of approximately 90% of I_c . Voltage pulses generated by the bridge in response to absorbed photons were further amplified by a cooled, low-noise amplifier (see Fig. 87.35). The output pulses were time limited by electronics and had a duration of approximately 100 ps. The intrinsic dark count rate for the detector was measured to be below 0.001 s⁻¹ (probability 10⁻⁶), which corresponds to zero detected responses over 1000 s when the input was completely blocked. Table 87.I presents the basic parameters of the device operated at the 790-nm wavelength. Single-photon counting was observed in the photon-wavelength range from 0.4 μm to 2.4 μm.⁴⁸ We note that the device represents a unique combination of the picosecond response time and very high responsivity. These characteristics of NbN HEP's should lead to their practical implementation in areas ranging from free-space satellite communication,⁴⁹ through quantum communication and quantum cryptography,⁵⁰ to ultraweak luminescence observations and semiconductor integrated circuit testing.⁵¹ Another exciting application for this type of detector can be background-limited direct detector arrays⁵² for submillimeter astronomy.

Table 87.I: Experimental performance of a NbN photodetector at 790 nm.

Response time— <i>intrinsic/measured</i>	10 ps/100 ps
Quantum gain factor	340
A/W responsivity	220 A/W
V/W responsivity	4×10^4 V/W
Device quantum efficiency	~20%
Operating temperature	~4 K
Dark counts per second	<0.0001
Device noise temperature	~15 K

The most-advanced superconducting quantum detectors are tunnel-junction detectors, which are being developed for a wide range of applications from materials science and microanalysis to particle physics and astrophysics. Only a few recent publications are mentioned here because a full review of the activities in this field is beyond the scope of this article. Nb-based tunnel-junction detectors with Al trapping layers

have reached, for photon energies of about 70 eV, an energy resolution of 1.9 eV. This performance is limited by the statistics of quasiparticle multiplication.⁵³ A typical device had an area of $50 \times 50 \mu\text{m}^2$. The smallest-detectable, 0.3-eV (4.1-μm-wavelength) photon energy was achieved with Ta-based devices⁵⁴ since this material has an energy gap smaller than that of Nb. An energy resolution of 0.19 eV was demonstrated for 2.5-eV (0.5-μm-wavelength) photons, using Ta-based devices with an area of $20 \times 20 \mu\text{m}^2$ and 12-μs response time.

Hot-Electron Mixers

Historically, HEM's have been divided into two large categories: lattice- or phonon-cooled¹³ and diffusion-cooled¹⁴ devices. As presented earlier, the physics for these two types of HEM's is essentially the same. Both types can be described by Eqs. (2) using temperature-dependent parameters and proper boundary conditions. The analysis becomes easier, however, when the device is designed to be close to one of two extremes, namely, the lattice- or the diffusion-cooling regime. Typically, lattice-cooled mixers are made from thin films of NbN, whereas diffusion-cooled devices use Nb or Al.

1. Lattice-Cooled Mixers

Current state-of-the-art NbN technology is capable of routinely delivering 3.0-nm-thick devices that are $500 \times 500 \text{ nm}^2$ in size with T_c above 9 K. Near T_c , τ_{pe} is close to τ_{es} , which is about 40 ps for 3-nm-thick film [see Fig. 87.30(b)]. The τ_{ep} at 8 K is below 20 ps, which results, with the diffusivity of 0.5 cm²s⁻¹, in a thermal healing length of about 30 nm. Since the device length is typically much larger, the mixer operates in the phonon-cooled regime. The mixer's intrinsic IF bandwidth is determined by the combination of τ_{ep} and τ_{es} time constants. In real devices, however, the measured bandwidth depends strongly on the bias regime. This makes it difficult to compare published data and reach meaningful conclusions. For HEM's on Si substrates, the best reported gain and noise bandwidths are 3.5 GHz⁵⁵ and 8 GHz,⁵⁶ respectively. Further increases in the bandwidth for lattice-cooled HEM's can be achieved by using a substrate material that is better thermally coupled to the superconducting film. One promising candidate is MgO. Recent measurements have shown⁵⁷ that MgO provides, for a 3.5-nm-thick bolometer, a 4.8-GHz gain bandwidth and 5.6-GHz noise bandwidth, respectively. Further progress in increasing the bandwidth may be achieved by decreasing the bolometer thickness. Recently a 9-GHz gain bandwidth was reported⁵⁸ for a 2.5-nm-thick device on MgO. Unfortunately, this direction is limited because NbN films thinner than 2.5 nm become inhomogeneous and lose their superconductivity.⁵⁹

A waveguide version of the receiver with the lattice-cooled NbN HEM has been installed and operated successfully in the frequency range of 0.6 to 0.8 THz⁶⁰ and 1.04 THz⁶¹ at the 10-m Sub-mm Telescope Facility on Mount Graham in Arizona. At this telescope, the measured noise temperature of the receiver was 560 K at 0.84 THz and 1600 K at 1.035 THz over a 1-GHz IF bandwidth centered at 1.8 GHz. The receiver was used to detect the CO molecular line emission in the Orion nebula (Fig. 87.41). It is worth noting that this was the first ground-based observation at a frequency above 1 THz. A quasi-optical version of the HEM receiver for the THz range is currently under preparation for test flights on a stratospheric airplane observatory.⁶² The mixer will be incorporated into a planar logarithmic spiral antenna (Fig. 87.42), which is integrated with an extended hyperhemispherical silicon lens.

Practical advantages of the lattice-cooled devices are their stability and the weak sensitivity of their noise temperature to operation parameters. Figure 87.43 shows that, indeed, the noise temperature of a NbN hot-electron mixer does not vary noticeably over a broad range of LO power and bias voltage.⁶³

2. Diffusion-Cooled Mixers

The bulk of diffusion-cooled mixers has been realized based on Nb films. At a 4.2-K bath temperature, the 10-nm-thick Nb film typically has τ_{ep} of about 1 ns and a diffusivity

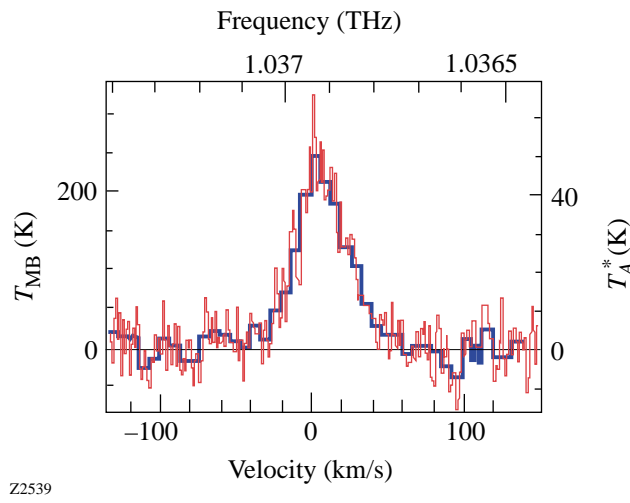


Figure 87.41

Terahertz CO line in the Orion IRc2 nebula recorded with a NbN hot-electron mixer at a ground-based telescope in Arizona (Ref. 61). The thick solid line shows a smoothed spectrum at a resolution of 25 MHz. The temperature scale of the spectrum is calibrated by taking into account the receiver noise temperature, the estimated atmospheric opacity, and the estimated efficiency of the telescope.

of $2 \text{ cm}^2 \text{s}^{-1}$,¹¹ which results in $L_{th} \approx 0.15 \mu\text{m}$. Therefore, Nb devices having a length of 0.1 μm or less operate in the diffusion-cooled regime. It has been shown experimentally⁶⁴ that the transition to diffusion cooling of electrons occurs at a

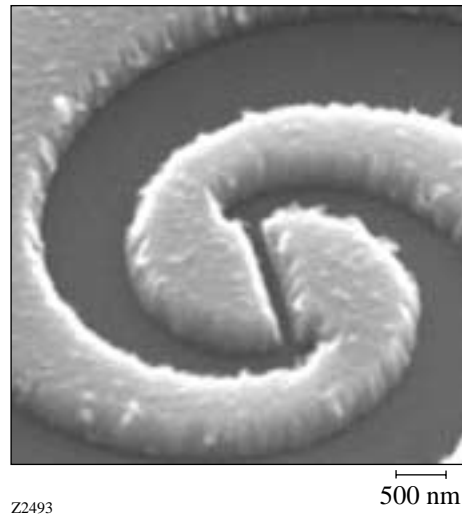


Figure 87.42

Central part of a planar logarithmic spiral antenna with the NbN hot-electron microbridge.

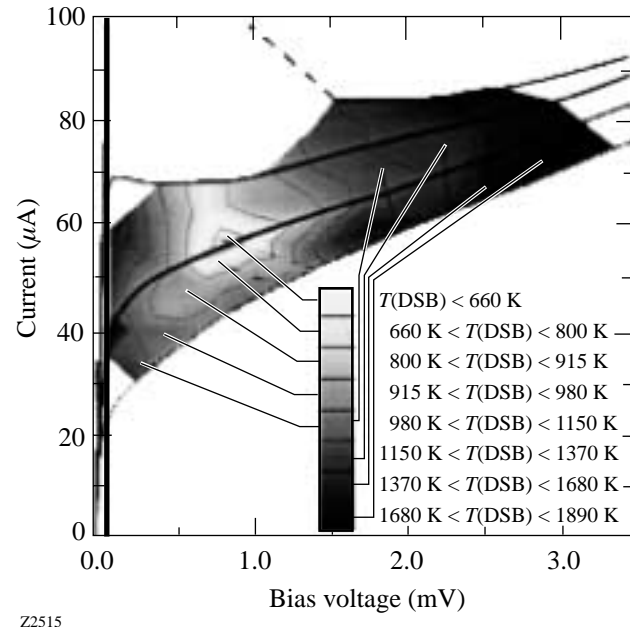


Figure 87.43

Double-sideband (DSB) noise temperature of a laboratory heterodyne receiver with NbN HEM at various bias regimes (Ref. 63).

device length $\approx 0.2 \mu\text{m}$. Expected gain bandwidth for a $0.1\text{-}\mu\text{m}$ -long device is about 7 GHz, if one assumes uniform electron heating through the length of the device. Laboratory tests at sub-THz frequencies confirmed theoretical expectations, and a 9-GHz gain bandwidth was measured for a $0.1\text{-}\mu\text{m}$ -long HEM.⁶⁵ No noise bandwidth data have been reported so far for diffusion-cooled mixers. Traditionally, quasi-optical, diffusion-cooled HEM's use a twin-slot or double-dipole planar antenna and a hemispherical lens to couple the LO and signal radiations to the mixer. The best reported noise temperatures for Nb diffusion-cooled mixers are presently almost twice as large as those of lattice-cooled devices.

Another apparent difference between the two types of HEM's is the optimal bias regime, i.e., the regime resulting in the lowest noise temperature. For a lattice-cooled HEM, the optimal bias point is within the linear portion of the nonhysteretic I - V characteristics,⁶³ whereas optimal operation of diffusion-cooled devices corresponds to the nonlinear portion of a hysteretic I - V curve.⁶⁵ The difference stems from boundary conditions imposed on the normal domain. Movement of the domain walls caused by signal radiation is not influenced by the contacts⁶⁶ if they are located far enough from the domain borders. One can envision such a domain as a freestanding domain in a stable equilibrium state. In the opposite case, when domain walls are confined near the contacts, the temperature profile at the walls slopes more steeply and the wall movement is restricted by the contacts. This hampers the responsivity of the HEM. As a result, the length of a diffusion-cooled mixer is smaller than the thermal diffusion length L_{th} and corresponds to the length of the smallest freestanding domain. Therefore, in a diffusion-cooled HEM, the conversion loss and, consequently, the noise temperature are smaller when the domain is “overcooled” and is slightly shorter than the smallest freestanding domain. The actual domain length, as seen from the resistance in the normal state at the optimal operation point,⁶⁵ is about 0.6 of the mixer physical length, whereas for phonon-cooled HEM's,⁶³ the domain length is 0.2 of the device length. Since the total noise power at the HEM output is partly due to Nyquist noise, smaller responsivity should result in a somewhat larger noise temperature. Another disadvantage of the diffusion-cooled HEM is that its hysteretic regime may cause additional instability⁶⁷ when accessed by a practical receiver.

For both mixer types, it is common that optimal operation, aimed at the minimal noise temperature, does not provide the largest-possible IF bandwidth. Both the bandwidth and the noise temperature increase with the bias current. Thus, varying the bias regime allows a compromise between the desired

bandwidth and the noise temperature acceptable for a particular application.

A diffusion-cooled Al mixer has been recently proposed⁶⁸ as an alternative to Nb devices. Measurements at 30 GHz⁶⁹ showed that a diffusion-cooled Al mixer exhibits reasonably good performance, but these data are not conclusive for the desired THz operation since the quantum energy of 30-GHz photons remains smaller than the Al energy gap. Moreover, there are concerns¹⁹ that Al HEM's at THz frequencies would require a large LO power.

Table 87.II and Fig. 87.44 summarize the current state-of-the-art noise temperatures for both the lattice-cooled and diffusion-cooled HEM's. The rapid increase in noise temperature with frequency is inconsistent with the hot-electron model. The model suggests that the noise temperature, when corrected for optical losses, should not depend on frequency unless it approaches the quantum-limited value $h\nu/k_B$. A proper account of losses in coupling optics does not eliminate the above discrepancy; the noise temperature of the mixer alone increases with frequency, following closely the $10 h\nu/k_B$ law in the frequency range from 0.6 THz to 5.2 THz. It has been shown recently⁶⁴ that the nonuniform distribution of the high-frequency current across the device may account for this effect.

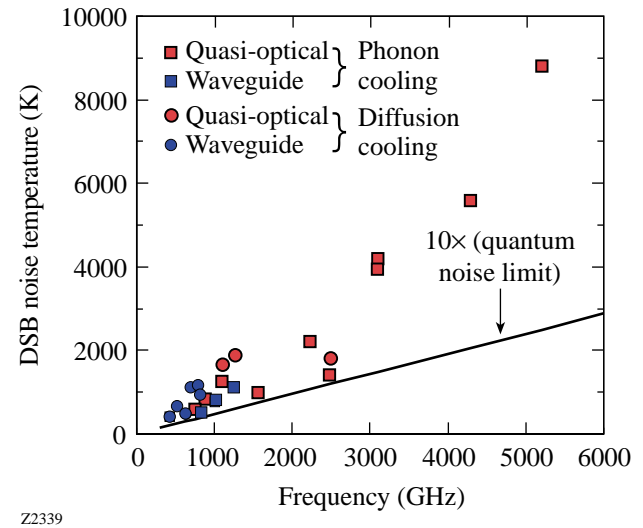


Figure 87.44

Best double-sideband (DSB) noise temperatures for various types of superconducting hot-electron mixers as a function of signal frequency. The solid line is the hot-electron model prediction.

In Fig. 87.45, simulated frequency dependence of the conversion efficiency is compared with the noise temperature corrected for optical losses. Good agreement between the experimental and theoretical results up to 4 THz suggests that the increase in the noise temperature should be less pronounced for narrower HEM's.

Conclusions

Superconductor hot-electron radiation sensors, operated as either THz-frequency mixers or optical single-photon detectors, promise a revolutionary approach for diagnostics, radio astronomy, and quantum cryptography and communications. The unique performance of these devices in heterodyne as well as in the direct-detection regime results from a combination of the hot-electron phenomenon with the high sensitivity of a superconductor to nonequilibrium electronic states. To take full advantage of this combination, devices are routinely fabricated from ultrathin superconducting films and feature sub-micron lateral dimensions. They are also operated in the very-low-noise cryogenic environment.

HEM's proved their reliability and advantageous features during a two-year test on a ground-based telescope. In the frequency range from 1 THz to 5.2 THz, HEM's outperformed Schottky diodes, making them the device-of-choice for THz astronomy and communications.

HEP's demonstrated excellent performance in the spectral range from far-infrared wavelengths to x rays when operated in either integrating or quantum regimes. Their future applications are expected in areas ranging from background-limited detector arrays for submillimeter astronomy and x-ray spectroscopy, through practical, high-speed quantum cryptography, to digital integrated-circuit diagnostics.

ACKNOWLEDGMENT

The authors thank S. Cherednichenko for helpful discussions and S. Svechnikov for systemizing published data. This research was made possible in part by Award No. RE-2227 of the U.S. Civilian Research and Development Foundation for the Independent States of the Former Soviet Union. G. N. Gol'tsman acknowledges support of the INTAS (#97-1453, #99-569). R. Sobolewski acknowledges support of the U.S. Office of Naval Research grant N00014-00-1-0237.

Table 87.II: Best double-sideband (DSB) noise temperatures reported in the literature for lattice-cooled and diffusion-cooled mixers.

Lattice-cooled mixers					
Quasi-optical layout			Waveguide layout		
Frequency (GHz)	DSB noise temperature (K)	Reference	Frequency (GHz)	DSB noise temperature (K)	Reference
620	500	70	430	410	73
750	600	65	636	483	73
910	850	65	840	490	61
1100	1250	65	1017	750	61
1560	1000	71	1030	800	61
1620	700	58	1260	1100	61
2240	2200	71			
2500	1100	58			
3100	4000	72			
4300	5600	72			
5200	8800	72			
Diffusion-cooled mixers					
Quasi-optical layout			Waveguide layout		
Frequency (GHz)	DSB noise temperature (K)	Reference	Frequency (GHz)	DSB noise temperature (K)	Reference
630	470	64	530	650	76
1100	1670	74	700	1100	17
1267	1880	75			
2500	1800	64			

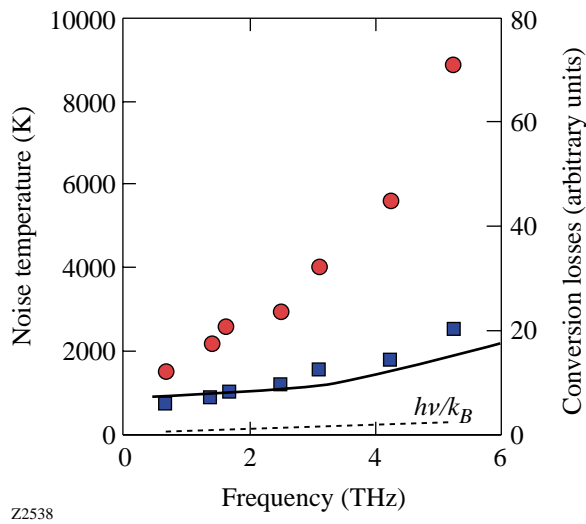


Figure 87.45

Frequency dependence of the noise temperature (circles) and conversion losses (squares) of a NbN HEM (Ref. 68). The solid line shows the calculated conversion losses that account for the skin effect in the device. The dashed line represents quantum-limited noise temperature $h\nu/k_B$. The scale of the right axis was adjusted to match calculated conversion losses and corrected noise temperature.

REFERENCES

1. E. M. Conwell, *High Field Transport in Semiconductors*, Solid State Physics Supplement 9 (Academic Press, New York, 1967).
2. M. L. Kaganov, I. M. Lifshitz, and L. V. Tanatarov, Sov. Phys.-JETP **4**, 173 (1957).
3. V. A. Schklovski, [Sov. Phys.] FTT **17**, 3076 (1975).
4. N. Perrin and C. Vanneste, Phys. Rev B **28**, 5150 (1983).
5. A. D. Semenov *et al.*, Phys. Rev. B **52**, 581 (1995).
6. E. M. Gershenson *et al.*, Sov. Phys.-JETP **59**, 442 (1984).
7. M. Lindgren *et al.*, Appl. Phys. Lett. **65**, 3398 (1994).
8. K. S. Il'in, M. Lindgren, M. Currie, A. D. Semenov, G. N. Gol'tsman, R. Sobolewski, S. I. Cherednichenko, and E. M. Gershenson, Appl. Phys. Lett. **76**, 2752 (2000).
9. M. Lindgren, M. Currie, C. Williams, T. Y. Hsiang, P. M. Fauchet, R. Sobolewski, S. H. Moffat, R. A. Hughes, J. S. Preston, and F. A. Hegmann, IEEE J. Sel. Top. Quantum Electron. **2**, 668 (1996).
10. R. Sobolewski, in *Superconducting and Related Oxides: Physics and Nanoengineering III*, edited by D. Pavuna and I. Bozovic (SPIE, Bellingham, WA, 1998), Vol. 3481, pp. 480–491.
11. E. M. Gershenson *et al.*, Sov. Phys.-JETP **70**, 505 (1990).
12. E. M. Gershenson *et al.*, Sov. Phys.-Tech. Phys. **34**, 195 (1989).
13. E. M. Gershenson *et al.*, Supercond., Phys. Chem. Technol. **3**, 1582 (1990); B. S. Karasik and A. I. Elantiev, Appl. Phys. Lett. **68**, 853 (1996).
14. D. E. Prober, Appl. Phys. Lett. **62**, 2119 (1993).
15. R. S. Nebosis *et al.*, in *Proceedings of the Seventh International Symposium on Space Terahertz Technology* (University of Virginia, Charlottesville, VA, 1996), pp. 601–613.
16. B. S. Karasik, W. R. McGrath, and M. C. Gaidis, J. Appl. Phys. **81**, 1581 (1997).
17. W. D. Floet *et al.*, in *Proceedings of the Tenth International Symposium on Space Terahertz Technology* (University of Virginia, Charlottesville, VA, 1999), pp. 228–236.
18. H. Merkel *et al.*, IEEE Trans. Appl. Supercond. **9**, 4201 (1999).
19. A. D. Semenov and G. N. Gol'tsman, J. Appl. Phys. **87**, 502 (2000).
20. H. Ekström *et al.*, IEEE Trans. Microw. Theory Tech. **43**, 938 (1995).
21. A. Rothwarf and B. N. Taylor, Phys. Rev. Lett. **19**, 27 (1967).
22. E. N. Grossman, D. G. McDonald, and J. E. Sauvageau, IEEE Trans. Magn. **27**, 2677 (1991).
23. N. Bluzer, J. Appl. Phys. **78**, 7340 (1995).
24. A. D. Semenov *et al.*, IEEE Trans. Appl. Supercond. **7**, 3083 (1997).
25. M. Lindgren, M. Currie, C. A. Williams, T. Y. Hsiang, P. M. Fauchet, R. Sobolewski, S. H. Moffat, R. A. Hughes, J. S. Preston, and F. A. Hegmann, IEEE J. Sel. Top. Quantum Electron. **2**, 668 (1996).
26. A. M. Kadin and M. W. Johnson, Appl. Phys. Lett. **69**, 3938 (1996).
27. D. Gupta and A. M. Kadin, IEEE Trans. Appl. Supercond. **9**, 4487 (1999).
28. A. D. Semenov, G. N. Gol'tsman, and A. A. Korneev, Physica C **351**, 349 (2001).
29. G. N. Gol'tsman, O. Okunev, G. Chulkova, A. Lipatov, A. Semenov, K. Smirnov, B. Voronov, A. Dzardanov, C. Williams, and R. Sobolewski, Appl. Phys. Lett. **79**, 705 (2001).
30. D. Twerenbold, Phys. Rev. B **34**, 7748 (1986).
31. Th. Nussbaumer *et al.*, Phys. Rev. B **61**, 9719 (2000).
32. E. M. Gershenson *et al.*, JETP Lett. **34**, 268 (1981).
33. E. M. Gershenson *et al.*, Sov. Tech. Phys. Lett. **15**, 118 (1989).
34. A. V. Bespalov *et al.*, Solid State Commun. **80**, 503 (1991).
35. B. M. Voronov *et al.*, Supercond., Phys. Chem. Technol. **5**, 960 (1992).
36. Yu. P. Gousev *et al.*, J. Appl. Phys. **75**, 3695 (1994).

37. S. V. Vonsovskii, Iu. A. Iziumov, and E. Z. Kurmaev, *Superconductivity of Transition Metals: Their Alloys and Compounds*, Springer Series in Solid-State Sciences (Springer-Verlag, Berlin, 1982).
38. K. S. Il'in, I. I. Milostnaya, A. A. Verevkin, G. N. Gol'tsman, E. M. Gershenson, and R. Sobolewski, *Appl. Phys. Lett.* **73**, 3938 (1998).
39. P. T. Lang *et al.*, *Appl. Phys. B* **B53**, 207 (1991); P. T. Lang *et al.*, *Opt. Lett.* **17**, 502 (1992).
40. A. J. Miller *et al.*, *IEEE Trans. Appl. Supercond.* **9**, 4205 (1999).
41. K. D. Irwin, *Appl. Phys. Lett.* **66**, 1998 (1995).
42. M. Nahum and J. M. Martinis, *Appl. Phys. Lett.* **66**, 3203 (1995); K. D. Irwin *et al.*, *Nucl. Instrum. Methods Phys. Res. A* **444**, 184 (2000).
43. M. Nahum and J. M. Martinis, *Appl. Phys. Lett.* **63**, 3075 (1993).
44. B. S. Karasik *et al.*, *Supercond. Sci. Technol.* **12**, 745 (1999).
45. E. N. Grossman, D. G. McDonald, and J. E. Sauvageau, *IEEE Trans. Magn.* **27**, 2677 (1991).
46. J. E. Sauvageau, D. G. McDonald, and E. N. Grossman, *IEEE Trans. Magn.* **27**, 2757 (1991).
47. A. V. Sergeev and M. Yu. Reizer, *Int. J. Mod. Phys. B* **10**, 635 (1996).
48. G. N. Gol'tsman, O. Okunev, G. Chulkova, A. Lipatov, A. Dzardanov, K. Smirnov, A. Semenov, B. Voronov, C. Williams, and R. Sobolewski, *IEEE Trans. Appl. Supercond.* **11**, 574 (2001).
49. G. G. Ortiz, J. V. Sandusky, and A. Biswas, in *Free-Space Laser Communication Technologies XII*, edited by G. S. Mercherle (SPIE, Bellingham, WA, 2000), Vol. 3932, pp. 127–138.
50. G. Gilbert and M. Hamrick, “Practical Quantum Cryptography: A Comprehensive Analysis (Part One),” to appear in *Phys. Rep.*; see also <http://xxx.lanl.gov/abs/quant-ph/0009027>.
51. J. C. Tsang and J. A. Kash, *Appl. Phys. Lett.* **70**, 889 (1997).
52. G. Gol'tsman *et al.*, “Background Limited Quantum Superconducting Detector for Submillimeter Wavelengths,” to be published in the *Proceedings of the Twelfth International Symposium on Space Terahertz Technology*.
53. S. Friedrich *et al.*, *IEEE Trans. Appl. Supercond.* **9**, 3330 (1999).
54. P. Verhoeve *et al.*, *IEEE Trans. Appl. Supercond.* **7**, 3359 (1997).
55. S. Cherednichenko *et al.*, in *Proceedings of the Eighth International Symposium on Space Terahertz Technology* (Harvard University, Cambridge, MA, 1997), pp. 245–252.
56. H. Ekström *et al.*, *Appl. Phys. Lett.* **70**, 3296 (1997).
57. S. Cherednichenko *et al.*, in *Proceedings of the Eleventh International Symposium on Space Terahertz Technology* (Ann Arbor, MI, 2000), pp. 219–227.
58. M. Kroug *et al.*, *IEEE Trans. Appl. Supercond.* **11**, 962–965 (2001).
59. B. M. Voronov, Moscow State Pedagogical University, private communication (2000).
60. J. H. Kawamura *et al.*, *IEEE Trans. Appl. Supercond.* **9**, 3753 (1999); J. H. Kawamura *et al.*, *Publ. Astron. Soc. Pac.* **111**, 1088 (1999).
61. C.-Y. E. Tong *et al.*, in *Proceedings of the Eleventh International Symposium on Space Terahertz Technology*, (Ann Arbor, MI, 2000), pp. 49–59.
62. H.-W. Huebers *et al.*, in *Airborne Telescope Systems*, edited by R. K. Melugin and H.-P. Roeser (SPIE, Bellingham, WA, 2000), Vol. 4014, pp. 195–202.
63. P. Yagoubov *et al.*, *Appl. Phys. Lett.* **73**, 2814 (1998).
64. P. J. Burke *et al.*, *Appl. Phys. Lett.* **68**, 3344 (1996).
65. R. A. Wyss *et al.*, in *Proceedings of the Tenth International Symposium on Space Terahertz Technology* (University of Virginia, Charlottesville, VA, 1999), pp. 215–228.
66. A. D. Semenov and H.-W. Hubers, *IEEE Trans. Appl. Supercond.* **11**, 196 (2001).
67. A. D. Semenov *et al.*, *J. Appl. Phys.* **88**, 6758 (2000).
68. B. S. Karasik and W. R. McGrath, in *Proceedings of the Ninth International Symposium on Space Terahertz Technology* (1998), p. 73.
69. I. Siddiqi *et al.*, in *Proceedings of the Eleventh International Symposium on Space Terahertz Technology*, (Ann Arbor, MI, 2000), pp. 82–94.
70. P. Yagoubov *et al.*, *Supercond. Sci. Technol.* **12**, 989 (1999).
71. E. Gerecht *et al.*, in *Proceedings of the Tenth International Symposium on Space Terahertz Technology* (University of Virginia, Charlottesville, VA, 1999), pp. 200–207.
72. J. Schubert *et al.*, *Supercond. Sci. Technol.* **12**, 748 (1999).
73. J. Kawamura *et al.*, in *Proceedings of the Eighth International Symposium on Space Terahertz Technology* (Harvard University, Cambridge, MA, 1997), pp. 23–26.
74. A. Skalare *et al.*, in *Proceedings of the Ninth International Symposium on Space Terahertz Technology* (1998), pp. 115–120.
75. A. Skalare *et al.*, *IEEE Trans. Appl. Supercond.* **7**, 3568 (1997).
76. A. Skalare *et al.*, *Appl. Phys. Lett.* **68**, 1558 (1996).

Scaling Law for Marginal Ignition

Introduction

In recent years, a considerable effort^{1–6} has been made to determine the minimum energy required for ignition in inertial confinement fusion (ICF) implosions. Though different conclusions have been reached by different authors, consensus is that the minimum energy required for ignition is a strong function of the shell implosion velocity as well as the shell adiabat. Various approaches to the study of ignition have led to scaling laws in which the shell kinetic energy required for ignition is given as a function of the implosion velocity, shell adiabat (in-flight and at stagnation), and other parameters such as the applied pressure at the end of the acceleration phase. Scientists from Lawrence Livermore National Laboratory (LLNL) have produced a scaling law^{1,5} for marginal ignition by fitting a large database of *LASNEX* simulations of implosions with gain approximately equal to unity. The first scaling law by Levedahl and Lindl (LL)¹ was obtained by fitting the shell kinetic energy with the in-flight shell adiabat and the shell implosion velocity. The LL scaling law yields

$$E_k \sim \frac{\beta_{if}^{1.7}}{V_{imp}^{5.5}}, \quad (1)$$

where E_k is the shell kinetic energy at the end of the acceleration phase, β_{if} is the in-flight shell adiabat, and V_{imp} is the shell implosion velocity. In the derivation of Eq. (1), the different hydrodynamic quantities have been rescaled by keeping the initial pressure constant. A similar result was also obtained by Piriz.² Later, Basko and Johner (BJ) derived a similar scaling law⁴ from a set of numerical simulations based on a self-similar rescaling of the hydrodynamic quantities. Their conclusion is that the minimum energy required for ignition scales as

$$E_k \sim \frac{\beta_{if}^3}{V_{imp}^{9.1}}. \quad (2)$$

At first glance, the BJ scaling appears quite different from the LL scaling; however, it must be emphasized that the hydrodynamic similarity used by Basko and Johner requires that the pressure scales as $P \sim V_{imp}^5 \beta_{if}^{-1.5}$ in contrast with the $P \sim \text{constant}$ assumption used in the derivation of the LL scaling. Relations (1) and (2) seem at odds with the standard static assembled scaling based on the isobaric model of Meyer-ter-Vehn,⁷

$$E_k \sim \frac{J_s^3 \beta_s^3}{V_{imp}^{10}}, \quad (3)$$

where β_s is the stagnation adiabat and $J_s \equiv \rho_s R_s T_s$ with ρ_s , R_s , and T_s representing the hot-spot density, radius, and temperature at stagnation.

It is important to emphasize that the shell adiabat used in Eq. (3) is calculated at stagnation and its value differs from the in-flight adiabat used in Eqs. (1) and (2). This point was not made by Basko and Johner, who did not distinguish between the in-flight and stagnation adiabats. It follows that a comparison between Eq. (3) and Eqs. (1) and (2) cannot be made unless a relation between the in-flight and stagnation adiabats is derived. Thus Eq. (3) and Eqs. (1) and (2) represent two different scalings that we denote as the “stagnation” scaling and “in-flight” scaling, respectively.

Another important point concerning the ignition condition is the following: If ignition is triggered at a fixed value of J_s (as commonly assumed), Eq. (3) yields a stagnation scaling

$$E_k \sim \frac{\beta_s^3}{V_{imp}^{10}}. \quad (4)$$

This result disagrees with the stagnation scaling recently found by Herrmann, Tabak, and Lindl (HTL)⁵ based on a numerical fit of *LASNEX* runs leading to

$$E_k \sim \frac{\beta_s^{2.66}}{V_{\text{imp}}^{7.2}}. \quad (5)$$

Basko and Johner⁴ pointed out that the condition $J_s = \text{constant}$ does not correctly represent the ignition conditions because it neglects the tamping effect of the shell. This is important because the shell's inertia determines the hot-spot disassembly time. Basko and Johner estimated analytically that, at ignition, J_s depends linearly on the implosion velocity $J_s \sim V_{\text{imp}}$, thus leading to the modified ignition scaling [from Eq. (3)]

$$E_k \sim \frac{\beta_s^3}{V_{\text{imp}}^7}. \quad (6)$$

Basko and Johner revised this scaling⁴ through a set of numerical simulations starting from the assembled state and derived what they define as the “dynamic assembled state scaling”

(7)

With the exception of minor differences in the exponents, all the stagnation scalings [Eqs. (5)–(7)] seem to agree and corroborate the argument that J_s is proportional to the implosion velocity or to some power (<1) of it.

Herrmann *et al.*⁵ revised the in-flight scaling of Levedahl and Lindl through a series of LASNEX simulations, allowing for changes in the shell pressure at the end of the acceleration phase, and concluded that the energy scaling in terms of the in-flight variables can be approximated by the following fit:

$$E_k \sim \frac{\beta_{\text{if}}^{1.8}}{V_{\text{imp}}^{5.8} P_a^{0.77}}, \quad (8)$$

where P_a is the applied pressure at the end of the acceleration phase (i.e., at the peak of the shell kinetic energy). It is important to notice that the in-flight HTL scaling [Eq. (8)] reproduces the in-flight BJ scaling [Eq. (2)] when the self-similar hydrodynamic scaling for the pressure $P \sim V_{\text{imp}}^5 / \beta_{\text{if}}^{3/2}$ is substituted into Eq. (8). Recently, Kemp, Meyer-ter-Vehn, and Atzeni (KMA)⁶ analytically reproduced a scaling law that resembles the in-flight HTL scaling [Eq. (8)]:

$$E_k \sim J_s^3 \frac{\beta_{\text{if}}^{1.8}}{V_0^6 P_0^{0.8}}. \quad (9)$$

Equation (9) was derived from a self-similar solution of an imploding shell where P_0 and V_0 are the peak pressure and velocity at the time of void closure. Even though it is unclear how to relate P_0 in Eq. (9) to P_a in the HTL scaling [Eq. (8)], the two scaling laws are strikingly similar if J_s is constant at the onset of ignition. However, if J_s scales linearly with the implosion velocity as suggested by Basko,³ the KMA scaling will produce a weak dependence on the implosion velocity and significantly deviate from the HTL scaling. Another important conclusion of the KMA self-similar solution is that the stagnation adiabat is related to its in-flight value through the shell Mach number:

$$\beta_s \sim \beta_{\text{if}} \sqrt{M_A} \sim \beta_{\text{if}}^{0.85} V_{\text{imp}}^{0.5} P_0^{-0.1}, \quad (10)$$

where M_A is the shell Mach number. A similar scaling between the adiabats was also derived in Ref. 5 through a fit of the LASNEX simulation database, yielding

$$\beta_s \sim \beta_{\text{if}}^{0.75} V_{\text{imp}}^{0.44} P_a^{-0.21}. \quad (11)$$

Observe that the HTL scaling [Eq. (8)] can also be approximately derived from the stagnation scaling [Eqs. (5)–(7)] by using Eq. (11) to relate the stagnation and in-flight adiabats.

Though many discrepancies have been resolved with regard to the different scalings, it is important to note that some differences persist. In particular, the analytic KMA scaling [Eq. (9)] reproduces the in-flight HTL scaling [Eq. (8)] only if J_s is independent of the implosion velocity. On the other hand, the stagnation scaling in Eq. (3) reproduces the stagnation HTL scaling [Eq. (5)] only if $J_s \sim V_{\text{imp}}$, as proposed by Basko and Johner. This leads to the paradox that the two analytic theories leading to Eqs. (3) and (6) and Eq. (9) match the numerical fits only when different ignition conditions are used ($J_s = \text{constant}$ or $J_s \sim V_{\text{imp}}$).

In this article, a new model is developed to determine the marginal ignition conditions and the minimum kinetic energy required for ignition. This model includes the propagation of the return shock through the shell and the change of the shell adiabat as well as the most-relevant ignition physics such as alpha-particle heating and heat-conduction losses. It repro-

duces BJ scaling and HTL scaling with respect to the stagnation adiabat, indicating that J_s is indeed proportional to the implosion velocity. Furthermore, the model yields a relation between the stagnation and in-flight adiabats that is in general agreement with the KMA scaling and the HTL scaling [Eqs. (10) and (11)].

The following sections of this article (1) describe hot-spot dynamics and shell dynamics; (2) derive the ignition scalings with respect to the stagnation adiabat; (3) relate the stagnation adiabat to the in-flight adiabat and derive the “in-flight” scaling; and (4) verify *a posteriori* all the assumptions concerning the hot-spot hydrodynamics.

Hot-Spot Dynamics

The hot spot is a low-density plasma heated by the shock and by the PdV work of the cold, dense surrounding shell. It is made of ionized DT gas and the plasma ablated off the inner shell surface. Its dynamics are determined by the compression of the shell, the energy conduction and radiation losses, and the alpha heating.

As the hot spot is formed after the shock reflection, its temperature is typically large enough that its sound speed is larger than the flow velocity. Therefore, it is a good approximation to neglect the hot-spot kinetic energy with respect to its internal energy throughout the assembly and ignition stages of the hot spot. Another consequence of the subsonic flow assumption is that the pressure is equilibrated and the pressure profile is flat within the hot spot, i.e., $P_{hs} = P_{hs}(t)$.

Bremsstrahlung radiation energy losses can also be neglected because their contribution is typically smaller than that of the mechanical work and/or the fusion power. The magnitude of the radiation losses is larger than the fusion power for temperatures below 4.4 keV, when the PdV work rate is typically greater than both radiation and fusion power. Thus, at such low temperatures, both radiation losses and alpha heating power are negligible with respect to the compression work rate. The PdV work rate decreases as the shell approaches the stagnation point, while higher temperatures are reached within the hot spot. If these temperatures are well above 4.4 keV, the alpha power is greater than the radiation losses and the bremsstrahlung term can again be neglected in the energy equation.

Another simplification is the assumption that the alpha particles are locally deposited. This approximation requires a condition on the hot-spot temperature and areal density that

can be satisfied for sufficiently large implosion velocities. Indeed, it will be shown *a posteriori* [Eq. (10)] that both bremsstrahlung radiation and alpha-particle diffusion can be neglected as long as the implosion velocity is larger than a critical value.

Based on previous assumptions, the energy conservation equation for the hot spot includes the PdV work of the shell, the conduction energy losses, the alpha-particle heating, and the change in internal energy:

$$\frac{3}{2} \frac{\partial}{\partial t} P + \nabla \cdot \left[\frac{5}{2} \mathbf{v} P \right] = \nabla \cdot \kappa(T) \nabla T + \frac{\rho^2}{4M_i^2} E_\alpha \langle \sigma v \rangle, \quad (12)$$

where ρ is the hot-spot density, M_i is the ion mass, $E_\alpha \approx 3.5$ MeV is the alpha-particle energy, $\kappa(T) \approx \kappa_0 T^{5/2}$ is Spitzer thermal conductivity, and $P \approx P_{hs}(t)$ for subsonic flows.

Following Ref. 8, we integrate Eq. (12) over the hot-spot volume enclosed by the inner shell surface and approximate the fusion cross section with the quadratic form $\langle \sigma v \rangle \approx S_\alpha T^2$ with $S_\alpha \approx 10^{-18} \text{ cm}^3 \text{s}^{-1} \text{ keV}^{-2}$. Figure 87.46 shows that the error produced by the T^2 approximation of $\langle \sigma v \rangle$ is less than 30% for $6 < T < 25$ keV. At the inner surface, the shell material is cold and the thermal conduction can be neglected. This leads to the following form of the integrated energy equation:

$$\begin{aligned} \frac{d}{dt} (P_{hs} R_{hs}^3) + 3R_{hs}^2 P_{hs} \left[\frac{5}{3} U(R_{hs}, t) - \frac{dR_{hs}}{dt} \right] \\ = \sum_\alpha P_{hs}^2 R_{hs}^3, \end{aligned} \quad (13)$$

where $U(R_{hs}, t)$ is the flow velocity at the shell inner surface and $\sum_\alpha \equiv E_\alpha S_\alpha / 24$. The flow velocity results from the combination of the inner surface motion and the ablative flow, $U(R_{hs}, t) = \dot{R}_{hs} - V_a$, where V_a is the ablation velocity and \dot{R}_{hs} scales with the implosion velocity. Since $V_a \ll \dot{R}_{hs}$, the ablation velocity⁸ can be neglected and Eq. (13) can be rewritten in the simplified form

$$\dot{R}_{hs} + 5 P_{hs} \frac{\dot{R}_{hs}}{R_{hs}} = \sum_\alpha P_{hs}^2. \quad (14)$$

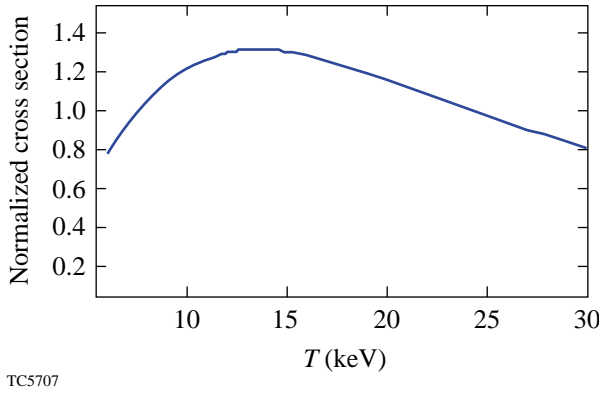


Figure 87.46

Plot of the normalized fusion cross section $\langle\sigma v\rangle/0.97 \times 10^{-18} T (\text{keV})^2$ between 6 and 30 keV. The maximum error is 27%. (The reference cross section is taken from Ref. 9.)

Note that the heat conduction losses do not enter into the global energy balance of the hot spot because the heat flux leaving the hot spot is deposited onto the inner shell surface. A fraction of this energy is transformed into internal energy of the shell material ablating into the hot spot. The remaining fraction produces the PdV work done by the ablated plasma entering the hot spot against the hot-spot pressure. In other words, the energy leaving the hot spot in the form of heat conduction losses goes back into the hot spot in the form of internal energy and compression work of the ablated plasma. Therefore, conduction losses do not affect the global energy balance of the hot spot and therefore do not represent net energy losses to the hot spot, as shown by Eq. (14). It is important to emphasize that the hot-spot energy is proportional to its pressure. The conduction losses do affect the hot-spot temperature but not its pressure. This conclusion implies that greater conduction losses would lower the temperature and raise the density (through larger ablation at the shell inner surface), leaving the pressure ($P \sim \rho T$) unaltered.

The next step is to couple the hot-spot-energy equation [Eq. (14)] with the shell dynamics through the shell momentum conservation and to determine the hot-spot radius as a function of the hot-spot pressure.

Shell Dynamics

In the initial stage of the deceleration phase, the hot spot is heated and compressed by the piston action of the shell. If a sufficiently large pressure is reached within the hot spot, a thermal instability is driven by the absorbed fusion power, leading to a rapid increase of the hot-spot energy. This instabil-

ity is referred to as “thermonuclear ignition.” In this section, we develop a simple model describing the shell motion and combine the shell and hot-spot equations in order to construct a self-consistent model of the deceleration phase and hot-spot ignition.

As mentioned in Ref. 8, the deceleration phase starts after the shock reflected from the center of the capsule interacts with the incoming shell. For simplicity, we assume that after the first shock reflects off the shell, all subsequent shocks are weak and do not produce large pressure jumps within the hot spot or the shell. For this reason, we refer to our model as the “one-shock model.” If multiple shocks are launched during the acceleration phase and do not merge into one before reaching the shell center but instead converge to the center at different times, the one-shock model may not be valid. After interacting with the shell, the return shock travels within the shell material and eventually reaches the shell’s outer surface.

Two shell configurations have been considered: the thin incompressible shell and the thick compressible shell. The thin shell model assumes that the shock reaches the outer shell surface immediately and that the whole shell acts like a rigid piston on the hot spot. This model is simple and provides useful physical insight into the ignition problem. However, it leads to a significant underestimation of the ignition energy requirements for two reasons: First, this model assumes that the entire shell kinetic energy is transformed into hot-spot internal energy at stagnation. Second, it does not include the shell decompression after the return shock has passed through the shell. ICF capsules are usually better described by the thick compressible shell model where the shock propagating through the shell divides it into two regions that provide compression work at different rates. At stagnation, the shock is still within the shell, and only the shocked part has released all its kinetic energy to the hot spot.

In Sec. 1, we determine the shell dynamics using the simple thin incompressible shell model. In Sec. 2, we derive the thick compressible shell model and determine all the relevant capsule properties, once the conditions at the beginning of the deceleration phase are known.

1. The Thin Incompressible Shell Model

To gain some physical insight into the shell dynamics, we consider the simple model of an incompressible shell of finite mass but infinitesimally small thickness.

The motion of the thin incompressible shell is governed by Newton's law balancing the shell inertia with the hot-spot pressure force:

$$M_{\text{sh}} \ddot{R}_{\text{hs}} = 4\pi R_{\text{hs}}^2 P_{\text{hs}}, \quad (15)$$

where M_{sh} is the shell mass. Here M_{sh} is constant and, according to the thin-shell approximation, the shell's center of mass coincides with the hot-spot radius. Note that the pressure applied to the shell's outer surface has been neglected since the laser is turned off during the deceleration phase. Equation (15) is combined with the hot-spot energy balance [Eq. (14)], which we rewrite in the following compact form:

$$\frac{d}{dt} \left[P_{\text{hs}} R_{\text{hs}}^5 \right] = \sum_{\alpha} P_{\text{hs}}^2 R_{\text{hs}}^5. \quad (16)$$

Equations (15) and (16) constitute a closed system of coupled differential equations that can be easily solved to determine the hot-spot pressure and shell position.

2. The Thick Compressible Shell Model

The thin incompressible shell model provides a useful qualitative understanding of the deceleration phase and hot-spot ignition. If the shell is incompressible, however, its mass supplies a uniform PdV work rate to the hot spot, and the thin shell model leads to optimistic predictions about the onset of ignition. For a more accurate quantitative estimate of the ignition conditions, it is appropriate to use a compressible model, including the return shock propagation through the shell. After the interaction with the shell's inner surface, the return shock travels within the shell material and eventually reaches the shell's outer surface. We let $R_k(t)$ denote the shock position within the shell. The shell material with $r < R_k$ is shocked and compressed, while the material with $r > R_k$ is in a "free-fall" condition. A free-fall condition is the state of the shell in the absence of a hot spot. Since the shock wave reflected from the center carries the information regarding the high pressure within the hot spot, it is reasonable to assume that the unshocked material is not aware of the presence of the hot spot and moves at constant velocity toward the center.

The shocked part of the shell behaves as a thin shell and acts like a piston on the hot spot. The unshocked part is in the free-fall (ff) condition and provides compression work rate through the flow of momentum across the shock. This flow of momentum, however, is proportional to $[\rho_{\text{ff}}]_{R_k}$ and for a given

implosion velocity can be small if the unshocked shell density ρ_{ff} is small. In simple words, a thick compressible shell does not act as a uniform piston. The material near the hot-spot surface provides PdV work at a faster rate than the material on the opposite side of the shock. The PdV work would be grossly overestimated if we were to assume that the entire shell mass is uniformly compressing the hot spot, as in the thin incompressible shell model.

a. Free-fall conditions. Free-fall conditions describe the dynamics of the unshocked part of the shell. Here a distinction is made between the coasting phase and free-fall conditions. The coasting phase represents the time interval after the laser is turned off and before the return shock has interacted with the shell. The free-fall conditions apply to the unshocked part of the shell after the shock–shell interaction. In the absence of the return shock, the shell travels inward at approximately constant velocity while its thickness increases due to the expansion of the shell material into its surroundings. We consider the following simple form for the density profile of a free-falling shell:

$$\rho_{\text{ff}}(r,t) = \frac{3M_{\text{sh}}}{\pi r^2} \frac{[r - R_{\text{in}}(t)]^2 [R_{\text{out}}(t) - r]}{\Delta_{\text{ff}}^4}, \quad (17)$$

where M_{sh} is the shell mass, $\Delta_{\text{ff}} = R_{\text{out}}(t) - R_{\text{in}}(t)$ is the free-fall shell thickness, and $R_{\text{out}}, R_{\text{in}}$ are the trajectories of the outer and inner free-falling surfaces. The density profile described by Eq. (17) accurately reproduces the results of numerical simulations obtained using the code *LILAC*.

During the coasting and deceleration phase, the absence of an applied pressure causes the shell surfaces to expand at the speed of sound, suggesting that the shell thickness increases at the rate

$$\frac{d\Delta_{\text{ff}}}{dt} = \mu \langle C_{s(\text{ff})} \rangle, \quad (18)$$

where $\langle C_{s(\text{ff})} \rangle$ is the average unshocked-shell sound speed and μ is a proportionality constant. Typically the free-fall sound speed is much smaller than the shock velocity through the shell so there is no significant thickening of the shell during the deceleration phase as compared to the coasting phase. Furthermore, the shell sound speed during the free-fall phase is much lower than the implosion velocity. Therefore, changes in the

shell's internal energy do not significantly affect the free-falling shell's kinetic energy. It follows that the change in shell thickness, while significant during the coasting phase, can be neglected during the deceleration phase, and $\Delta_{\text{ff}} = \Delta_0 = \text{constant}$ from the shock–shell interaction time to the stagnation time. The inner and outer free-fall surface trajectories can therefore be approximated with linear functions of time:

$$R_{\text{in}} \approx R_0 - V_{\text{imp}}t, \quad R_{\text{out}} \approx R_0 + \Delta_0 - V_{\text{imp}}t, \quad (19)$$

where R_0 is the position of the inner shell surface at the beginning of the deceleration phase.

Since the free-fall profiles describe the conditions of the unshocked shell material, it is reasonable to assume that the free-fall conditions are isentropic. If, for simplicity, we use an ideal gas equation of state for the shell, the shell pressure evolves according to the simple adiabatic equation

$$P_{\text{ff}}(r, t) = \beta_{\text{ff}} \rho_{\text{ff}}(r, t)^{5/3}, \quad (20)$$

where P_{ff} and β_{ff} are the free-fall pressure and adiabat, respectively. Here, for simplicity, we assume that the free-fall adiabat is uniform and equal to its value (in flight) at the beginning of the deceleration phase $\beta_{\text{ff}} = \beta_{\text{if}}$.

b. Shocked-shell equations of motion. The shock front divides the shell into two parts, which have different dynamics. The shocked shell material encloses the hot spot and produces the true piston action of the shell. The shocked material is usually much denser than the unshocked material. The latter is described by the free-fall conditions mentioned earlier and contributes to the hot-spot compression work through the flow of momentum across the shock front. The contribution of the free-fall shell to the hot-spot compression is dominant during the initial stage of the deceleration phase, when the mass of the shocked shell is small. At later times, however, it is the shocked shell that provides most of the compression work.

As shown in Ref. 8, ablation off the shell's inner surface into the hot spot determines the hot-spot mass. This is typically a small fraction of the shell mass until a burn wave begins to propagate through the shell and the hot spot is filled with ablated material. This raises its density to a level comparable with the shell density. Thus, mass ablation off the shell into the hot spot significantly affects the shell dynamics only after the onset of the ignition process and during burn-wave propaga-

tion in the shell, stages that are not considered in this article. Here, we neglect the effect of mass ablation on the shell's dynamics and approximate the fluid velocity at the shell's inner surface (equal to the hot-spot radius) with the surface velocity:

$$U_{\text{ss}}(R_{\text{hs}}, t) = \dot{R}_{\text{hs}} - V_a \approx \dot{R}_{\text{hs}}, \quad (21)$$

where the subscript “ss” stands for *shocked shell* and “hs” for *hot spot*. Since the shocked material is dense, it is appropriate to approximate the shocked part of the shell as a thin shell. In the thin-shell approximation, the shocked shell's thickness is assumed to be much smaller than its radius. Here, the shocked shell extends from the hot-spot radius R_{hs} to the shock front R_k , and the fluid velocity within the shocked shell can be approximated by its Taylor expansion:

$$U_{\text{ss}}(r, t) \approx \dot{R}_{\text{hs}} + \left[\frac{\partial U}{\partial r} \right]_{R_{\text{hs}}} (r - R_{\text{hs}}). \quad (22)$$

Since the flow is isentropic within the shocked shell, it is straightforward to determine the spatial derivatives from the entropy conservation equation

$$\left[\partial_t (P^{3/5} r^2) + \partial_r (P^{3/5} r^2 U) = 0 \right],$$

leading to

$$\left[\frac{\partial U}{\partial r} \right]_{R_{\text{hs}}} = -\frac{1}{P_{\text{hs}}(t)^{3/5} R_{\text{hs}}(t)^2} \frac{d}{dt} \{ P_{\text{hs}}(t)^{3/5} R_{\text{hs}}(t)^2 \}. \quad (23)$$

Using the hot-spot-energy equation [Eq. (14)] to eliminate \dot{R}_{hs} in Eq. (23) and substituting (23) into (22) leads to the following simple form of the post-shock velocity:

$$U_{\text{ss}}(R_k, t) = \dot{R}_{\text{hs}} \frac{R_k}{R_{\text{hs}}} - \frac{3}{5} \sum_{\alpha} P_{\text{hs}}(R_k - R_{\text{hs}}). \quad (24)$$

Because of the mass flow through the shock front, the mass of the shocked part M_{ss} increases with time. The variation of the shocked shell's mass is determined by the mass flow through the shock front:

$$\dot{M}_{\text{ss}} = 4\pi R_k^2 \rho_{\text{ff}}(R_k, t) [\dot{R}_k + V_{\text{imp}}], \quad (25)$$

where $\rho_{\text{ff}}(R_k, t)$ is the unshocked density given by Eq. (17) calculated at the shock front. Here, the subscript “ff” (free fall) refers to the unshocked material.

The momentum balance of the shocked shell is obtained by integrating the momentum conservation equation from the hot-spot radius to the shock front, yielding

$$\frac{d}{dt} [M_{\text{ss}} \langle U_{\text{ss}} \rangle] + \dot{M}_{\text{ss}} V_{\text{imp}} = 4\pi R_{\text{hs}}^2 P_{\text{hs}}, \quad (26)$$

where $\langle U_{\text{ss}} \rangle \approx 0.5 [U_{\text{ss}}(R_{\text{hs}}, t) + U_{\text{ss}}(R_k, t)]$ is an average velocity of the shocked shell. In the derivation of Eq. (26), the shell’s free-fall pressure has been neglected with respect to the hot-spot pressure, and the velocity is assumed uniform and equal to the implosion velocity throughout the free-fall part of the shell. The average shocked-shell velocity can be rewritten using Eqs. (21) and (24), yielding

$$\langle U_{\text{ss}} \rangle = \dot{R}_{\text{hs}} \frac{R_{\text{hs}} + R_k}{2R_{\text{hs}}} - \frac{3}{5} \sum_{\alpha} P_{\text{hs}} \frac{R_k - R_{\text{hs}}}{2}. \quad (27)$$

The next step is to determine the shock position $R_k(t)$ using the Rankine–Hugoniot relations at the shock front. We assume that the return shock is strong and write the shock velocity as

$$\dot{R}_k = -V_{\text{imp}} + \sqrt{\frac{4P_{\text{ss}}(R_k, t)}{3\rho_{\text{ff}}(R_k, t)}}. \quad (28)$$

The quantity $P_{\text{ss}}(R_k, t)$ represents the pressure in the shocked shell calculated at the shock front. This pressure can be determined using another Hugoniot relation relating the velocities before ($-V_{\text{imp}}$) and after [$U_{\text{ss}}(R_k, t)$] the shock:

$$U_{\text{ss}}(R_k, t) = -V_{\text{imp}} + \sqrt{\frac{3P_{\text{ss}}(R_k, t)}{4\rho_{\text{ff}}(R_k, t)}}. \quad (29)$$

Thus, the post-shock pressure $P_{\text{ss}}(R_k, t)$ can be determined from Eq. (29) and substituted into Eq. (28), leading to the following equation for the shock position:

$$\dot{R}_k = \frac{V_{\text{imp}}}{3} + \frac{4}{3} U_{\text{ss}}(R_k, t), \quad (30)$$

where the post-shock velocity $U_{\text{ss}}(R_k, t)$ is given in Eq. (24). The last equation needed to close the system comes from the hot-spot energy balance [Eq. (14)] (derived earlier) relating the hot-spot pressure $P_{\text{hs}}(t)$ to the hot-spot radius $R_{\text{hs}}(t)$. Equations (14), (17), (24)–(27), and (30) represent a complete set of equations that describe the evolution of all the relevant hydrodynamic quantities during the deceleration phase and the onset of ignition. For convenience, the complete model is summarized in the following subsection.

c. Summary of the thick shell model. We summarize below all the relevant equations of the thick shell model, consisting of a set of four ordinary differential equations governing the evolution of the following hydrodynamic quantities:

1. The hot-spot pressure $P_{\text{hs}}(t)$, which obeys the following ordinary differential equation (ODE):

$$\dot{P}_{\text{hs}} + 5P_{\text{hs}} \frac{\dot{R}_{\text{hs}}}{R_{\text{hs}}} = \sum_{\alpha} P_{\text{hs}}^2. \quad (31)$$

2. The hot-spot radius $R_{\text{hs}}(t)$ equal to the shocked-shell inner-surface radius governed by Newton’s law:

$$M_{\text{ss}} \frac{d}{d\tau} \langle U_{\text{ss}} \rangle + \dot{M}_{\text{ss}} [\langle U_{\text{ss}} \rangle + V_{\text{imp}}] = 4\pi P_{\text{hs}} R_{\text{hs}}^2, \quad (32)$$

where $\langle U_{\text{ss}} \rangle$ is the average shocked-shell velocity,

$$\langle U_{\text{ss}} \rangle = \dot{R}_{\text{hs}} \frac{R_{\text{hs}} + R_k}{2R_{\text{hs}}} - \frac{3}{10} \sum_{\alpha} P_{\text{hs}} (R_k - R_{\text{hs}}), \quad (33)$$

and R_k is the shock position.

3. The shocked-shell mass $M_{\text{ss}}(t)$, which obeys mass conservation:

$$\dot{M}_{\text{ss}} = 4\pi R_k^2 \rho_{\text{ff}}(R_k, t) [\dot{R}_k + V_{\text{imp}}]. \quad (34)$$

4. The shock position within the shell $R_k(t)$ derived from Hugoniot relations:

$$\dot{R}_k = \frac{V_{\text{imp}}}{3} + \frac{4}{3} U_{\text{ss}}(R_k, t), \quad (35)$$

where $U_{ss}(R_k, t)$ is the post-shock velocity,

$$U_{ss}(R_k, t) = \dot{R}_{hs} \frac{R_k}{R_{hs}} - \frac{3}{5} \sum_{\alpha} P_{hs}(R_k - R_{hs}). \quad (36)$$

The unshocked shell material is described by the *free-fall* conditions:

$$\rho_{ff}(r, t) = \frac{3M_{sh}}{\pi r^2} \frac{[r - R_{in}(t)]^2 [R_{out}(t) - r]}{\Delta_0^4}, \quad (37)$$

where M_{sh} is the total shell mass, $\Delta_0 = R_{out}(t) - R_{in}(t)$ is the free-fall shell thickness (approximately constant), and $R_{in}(t) = R_0 - V_{imp}t$ is the inner-surface trajectory starting from the initial radius R_0 at the beginning of the deceleration phase.

A set of initial conditions at the beginning of the deceleration phase corresponding to the shell–shock interaction time must be provided to solve the system of equations:

1. the inner-surface, free-fall (or implosion) velocity $-V_{imp}$,
2. the inner shell radius R_0 ,
3. the shell thickness Δ_0 ,
4. the shell mass M_{sh} , and
5. the hot-spot pressure P_0 .

The solution of the four differential equations yields the time evolution of the shock position, hot-spot radius, and pressure. The last two quantities can be used to determine the evolution of all other relevant hydrodynamic quantities inside the hot spot, such as temperature, density, ablation velocity, density-gradient scale length, and areal density as described in Ref. 8.

Ignition Scaling Using the Thin Incompressible Shell Model

In this section, we first determine the ignition criterion in terms of the initial conditions at the beginning of the deceleration phase for the thin incompressible shell model. The ignition criterion has a very simple form and simple physical interpretation. Next, we derive a scaling law in terms of the shell’s kinetic energy and an entropy function. The latter does not represent the shell adiabat since the shell is assumed incompressible. It will be shown in the section entitled **Ignition Scaling Using the Compressible Shell Model**, however, that this entropy function is directly proportional to the shell

adiabat at stagnation when the finite compressibility of the shell is included.

1. Ignition Criterion

The thin shell model can be simplified by eliminating P_{hs} between Eqs. (15) and (16) and by using the following dimensionless variables:

$$\hat{R}_{hs} \equiv R_{hs}/R_0, \quad \tau = V_{imp}t/R_0. \quad (38)$$

A straightforward manipulation of Eqs. (15) and (16) leads to the following single ordinary differential equation for the hot-spot radius:

$$\frac{d}{d\tau} \left(\hat{R}_{hs}^3 \frac{d^2 \hat{R}_{hs}}{d\tau^2} \right) = \frac{\Upsilon_{\alpha}}{\hat{\epsilon}_0} \hat{R}_{hs} \left(\frac{d^2 \hat{R}_{hs}}{d\tau^2} \right)^2, \quad (39)$$

where

$$\Upsilon_{\alpha} \equiv \frac{\sum_{\alpha} P_0 R_0}{V_{imp}} \hat{\epsilon}_0^2 = \frac{\tau_i^0}{\tau_{\alpha}^0} \hat{\epsilon}_0^{3/2}, \quad \hat{\epsilon}_0 = \frac{M_{sh} V_{imp}^2}{4\pi P_0 R_0^3}, \quad (40)$$

$$\tau_i^0 = \left[\frac{M_{sh}}{4\pi P_0 R_0} \right]^{1/2}, \quad \tau_{\alpha}^0 = \frac{1}{\sum_{\alpha} P_0}. \quad (41)$$

Here $\hat{\epsilon}_0$ represents the ratio between the initial shell kinetic energy and the initial hot-spot internal energy, which is much greater than unity in typical ICF implosions. (Small values of $\hat{\epsilon}_0$ require that the hot-spot radius at the beginning of the free-fall phase be very close to the stagnation hot-spot radius. This does not occur in typical ICF implosions.) The times τ_i^0 and τ_{α}^0 represent the inertial time of the shell and the alpha-particle heating time at the beginning of the deceleration phase. The shell trajectory is determined by solving Eq. (39) with the following initial conditions:

$$\hat{R}_{hs}(0) = 1, \quad \dot{\hat{R}}_{hs}(0) = -1, \quad \ddot{\hat{R}}_{hs}(0) = 1/\hat{\epsilon}_0, \quad (42)$$

where the “dot” indicates a derivative with respect to τ .

It is important to notice that as long as the alpha heating is smaller than the compression work, the right-hand side of Eq. (39) can be neglected and the shell trajectory is given by

$$\hat{R} = \sqrt{1 - 2\tau + \tau^2(1 + \hat{\epsilon}_0^{-1})}, \quad (43)$$

leading to the following values of the stagnation time, radius, acceleration, and pressure:

$$t_{\text{stag}} = \frac{R_0}{V_{\text{imp}}} \frac{\hat{\epsilon}_0}{1 + \hat{\epsilon}_0}, \quad R_{\text{stag}} = \frac{R_0}{\sqrt{1 + \hat{\epsilon}_0}}, \quad (44a)$$

$$g_{\text{stag}} = (1 + \hat{\epsilon}_0)^{3/2} \frac{R_0}{(\tau_i^0)^2}, \quad P_{\text{stag}} = P_0 (1 + \hat{\epsilon}_0)^{5/2}. \quad (44b)$$

Equations (44) yield scaling relations for the stagnation values of the hydrodynamic quantities in terms of the shell and hot-spot properties at the beginning of the deceleration phase. Such relations are valid as long as the hot spot is not ignited. If the alpha heating becomes important, the right-hand side of Eq. (39) must be retained and the stagnation pressure and deceleration are significantly larger.

It is easy to show that, for a given $\hat{\epsilon}_0$, the solution of Eq. (39) develops an explosive instability when the parameter Υ_α exceeds a critical value. Both parameters $\hat{\epsilon}_0$ and Υ_α are functions of the shell and hot-spot properties at the beginning of the deceleration phase (M_{sh} , V_{imp} , R_0 , and P_0). A typical singular explosive solution (dashed line in Fig. 87.47) shows the shell ejected outward at an infinite velocity. Such solutions correspond to the thermal instability of the hot spot, which we denote as “ignition.” The singularity is due to the fact that the fusion reaction rate $\langle \sigma v \rangle$ is taken to be proportional to T^2 , and, therefore, it diverges to infinity with temperature. In reality, $\langle \sigma v \rangle$ is bounded at high temperatures and the shell ejection velocity is finite. Nevertheless, the occurrence of the singularity in the solution of Eq. (39) represents a simple and robust definition of ignition for the thin shell model. We therefore conclude that the hot spot is ignited when the solution of Eq. (39) is singular. The numerical solution of Eq. (39) indicates that singular solutions develop when the following approximate condition is satisfied:

$$\Upsilon_\alpha \left[1 + \left(\frac{3}{5} \right)^{1/3} \hat{\epsilon}_0^{-1} \right]^{3/2} > \sqrt{3}, \quad (45a)$$

which reduces to

$$\Upsilon_\alpha > \sqrt{3} \quad (45b)$$

in the limit $\hat{\epsilon}_0 \gg 1$. Equations (45) represent the ignition conditions in terms of the shell and hot-spot properties at the beginning of the deceleration phase. The physical interpretation of the ignition threshold is straightforward. We rewrite the hot-spot-energy equation [Eq. (14)] in the following intuitive form:

$$\frac{1}{E_{\text{hs}}} \frac{dE_{\text{hs}}}{dt} = \sum_\alpha P_{\text{hs}} - 2 \frac{\dot{R}_{\text{hs}}}{R_{\text{hs}}}, \quad (46)$$

where $E_{\text{hs}} = (4\pi/3)P_{\text{hs}}R_{\text{hs}}^3$ is the hot-spot energy. After stagnation, the second term on the right-hand side is negative ($\dot{R}_{\text{hs}} > 0$ after stagnation) and represents the inverse hot-spot decompression time ($\tau_{\text{decomp}} = R_{\text{hs}}/2\dot{R}_{\text{hs}}$) due to the outward motion of the shell pushed by the hot-spot pressure. This decompression time can be estimated by setting

$$\tau_{\text{decomp}} \sim 0.5 \sqrt{R_{\text{hs}}/\ddot{R}_{\text{hs}}}$$

and using Eq. (15), leading to

$$\tau_{\text{decomp}} = \frac{1}{2} \sqrt{\frac{M_{\text{sh}}}{4\pi P_{\text{hs}} R_{\text{hs}}}}. \quad (47)$$

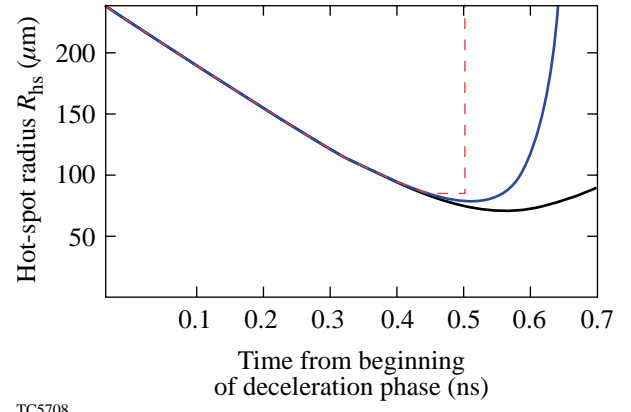


Figure 87.47

Thin incompressible shell model prediction for the evolution of the hot-spot radius for NIF-like capsules [obtained by solving Eq. (39)]. The dashed line represents an ignited solution with a singularity after stagnation. The solid lines represent two non-ignited solutions.

Note that the first term on the right-hand side of Eq. (46) represents the inverse alpha-particle heating time

$$\tau_\alpha = 1/\sum_\alpha P_{\text{hs}}.$$

Ignition occurs right after stagnation if the alpha heating time is shorter than the decompression time:

$$\tau_\alpha(\text{stag}) < \tau_{\text{decomp}}(\text{stag}). \quad (48)$$

If Eq. (48) is satisfied, a thermal instability (the ignition process) is triggered because the hot-spot pressure starts to increase and leads to a shorter alpha heating time $\tau_\alpha \sim 1/P_{\text{hs}}$. The decompression time is proportional to $1/\sqrt{P_{\text{hs}}}$ and decreases less than the alpha heating time. This leads to a further increase in pressure and a thermal explosive instability. To estimate the ignition threshold, we use the stagnation values (without alpha particles) given in Eqs. (44) to find $\tau_\alpha(\text{stag})$:

$$\tau_\alpha(\text{stag}) \approx \frac{1}{\sum_\alpha P_0 (1 + \hat{\epsilon}_0)^{5/2}} = \frac{\tau_\alpha^0}{(1 + \hat{\epsilon}_0)^{5/2}}. \quad (49)$$

Similarly, we find $\tau_{\text{decomp}}(\text{stag})$:

$$\tau_{\text{decomp}}(\text{stag}) \approx \frac{1}{2} \left(\frac{R_{\text{stag}}}{g_{\text{stag}}} \right)^{1/2} = \frac{\tau_i^0}{2(1 + \hat{\epsilon}_0)}, \quad (50)$$

where τ_i^0 [defined in Eq. (41)] represents the decompression time if the shell stagnates at time $t=0$ [$\tau_{\text{decomp}}(0) = \tau_i^0$]. Substituting Eqs. (49) and (50) into (48) yields the approximate ignition condition

$$\frac{\tau_{\text{decomp}}(0)}{\tau_\alpha(0)} (1 + \hat{\epsilon}_0)^{3/2} = Y_\alpha (1 + \hat{\epsilon}_0^{-1})^{3/2} > 2, \quad (51)$$

where the identity $\tau_\alpha^0 \equiv \tau_\alpha(0)$ has been used and the term $(1 + \hat{\epsilon}_0)^{3/2}$ represents the amplification factor of the ratio τ_i/τ_α due to the hot-spot compression by the shell. Observe that condition (51) is similar to the numerical fit given in (45a) and yields approximately the same ignition threshold ($Y_\alpha > 2$) in the limit of $\hat{\epsilon}_0 \gg 1$.

2. Ignition Scaling

We consider the marginal ignition criterion given in Eq. (45b) in the relevant ICF limit $\hat{\epsilon}_0 \gg 1$ and rewrite Y_α [defined in Eq. (40)] in the following form:

$$Y_\alpha = \frac{\sum_\alpha}{(2\pi)^2} \frac{E_k^2}{P_0 R_0^5 V_{\text{imp}}}, \quad (52)$$

where $E_k = M_{\text{sh}} V_{\text{imp}}^2 / 2$ is the shell's kinetic energy. Using the thin-shell approximation, the shell mass can be written as

$$M_{\text{sh}} \approx 4\pi \rho_{\text{sh}}(0) R_0^3 / A_0, \quad (53)$$

where $\rho_{\text{sh}}(0)$ and $A_0 = R_0/\Delta_0$ are the shell density and aspect ratio at the beginning of the deceleration phase (here Δ_0 is the shell thickness). Equation (53) can also be cast in terms of shell kinetic energy by multiplying both sides by V_{imp}^2 and then using it to derive the initial hot-spot radius R_0 :

$$R_0 = \left(\frac{A_0 E_k}{2\pi \rho_{\text{sh}}(0) V_{\text{imp}}^2} \right)^{1/3}. \quad (54)$$

Substituting Eq. (54) into Eq. (52) and rewriting the ignition condition $Y_\alpha = \text{constant}$ in terms of the kinetic energy yields

$$E_k \approx \frac{2\pi Y_\alpha^3}{\sum_\alpha^3} \frac{\beta_0^3}{V_{\text{imp}}^7}, \quad (55)$$

where $Y_\alpha \approx \sqrt{3}$ for ignition and

$$\beta_0 \equiv \frac{P_0}{[\rho_{\text{sh}}(0)/A_0]^{5/3}} \quad (56)$$

has the dimensions of an adiabat. Note that the pressure P_0 is the hot-spot pressure at time $t=0$ and not the shell pressure. Thus, at this stage, the parameter β_0 cannot be related to the shell adiabat as should be expected when approximating the shell with an incompressible layer. The scaling (56), though dimensionally similar to the HTL stagnation scaling [Eq. (5)], is still inconclusive and deserves further analysis as shown in the next section, where the effects of finite shell compressibility are retained.

Ignition Scaling Using the Compressible Shell Model

Since the right-hand side of Eq. (55) represents the minimum kinetic energy required for ignition, it is appropriate to determine A_0 in order to minimize the ignition requirements. The optimum A_0 can be determined by making use of the thick shell model described earlier [Eqs. (31)–(37)] and the following simple argument.

If the shell is too thin, the return shock reaches the outer shell surface before stagnation, causing the shell to rapidly expand outward, decompressing the hot spot and stopping the ignition process. If the shell is too thick, stagnation (and therefore ignition) is reached when the shock is still within the shell and the unshocked part of the shell is still free falling. In this scenario, ignition is triggered with a surplus of kinetic energy in the free-fall part of the shell. Ignition using the minimum kinetic energy occurs when the return shock is exactly at the shell's outer surface at the same time the shell reaches the stagnation point. We conclude that the optimum shell thickness is such that the shock reaches the outer shell surface at stagnation.

Because the shock position is the new information needed to optimize A_0 and minimize the shell's kinetic energy, the ignition condition needs to be determined using the compressible thick shell model. The next step is to rewrite the thick shell model in dimensionless form using the following definitions:

$$\hat{R}_{\text{hs}} = R_{\text{hs}}/R_0, \quad \hat{R}_k = R_k/R_0, \quad \hat{P}_{\text{hs}} = P_{\text{hs}}/P_0, \quad (57\text{a})$$

$$\tau = V_{\text{imp}}t/R_0, \quad \hat{M} = M_{\text{ss}}/M_{\text{sh}}, \quad (57\text{b})$$

where R_0 and P_0 are the shell's inner surface and hot-spot pressure at the beginning of the deceleration phase. A simple manipulation of Eqs. (31)–(37) using the definitions in (57) yields a closed set of four differential equations,

$$\begin{aligned} \frac{d}{d\tau} \left\{ \hat{M} \left[\hat{R}_{\text{hs}} \frac{\dot{\hat{R}}_{\text{hs}} + \dot{\hat{R}}_k}{2\hat{R}_{\text{hs}}} - \frac{3}{10} \frac{\Upsilon_\alpha}{\hat{\varepsilon}_0^2} \hat{P}_{\text{hs}} (\hat{R}_k - \hat{R}_{\text{hs}}) + 1 \right] \right\} \\ = \frac{\hat{P}_{\text{hs}} \hat{R}_{\text{hs}}^2}{\hat{\varepsilon}_0}, \end{aligned} \quad (58)$$

$$\dot{\hat{R}}_k = \frac{1}{3} + \frac{4}{3} \dot{\hat{R}}_{\text{hs}} \frac{\hat{R}_k}{\hat{R}_{\text{hs}}} - \frac{4}{5} \frac{\Upsilon_\alpha}{\hat{\varepsilon}_0^2} \hat{P}_{\text{hs}} (\hat{R}_k - \hat{R}_{\text{hs}}), \quad (59)$$

$$\dot{\hat{M}} = 12A_0^4 (\hat{R}_k + \tau - 1)^2 |1 + A_0^{-1} - \tau - \hat{R}_k|$$

$$\times (\dot{\hat{R}}_k + 1) H(1 - \hat{M}), \quad (60)$$

$$\dot{\hat{P}}_{\text{hs}} + 5 \hat{P}_{\text{hs}} \frac{\dot{\hat{R}}_{\text{hs}}}{\hat{R}_{\text{hs}}} = \frac{\Upsilon_\alpha}{\hat{\varepsilon}_0^2} \hat{P}_{\text{hs}}^2, \quad (61)$$

representing the evolution of the shocked shell's inner radius \hat{R}_{hs} , shock position \hat{R}_k , shocked shell mass \hat{M} , and hot-spot pressure \hat{P}_{hs} . The step function $H(1 - \hat{M})$ in Eq. (60) limits the magnitude of the shocked shell mass to the total shell mass. That is, when $M_{\text{ss}} = M_{\text{sh}}$ (i.e., $\hat{M} = 1$), the right-hand side of Eq. (60) vanishes and the shocked shell mass remains constant and equal to the total shell mass. Equations (58)–(61) can be solved using the following set of initial conditions:

$$\begin{aligned} \hat{R}_{\text{hs}}(0) &= 1, \quad \dot{\hat{R}}_{\text{hs}}(0) = 0, \quad \hat{R}_k(0) = 1, \\ \hat{M}(0) &= 0, \quad \hat{P}_{\text{hs}}(0) = 1. \end{aligned} \quad (62)$$

The initial condition $\dot{\hat{R}}_{\text{hs}} = 0$ needs a clarification. Before the interaction with the return shock, the shell density vanishes on the inner surface. As a result of the interaction with the shock, the shell's inner surface is stopped, so the condition $\dot{\hat{R}}_{\text{hs}} = 0$ is applicable right after the interaction with the shock. After this brief stop, the inner shell surface is set in motion by the imploding high-density shell material that is not stopped by the return shock.

Observe that Eqs. (58)–(61) depend on three dimensionless parameters Υ_α , $\hat{\varepsilon}_0$, and A_0 , which need to be determined to satisfy the following two conditions: (1) the hot spot must be ignited, and (2) the return shock must be on the outer surface at stagnation to assure that the kinetic energy is minimized. The first condition requires that the solution of Eqs. (58)–(61) be singular and the shell be ejected outward at infinite velocity after stagnation. The second requires that $\hat{M} = 1$ at stagnation, implying that the entire shell has been shocked.

We solve Eqs. (58)–(61) with the software program MATHEMATICA in the limit of $\hat{\varepsilon}_0 \gg 1$, which is the correct limit for ICF implosions since the shell's kinetic energy is much larger than the hot-spot internal energy at the beginning of the deceleration phase. We find that the singular solutions with $\hat{M} = 1$ at stagnation occur when

$$A_0 = 0.39\sqrt{\hat{\varepsilon}_0}, \quad \Upsilon_\alpha \approx 2.60. \quad (63)$$

Other results from the solution of Eqs. (58)–(61) are shown in Figs. 87.48–87.50. Figures 87.48 and 87.49 plot the evolution of the shocked shell mass and hot-spot pressure. Figure 87.50 shows the trajectories of the hot-spot radius and the shock front near stagnation. Analysis of the solution to the thick shell equations suggests that the stagnation scaling of the hot-spot pressure, hot-spot radius, and shock position are given by the following:

$$P_{hs}(\text{stag}) \approx 1.02 P_0 \hat{\varepsilon}_0^{5/2}, \quad (64a)$$

$$R_{hs}(\text{stag}) \approx 1.23 R_0 / \sqrt{\hat{\varepsilon}_0}, \quad (64b)$$

$$R_k(\text{stag}) \approx 1.40 R_0 / \sqrt{\hat{\varepsilon}_0}. \quad (64c)$$

Observe that the relations for the stagnation values of P_{hs} and R_{hs} are similar (except for a numerical factor) to the ones obtained earlier [Eqs. (44)] with the thin shell model and

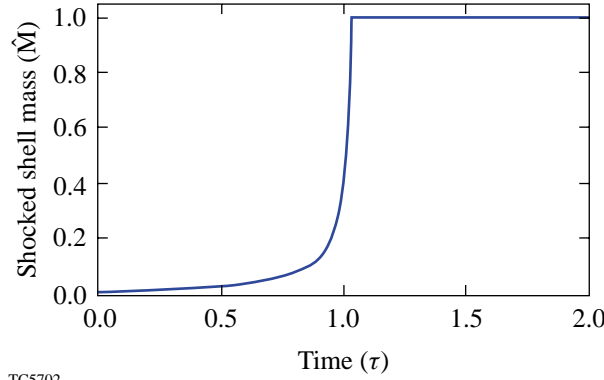


Figure 87.48

Thick compressible shell model results. Plot of the shocked shell mass versus time. Time $t = 0$ corresponds with the beginning of the deceleration phase. When $\hat{M} = 1$, the entire shell has been shocked.

$\hat{\varepsilon}_0 \gg 1$. The ignition condition for Υ_α in Eq. (63) is also similar to (but with a different numerical value) that derived with the thin shell model and leads to the same scaling for the minimum energy required for ignition:

$$E_k \approx \frac{2\pi\Upsilon_\alpha^3}{\Sigma_\alpha^3} \frac{\beta_0^3}{V_{imp}^7}, \quad (65)$$

where β_0 is defined in Eq. (56). The new result here is that the shell's aspect ratio A_0 at the beginning of the deceleration phase is related to the other shell properties through the first condition in Eq. (63). Furthermore, the position of the outer

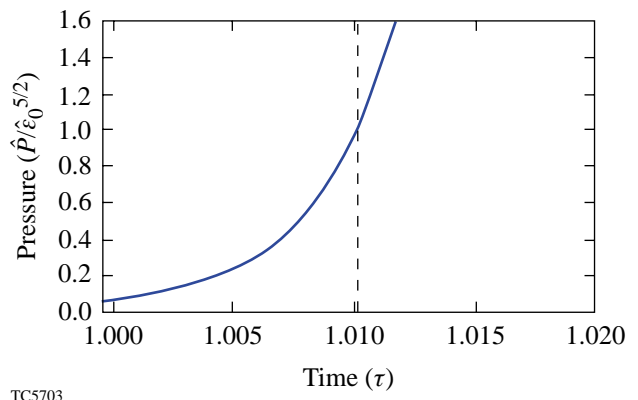


Figure 87.49

Thick compressible shell model results. Evolution of the hot-spot pressure, obtained from Eqs. (58)–(61). The vertical dashed line represents the shock breakout time (also stagnation time).

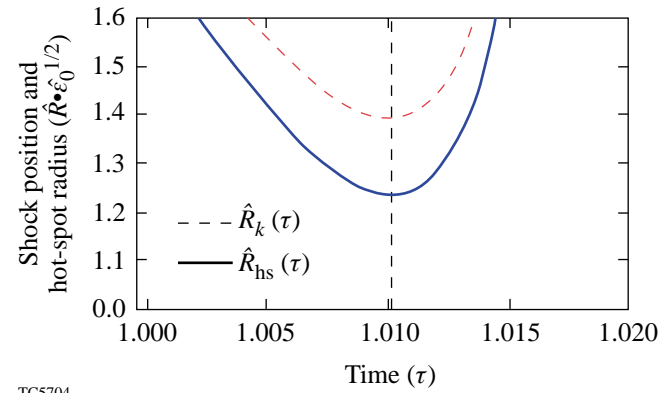


Figure 87.50

Thick compressible shell model results. Trajectories of the shock and the hot-spot radius, obtained from Eqs. (58)–(61). The vertical dashed line represents the shock breakout time (also stagnation time).

shell surface coincides with the shock position R_k and is determined in Eq. (64c). This latest result is essential to determine the ignition scaling in terms of the stagnation properties.

Setting the shell mass at the beginning of the deceleration phase equal to the stagnation mass,

$$4\pi \frac{R_0^3}{A_0} \rho_{sh}(0) \approx \frac{4\pi}{3} [R_k(stag)^3 - R_{hs}(stag)^3] \rho_{sh}(stag), \quad (66)$$

and substituting Eqs. (64) into Eq. (66) leads to the following relation between the shell densities:

$$\rho_{sh}(0) = 0.3 \rho_{sh}(stag) \frac{A_0}{\hat{\epsilon}_0^{3/2}}. \quad (67)$$

Then, using the definition of $\beta_0 \equiv A_0^{5/3} P_0 / \rho_{sh}(0)^{5/3}$ and Eqs. (64a) and (67), the following relation is easily derived:

$$\beta_0 = 7.52 \beta_s, \quad (68)$$

where $\beta_s \equiv P_{hs}(stag)/\rho_{sh}(stag)^{5/3}$ represents the shell stagnation adiabat. Observe that the hot-spot pressure is used in the definition of the shell stagnation adiabat. While this is not an exact definition, it is sufficiently accurate because the stagnation pressure is continuous at the hot spot/shell interface.

The next step is to finalize the scaling law Eq. (65) using Eqs. (63) and (68) and the standard definition of the normalized stagnation adiabat

$$\alpha_s \equiv \frac{P(\text{Mbar})}{2.18 \rho_{sh}(\text{g/cm}^3)^{5/3}}. \quad (69)$$

A straightforward manipulation of Eq. (65) leads to the following formula for the minimum energy required for ignition:

$$E_k \approx 2.7(\text{kJ}) \alpha_s^3 \left[\frac{3 \times 10^7}{V_{imp}(\text{cm/s})} \right]^7. \quad (70)$$

Equation (70) represents the marginal ignition scaling in terms of the stagnation adiabat. Observe that Eq. (70) is quite similar

in both the scaling relation as well as the numerical coefficient with the result of Ref. 5, which reads as

$$E_k \approx 2.1(\text{kJ}) \alpha_s^{2.66} \left[\frac{3 \times 10^7}{V_{imp}(\text{cm/s})} \right]^{7.2}.$$

The next step is to relate the stagnation to the in-flight adiabat and determine the “in-flight” scaling for marginal ignition.

Ignition Scaling Using the In-Flight Adiabat

Comparisons of different ignition capsules are usually based on the magnitude of the in-flight adiabat, which can be easily controlled by tuning the initial foot of the laser pulse. In this section, the stagnation adiabat is related to the in-flight adiabat, and the ignition scaling law is expressed in terms of the in-flight hydrodynamic properties of the shell.

Starting from Eq. (63) ($A_0 = 0.39\sqrt{\hat{\epsilon}_0}$) and the definition of $\hat{\epsilon}_0$ [Eq. (40)], we express the hot-spot pressure at the beginning of the deceleration phase $P_{hs}(0)$ in terms of the shell pressure at the same time $P_{sh}(0)$:

$$P_{hs}(0) = 0.25 P_{sh}(0) M_A(0)^2 / A_0^3, \quad (71)$$

where $M_A(0) = V_{imp}/C_s(0)$ is the shell’s Mach number at the beginning of the deceleration phase and $C_s(0)$ is the shell’s sound speed. Substituting Eq. (71) into Eq. (68) yields the following relation:

$$\beta_s \approx 0.034 \beta_{if} M_A(0)^2 / A_0^{4/3}, \quad (72)$$

where $\beta_{if} \equiv P_{sh}(0)/\rho_{sh}(0)^{5/3}$ is the shell’s in-flight adiabat. It is important to emphasize that time zero represents the beginning of the deceleration phase, which starts after the coasting phase.

The next step is to relate the shell’s Mach number and aspect ratio at the beginning of the deceleration phase to their values at the beginning of the coasting phase during which the laser is off and the ablation pressure vanishes. During the coasting phase, the shell travels at approximately constant velocity, while rarefaction waves propagate inside the shell from both the inner and outer surfaces since the shell pressure is much larger than the surrounding pressure. The expansion velocity induced by a rarefaction wave is

$$v_{\text{exp}} = 3C_s \left[1 - (\rho/\rho_{\max})^{1/3} \right]$$

and depends on the location along the density profile. If we characterize the shell as the region enclosed by the two points where the density is equal to $1/e$ times the maximum density, then the expansion velocity of the inner and outer surfaces is $v_{\text{exp}} \approx 0.85 C_s$. Using these definitions, the shell thickness Δ_{sh} increases with time during the coasting phase, according to the following equation:

$$\frac{d\Delta_{\text{sh}}}{dt} \approx 1.7 C_s^c, \quad (73)$$

where C_s^c is the shell sound speed during the coasting phase. Equation (73) can be further simplified by using the following dimensionless variables:

$$\hat{\Delta}_{\text{sh}} = \Delta_{\text{sh}}/\Delta_c, \quad \hat{R}_{\text{sh}} = R_{\text{sh}}/R_c,$$

where R_{sh} is the shell radius and R_c, Δ_c are the shell radius and thickness at the beginning of the coasting phase. Assuming that the shell adiabat is constant during the coasting phase and using the thin-shell approximation $[M_{\text{sh}} \approx 4\pi\rho_{\text{sh}} R_{\text{sh}}^2 \Delta_{\text{sh}}]$, Eq. (73) can be rewritten as

$$\frac{d\hat{\Delta}_{\text{sh}}}{d\hat{R}_{\text{sh}}} = -1.7 \frac{A_c}{M_A^c} \frac{1}{\hat{R}_{\text{sh}}^{2/3} \hat{\Delta}_{\text{sh}}^{1/3}}, \quad (74)$$

where A_c and M_A^c are the shell's aspect ratio and Mach number at the beginning of the coasting phase. Equation (74) can be easily integrated to determine the evolution of the shell thickness during the coasting phase:

$$\Delta_{\text{sh}} = \Delta_c \left\{ 1 + 6.8 \frac{A_c}{M_A^c} \left[1 - \left(\frac{R_{\text{sh}}}{R_c} \right)^{1/3} \right] \right\}^{3/4}. \quad (75)$$

Assuming that the shell radius at the beginning of the deceleration phase is much smaller than the radius at the beginning of the coasting phase [$R_{\text{sh}}(0) \ll R_c$], Eq. (75) yields the asymptotic value of the shell thickness at the beginning of the deceleration phase (i.e., time $t = 0$):

$$\Delta_{\text{sh}}(0) \approx \Delta_c \left(1 + 6.8 \frac{A_c}{M_A^c} \right)^{3/4}. \quad (76)$$

A relation between the aspect ratio A_c and Mach number M_A^c can be determined by matching the shell expansion rate at the beginning of the coasting phase with the one calculated at the end of the acceleration phase as explained below.

During the acceleration phase, the shell density can be obtained from the momentum conservation equation

$$\rho_{\text{sh}} g = \frac{\partial P}{\partial r}, \quad (77)$$

where $P = \beta_{\text{if}} \rho_{\text{sh}}^{5/3}$. A simple manipulation of Eq. (77) yields the density profile

$$\rho_{\text{sh}} = \rho_a \left(1 - \frac{R_a - r}{2\Delta_{\text{sh}}} \right)^{3/2}, \quad (78)$$

where R_a is the radius of the ablation surface, ρ_a is the density at the ablation surface, and

$$\Delta_{\text{sh}} = \frac{3C_s^2}{4g} \quad (79)$$

is the shell thickness from the ablation surface to the $1/e$ point. The shell's aspect ratio peaks at the beginning of the main pulse when its value is proportional to the square of the Mach number. It then decays during the main pulse and the following coasting phase when the shell radius decreases and the thickness increases. The thickness can be written in terms of the shell radius by using Eq. (79) and assuming that the ablation pressure P_a increases like $1/R$ as indicated by the result of several numerical simulations. Setting $g = 4\pi R^2 P_a / M_{\text{sh}}$ into Eq. (79) yields the shell thickness as a function of the radius:

$$\Delta_{\text{sh}} = \frac{5}{16\pi} \frac{\beta_{\text{if}}^{3/5} M_{\text{sh}}}{(P_a R_{\text{sh}})^{3/5}} \frac{1}{R_{\text{sh}}^{7/5}} \sim \frac{1}{R_{\text{sh}}^{7/5}}. \quad (80)$$

In deriving Eq. (80), the reduction of the shell mass due to the laser ablation has been neglected. This approximation may not be appropriate for indirect-drive capsules where a large portion of the shell material is ablated off during the implosion. The rate of the shell expansion during the acceleration phase follows from Eq. (80):

$$\dot{\Delta}_{\text{sh}} = -\frac{7}{5} \frac{\Delta_{\text{sh}}}{R_{\text{sh}}} \dot{R}_{\text{sh}}. \quad (81)$$

When the expansion velocity [Eq. (81)] reaches the sound speed, the shell pressure exceeds the applied ablation pressure. Typically, the laser is turned off at this point since the shell pressure is so large that the applied ablation pressure has little effect on the shell dynamics. From a mathematical standpoint, the acceleration phase turns into the coasting phase when the shell's expansion velocity calculated during acceleration phase [Eq. (81)] matches the expansion velocity calculated during the coasting phase [Eq. (73)]. The matching occurs when

$$\frac{7}{5} \frac{\Delta_{\text{sh}}}{R_{\text{sh}}} = 1.7 \frac{C_s^c}{-\dot{R}_{\text{sh}}}, \quad (82)$$

which leads to the following expression for the aspect ratio at the beginning of the coasting phase:

$$A_c = 0.82 M_A^c. \quad (83)$$

The next step is to rewrite the shell's Mach number at the beginning of the deceleration phase in terms of the hydrodynamic quantities at the beginning of the coasting phase. Using the thin-shell approximation, one finds

$$M_A(0) = M_A^c \left(\frac{R_0}{R_c} \right)^{2/3} \left(\frac{\Delta_0}{\Delta_c} \right)^{1/3}, \quad (84)$$

where $R_0 = R_{\text{sh}}(0)$ and $\Delta_0 = \Delta_{\text{sh}}(0)$. Substituting Eqs. (83), (84), and (76) into (72) leads to the following expression of the stagnation adiabat:

$$\beta_s = 0.74 \beta_{\text{if}} \left(M_A^c \right)^{2/3}, \quad (85)$$

which can be expressed in the convenient form

$$\alpha_s = 2.8 \alpha_{\text{if}}^{0.8} \left[\frac{V_{\text{imp}}(\text{cm/s})}{3 \times 10^7} \right]^{0.67} \left[\frac{100}{P(\text{Mbar})} \right]^{0.13}. \quad (86)$$

This relation is similar to the numerical fit of Herrmann *et al.*⁵ and to the self-similar scaling found by Kemp *et al.*⁶

$$\alpha_s^{\text{HTL}} = 3.2 \alpha_{\text{if}}^{0.75} \left[\frac{V_{\text{imp}}(\text{cm/s})}{3 \times 10^7} \right]^{0.44} \left[\frac{100}{P(\text{Mbar})} \right]^{0.21}, \quad (87)$$

$$\alpha_s^{\text{KMA}} = 2.3 \alpha_{\text{if}}^{0.85} \left[\frac{V_{\text{imp}}(\text{cm/s})}{3 \times 10^7} \right]^{0.5} \left[\frac{100}{P(\text{Mbar})} \right]^{0.1}. \quad (88)$$

The final ignition energy scaling can be found by substituting Eq. (86) into Eq. (70), yielding

$$E_k = 59(\text{kJ}) \alpha_{\text{if}}^{2.4} \left[\frac{3 \times 10^7}{V_{\text{imp}}(\text{cm/s})} \right]^5 \left[\frac{100}{P(\text{Mbar})} \right]^{0.39}, \quad (89)$$

which is similar to Herrmann's numerical fit

$$E_k^{\text{HTL}} = 50.8(\text{kJ}) \alpha_{\text{if}}^{1.88} \left[\frac{3 \times 10^7}{V_{\text{imp}}(\text{cm/s})} \right]^{5.89} \left[\frac{100}{P(\text{Mbar})} \right]^{0.77}. \quad (90)$$

Observe that both Eq. (88) and (89) show a scaling relation resembling the one derived by Kemp *et al.* as long as the triple product $\rho_{\text{hs}} T_{\text{hs}} R_{\text{hs}}$ is a constant for marginal ignition. However, as shown in the following section, the model described in this article yields a triple product that is proportional to the implosion velocity. This is in agreement with Basko's analysis.

Assumptions About Hot-Spot Hydrodynamics

It is important to remember that Eq. (89) has been derived under three assumptions. The first relates the alpha-particle mean free path, which is assumed to be smaller than the hot-spot radius, implying that the alpha-particle energy is deposited locally. The second, that the behavior of the averaged fusion cross section is given by $\langle \sigma v \rangle \sim T^2$, is valid as long as

the volume average temperature \bar{T}_{hs} is above 6 keV. The third comes from neglecting the radiation losses with respect to the alpha heating. To verify these assumptions, we use the hot-spot solution derived in Ref. 8, where all the hot-spot hydrodynamic quantities are obtained as functions of the hot-spot radius and pressure.

We start with the first of Eq. (24) of Ref. 8, calculated at the hot-spot center $\xi = 0$. Observe that Eq. (24) is an integral equation because the hot-spot mass M_{hs} is a time integral. Equation (24) can be easily converted into a simple differential equation for the central hot-spot density ρ_{hs}^0 :

$$\dot{\rho}_{\text{hs}}^0 + 3\rho_{\text{hs}}^0 \frac{\dot{R}_{\text{hs}}}{R_{\text{hs}}} = 0.072 m_i^{7/2} \kappa_0 \frac{P_{\text{hs}}^{5/2}}{\left(\rho_{\text{hs}}^0\right)^{5/2} R_{\text{hs}}^2}, \quad (91)$$

where $\kappa_0 T^{5/2}$ represents Spitzer thermal conductivity. Equation (91) can be rewritten in a convenient dimensionless form by defining the following variables:

$$\hat{\rho} = \rho_{\text{hs}}^0 / \rho_*, \quad \hat{P} = P_{\text{hs}} / P_0, \quad (92)$$

$$\tau = t V_{\text{imp}} / R_0, \quad \hat{R}_{\text{hs}} = R_{\text{hs}} / R_0, \quad (93)$$

where P_0 , R_0 are the hot-spot pressure and radius at the beginning of the deceleration phase, and

$$\rho_* = 0.47 m_i \left(\kappa_0 \frac{P_0^{5/2} \hat{\epsilon}_0^{27/4}}{R_0 V_{\text{imp}}} \right)^{2/7}, \quad (94)$$

where $\hat{\epsilon}_0$ is defined in Eq. (40). The dimensionless form of the density evolution equation becomes

$$\frac{d\hat{\rho}}{d\tau} + \frac{3\hat{\rho}}{\hat{R}_{\text{hs}}} \frac{d\hat{R}_{\text{hs}}}{d\tau} = \left(\frac{\hat{P}}{\hat{\rho}} \right)^{5/2} \frac{1}{\hat{R}_{\text{hs}}^2} \frac{1}{\hat{\epsilon}_0^{27/4}}, \quad (95)$$

which can be numerically solved once the hot-spot radius and pressure have been determined by solving the set of Eqs. (58)–(61). The central hot-spot temperature follows from Eq. (24) of Ref. 8. A straightforward manipulation yields

$$T_{\text{hs}}(0, t) = 8.3 \text{ (keV)} \left(\frac{\Upsilon_\alpha}{2.6} \right)^{2/7} \left(\frac{V_{\text{imp}} \text{ (cm/s)}}{3 \times 10^7} \right)^{4/7} \frac{\hat{P}}{\hat{\rho} \hat{\epsilon}_0^{5/2}}, \quad (96)$$

where Υ_α is defined in Eq. (40). The hot-spot areal density can also be determined by using Eqs. (23) of Ref. 8 and the definition of $\hat{\rho}$, leading to the following expression:

$$\rho R = 0.18 \text{ (g/cm}^2\text{)} \left(\frac{\Upsilon_\alpha}{2.6} \right)^{5/7} \left[\frac{V_{\text{imp}} \text{ (cm/s)}}{3 \times 10^7} \right]^{3/7} \hat{\rho} \hat{R}_{\text{hs}} \sqrt{\hat{\epsilon}_0}. \quad (97)$$

To determine the stagnation value of the areal density, Eq. (95) is numerically solved using the radius and pressure of the marginally igniting shells $\hat{\epsilon}_0 \rightarrow \infty$ discussed earlier [Eqs. (64)]. Since the hot-spot density at the beginning of the deceleration phase is negligible, we solve Eq. (95) with the initial condition $\hat{\rho}(0) \rightarrow 0$ leading to the stagnation value $\hat{\rho}_{\text{stag}} \approx 0.83$. Substituting the marginal ignition condition $\Upsilon_\alpha \approx 2.6$ and $\hat{R}_{\text{stag}} \approx 1.23 / \sqrt{\hat{\epsilon}_0}$ into Eqs. (96) and (97) yields the stagnation value of the hot-spot areal density and central temperature of marginally igniting capsules:

$$\rho R(\text{stag}) = 0.18 \text{ (g/cm}^2\text{)} \left[\frac{V_{\text{imp}} \text{ (cm/s)}}{3 \times 10^7} \right]^{3/7}, \quad (98)$$

$$T_{\text{hs}}(r=0, \text{stag}) = 10 \text{ (keV)} \left[\frac{V_{\text{imp}} \text{ (cm/s)}}{3 \times 10^7} \right]^{4/7}. \quad (99)$$

To estimate the fraction θ_α of absorbed alpha particles we follow the work of Basko and set $\theta_\alpha = \text{Min}[1, \theta_0]$, where $\theta_0 = 50 \int_0^{R_{\text{hs}}} (\rho / T_{\text{hs}}^{1.2}) dr$ with T_{hs} in keV and ρ in g/cm². After a straightforward manipulation, we find that for marginally igniting capsules (i.e., $\Upsilon_\alpha \approx 2.6$),

$$\theta_\alpha \approx \text{Min} \left\{ 1, 1.4 \left[\frac{3 \times 10^7}{V_{\text{imp}} \text{ (cm/s)}} \right]^{9/35} \right\}, \quad (100)$$

indicating that the fraction of absorbed alpha particles is close to unity for implosion velocities typical of direct-drive ICF. If

we require that $\theta > 0.7$ for the theory to be applicable with a reasonably small error, then Eq. (100) provides a constraint on the implosion velocity, i.e., $V_{\text{imp}} < 4 \times 10^8 \text{ (cm/s)}$. The next step is to determine the volume average temperature to verify the assumption concerning the quadratic behavior of $\langle \sigma v \rangle$. Integrating Eq. (41) of Ref. 8 over the hot-spot volume yields $\bar{T}_{\text{hs}} \approx 0.7 T_{\text{hs}}(0, t)$. The average temperature of marginal igniting capsules is then found from Eq. (99), and the resulting condition $\bar{T}_{\text{hs}} > 6 \text{ keV}$ leads to another constraint on the implosion velocity, i.e., $V_{\text{imp}} > 2 \times 10^7 \text{ (cm/s)}$. In summary, both assumptions are simultaneously satisfied as long as the implosion velocity is in the range

$$2 \times 10^7 < V_{\text{imp}} \text{ (cm/s)} < 4 \times 10^8, \quad (101)$$

which is the typical range of directly driven capsules. Observe that the condition $\bar{T}_{\text{hs}} > 6 \text{ keV}$ also implies that the alpha heating is significantly larger than the radiation losses, indicating that the bremmstrahlung term can indeed be neglected in the energy equation.

Conclusions

A model for the deceleration phase and marginal ignition of imploding capsules is derived by solving a set of ordinary differential equations describing the hot-spot energy balance and the shell dynamics including the return shock propagation. The change of adiabat induced by the shock is also calculated, and the relation between the in-flight and stagnation adiabats is in general agreement with the numerical fit of LASNEX simulations⁵ and the self-similar solution of Ref. 6. The minimum kinetic energy required for ignition is also calculated from the same model. The marginal ignition scaling is determined in terms of the stagnation as well as the in-flight adiabat. Both scaling relations are in good agreement with the numerical fit of Ref. 5.

ACKNOWLEDGMENT

This work was supported by the U.S. Department of Energy Office of Inertial Confinement Fusion under Cooperative Agreement No. DE-FC03-92SF19460, the University of Rochester, and the New York State Energy Research and Development Authority. The support of DOE does not constitute an endorsement by DOE of the views expressed in this article.

REFERENCES

1. W. K. Levedahl and J. D. Lindl, Nucl. Fusion **37**, 165 (1997).
2. A. R. Piriz, Fusion Eng. Des. **32-33**, 561 (1996).
3. M. M. Basko, Nucl. Fusion **35**, 87 (1995).
4. M. M. Basko and J. Johner, Nucl. Fusion **38**, 1779 (1998).
5. M. C. Herrmann, M. Tabak, and J. D. Lindl, Nucl. Fusion **41**, 99 (2001).
6. A. Kemp, J. Meyer-ter-Vehn, and S. Atzeni, Phys. Rev. Lett. **86**, 3336 (2001).
7. J. Meyer-ter-Vehn, Nucl. Fusion **22**, 561 (1982).
8. Laboratory for Laser Energetics LLE Review **85**, 1, NTIS document No. DOE/SF/19460-378 (2001). Copies may be obtained from the National Technical Information Service, Springfield, VA 22161.
9. H.-S. Bosch and G. M. Hale, Nucl. Fusion **32**, 611 (1992).

Publications and Conference Presentations

Publications

- R. Adam, R. Sobolewski, and M. Darula, "Subpicosecond Dynamics of the Switching Process in Y-Ba-Cu-O Josephson Junctions," in *Superconducting and Related Oxides: Physics and Nanoengineering IV*, edited by I. Bozovic and D. Pavuna (SPIE, Bellingham, WA, 2000), Vol. 4058, pp. 230–244.
- T. R. Boehly, A. Babushkin, D. K. Bradley, R. S. Craxton, J. A. Delettrez, R. Epstein, T. J. Kessler, J. P. Knauer, R. L. McCrory, P. W. McKenty, D. D. Meyerhofer, S. P. Regan, W. Seka, S. Skupsky, V. A. Smalyuk, R. P. J. Town, and B. Yaakobi, "Optical and Plasma Smoothing of Laser Imprinting in Targets Driven by Lasers with SSD Bandwidths Up to 1 THz," *Phys. Plasmas* **8**, 2331 (2001) (invited).
- D. P. Butler, Z. Celik-Butler, and R. Sobolewski, "Y-Ba-Cu-O as an Infrared Radiation Sensing Material," in *Handbook of Advanced Electronic and Photonic Materials and Devices*, edited by H. S. Nawly, Vol. 3: High T_c Superconductors and Organic Conductors (Academic Press, NY, 2001), Chap. 4, pp. 169–195.
- G. N. Gol'tsman, O. Okunev, G. Chulkova, A. Dzardanov, A. Lipatov, A. Semenov, K. Smirnov, B. Voronov, C. Williams, and R. Sobolewski, "Picosecond Superconducting Single-Photon Optical Detector," *Appl. Phys. Lett.* **79**, 705 (2001).
- V. N. Goncharov, P. McKenty, S. Skupsky, R. Betti, R. L. McCrory, and C. Cherfils-Clérouin, "Modeling Hydrodynamic Instabilities in Inertial Confinement Fusion Targets," *Phys. Plasmas* **7**, 5118 (2001).
- P. A. Jaanimagi, R. Boni, and R. L. Keck, "Neutron-Induced Background in Charge-Coupled Device Detectors," *Rev. Sci. Instrum.* **72**, 801 (2001).
- C. K. Li, D. G. Hicks, F. H. Séguin, J. Frenje, R. D. Petrasso, J. M. Soures, P. B. Radha, V. Yu. Glebov, C. Stoeckl, J. P. Knauer, F. J. Marshall, D. D. Meyerhofer, S. Skupsky, S. Roberts, C. Sorce, T. C. Sangster, T. W. Phillips, and M. D. Cable, "Measuring Fusion Yields, Areal Densities, and Ion Temperatures of Imploded Capsules at OMEGA," *Rev. Sci. Instrum.* **72**, 864 (2001).
- P. W. McKenty, V. N. Goncharov, R. P. J. Town, S. Skupsky, R. Betti, and R. L. McCrory, "Analysis of a Direct-Drive Ignition Capsule Designed for the National Ignition Facility," *Phys. Plasmas* **8**, 2315 (2001) (invited).
- D. D. Meyerhofer, J. A. Delettrez, R. Epstein, V. Yu Glebov, V. N. Goncharov, R. L. Keck, R. L. McCrory, P. W. McKenty, F. J. Marshall, P. B. Radha, S. P. Regan, S. Roberts, W. Seka, S. Skupsky, V. A. Smalyuk, C. Sorce, J. M. Soures, C. Stoeckl, R. P. J. Town, B. Yaakobi, J. D. Zuegel, R. D. Petrasso, S. Padalino, J. A. Frenje, D. G. Hicks, F. H. Séguin, C. K. Li, N. Izumi, R. Lerche, T. C. Sangster, and T. W. Phillips, "Core Performance and Mix in Direct-Drive Spherical Implosions with High Uniformity," *Phys. Plasmas* **8**, 2251 (2001) (invited).
- V. A. Smalyuk, T. R. Boehly, L. S. Iwan, T. J. Kessler, J. P. Knauer, F. J. Marshall, D. D. Meyerhofer, C. Stoeckl, B. Yaakobi, and D. K. Bradley, "Fourier-Space Image Processing for Spherical Experiments on OMEGA," *Rev. Sci. Instrum.* **72**, 635 (2001) (invited).
- V. A. Smalyuk, B. Yaakobi, J. A. Delettrez, F. J. Marshall, and D. D. Meyerhofer, "Compressed-Shell Integrity Measurements in Spherical Implosions Experiments," *Phys. Plasmas* **8**, 2872 (2001).
- R. Sobolewski, D. P. Butler, and Z. Celik-Butler, "Cooled and Uncooled Infrared Detectors Based on Yttrium Barium Copper Oxide," in *Smart Optical Inorganic Structures and Devices*, edited by S. P. Asmontas and J. Gradauskas (SPIE, Bellingham, WA, 2001), Vol. 4318, pp. 204–214 (invited).

Forthcoming Publications

S. R. Arrasmith, S. D. Jacobs, I. A. Kozhinova, A. B. Shorey, D. Golini, W. I. Kordonski, S. Hogan, and P. Dumas, "Development and Characterization of Magnetorheological Fluids for Optical Finishing," to be published in the Proceedings of Fine Powder Processing '99, University Park, PA, 20–22 September 1999.

A. Babushkin, M. J. Harvey, and M. D. Skeldon, "The Output Signal-to-Noise Ratio of a Nd:YLF Regenerative Amplifier," to be published in Applied Optics.

R. Betti and J. P. Freidberg, "Low- β , Magnetohydrodynamic Tokamak Equilibria with Poloidal Transonic Flow," to be published in Physical Review Letters.

T. R. Boehly, J. A. Delettrez, J. P. Knauer, D. D. Meyerhofer, B. Yaakobi, R. P. J. Town, and D. Hoarty, "The Effect of Shock Heating on the Stability of Laser-Driven Targets," to be published in Physical Review Letters.

T. R. Boehly, V. N. Goncharov, O. Gotchev, J. P. Knauer, D. D. Meyerhofer, D. Oron, S. P. Regan, Y. Srebro, W. Seka, D. Shvarts, S. Skupsky, and V. A. Smalyuk, "The Effect of Plasma Formation Rate and Beam Smoothing on Laser Imprinting," to be published in Physical Review Letters.

B. Buerke and D. D. Meyerhofer, "Accurate Measurement of Hydrogenic Tunneling Rates in a High-Intensity Laser Focus," to be published in Physical Review Letters.

W. R. Donaldson, J. H. Kelly, R. L. Keck, and R. Boni, "Predicting and Measuring Optical Pulse Shapes on the OMEGA Laser System," to be published in the OSA Technical Digest.

F. Y. Fan, S. W. Culligan, J. C. Mastrangelo, D. Katsis, and S. H. Chen, "Novel Glass-Forming Liquid Crystals. VI. High-Temperature Glassy Nematics," to be published in Chemical Materials.

J. A. Frenje, D. G. Hicks, C. K. Li, F. H. Séguin, R. D. Petrasso, K. Fletcher, H. Olliver, S. Padalino, S. Thompson, J. M. Soures, S. Roberts, C. Sorce, T. C. Sangster, and T. W. Phillips, "CR-39 Tract Detector Response to Charged Particles and Neutrons," to be published in the Review of Scientific Instruments.

O. A. Konoplev, Y. Fisher, and D. D. Meyerhofer, "Generation of a Picosecond Laser Pulse with an Intensity Contrast of Eleven Orders of Magnitude," to be published in Optics Letters.

V. Lobatchev and R. Betti, "Ablative Stabilization of the Deceleration-Phase Rayleigh–Taylor Instability," to be published in Physical Review Letters.

A. E. Marino, S. D. Jacobs, L. L. Gregg, G. Chen, and Y. Due, "Durable Phosphate Glasses with Lower Transition Temperatures," to be published in the Journal of Non-Crystalline Solids.

J. A. Marozas, "Self- and Cross-Phase Modulation of High-Intensity Laser Beams Emerging from a Diamond-Turned KDP Wedge," to be published in the Journal of the Optical Society of America B.

J. A. Marozas, S. P. Regan, J. H. Kelly, D. D. Meyerhofer, W. Seka, and S. Skupsky, "Laser Beam Smoothing Caused by the Small-Spatial-Scale β -Integral," to be published in the Journal of the Optical Society of America B.

J. A. Marozas, J. D. Zuegel, D. Jacobs-Perkins, and J. H. Kelly, "Angular Spectrum Representation of Pulsed Laser Beams with Two-Dimensional Smoothing by Spectral Dispersion," to be published in the Journal of the Optical Society of America B.

R. L. McCrory, R. E. Bahr, R. Betti, T. R. Boehly, T. J. B. Collins, R. S. Craxton, J. A. Delettrez, W. R. Donaldson, R. Epstein, J. Frenje, V. Yu. Glebov, V. N. Goncharov, O. V. Gotchev, R. Q. Gram, D. R. Harding, D. G. Hicks, P. A. Jaanimagi, R. L. Keck, J. Kelly, J. P. Knauer, C. K. Li, S. J. Loucks, L. D. Lund, F. J. Marshall, P. W. McKenty, D. D. Meyerhofer, S. F. B. Morse, R. D. Petrasso, P. B. Radha, S. P. Regan, S. Roberts, F. Séguin, W. Seka, S. Skupsky, V. A. Smalyuk, C. Sorce, J. M. Soures, C. Stoeckl, R. P. J. Town, M. D. Wittman, B. Yaakobi, and J. D. Zuegel, "OMEGA ICF Experiments and Preparation for Direct-Drive Ignition on NIF," to be published in the proceedings of the 18th IAEA Fusion Energy Conference.

A. V. Okishev, R. Boni, M. Millecchia, P. A. Jaanimagi, W. R. Donaldson, R. L. Keck, W. Seka, K. V. Dukelsky, M. A. Eronyan, V. S. Shevandin, G. A. Ermolaeva, G. Nikolaev, and V. B. Shilov, "Unique High-Bandwidth, UV Fiber Delivery System for the OMEGA Diagnostic Applications," to be published in the IEEE Journal on Selected Topics in Quantum Electronics.

F. H. Séguin, C. K. Li, D. G. Hicks, J. A. Frenje, R. D. Petrasso, J. M. Soures, V. Yu. Glebov, C. Stoeckl, P. B. Radha, D. D. Meyerhofer, S. Roberts, C. Sorce, T. C. Sangster, and M. D. Cable, "Diagnostic Use of Secondary D³He Proton Spectra for D-D OMEGA Targets," to be published in Physics of Plasmas.

M. D. Skeldon, "An Optical-Pulse-Shaping System Based on an Electrooptic Modulator Driven by an Aperture-Coupled-Stripline Electrical-Waveform Generator," to be published in the Journal of the Optical Society of America B.

S. Skupsky, R. L. McCrory, R. E. Bahr, T. R. Boehly, T. J. B. Collins, R. S. Craxton, J. A. Delettrez, W. R. Donaldson, R. Epstein, V. N. Goncharov, R. Q. Gram, D. R. Harding, P. A. Jaanimagi, R. L. Keck, J. P. Knauer, S. J. Loucks, F. J. Marshall, P. W. McKenty, D. D. Meyerhofer, S. F. B. Morse, O. V. Gotchev, P. B. Radha, S. P. Regan, W. Seka, V. A. Smalyuk, J. M. Soures, C. Stoeckl, R. P. J. Town, M. D. Wittman, B. Yaakobi, J. D. Zuegel, R. D. Petrasso, D. G. Hicks, and C. K. Li, "Recent Progress in Direct-Drive ICF Research at the Laboratory for Laser Energetics," to be published in SPIE's Proceedings of the XXVI European Conference on Laser Interaction with Matter.

V. A. Smalyuk, B. Yaakobi, J. A. Delettrez, F. J. Marshall, D. D. Meyerhofer, S. P. Regan, and R. P. J. Town, "Evolution of Shell Nonuniformities Near Peak Compression of Spherical Implosion," to be published in Physical Review Letters.

D. J. Smith, J. A. Warner, N. E. LeBarron, T. J. Kessler, and S. LaDelia, "The Development of Ion-Etched Phase Plates," to be published in Applied Optics.

E. A. Startsev and C. J. McKinstry, "Relativistic Ponderomotive Dynamics of a Test Particle in a Plasma," to be published in Physical Review E.

F.-Y. Tsai, E. L. Alfonso, S. H. Chen, and D. R. Harding, "Processing Vapor-Deposited Polyimide," to be published in the Journal of Applied Physics.

B. Yaakobi, C. Stoeckl, T. Boehly, D. D. Meyerhofer, and W. Seka, "Measurement of Preheat due to Fast Electrons in Laser Implosions," to be published in SPIE's Proceedings of the XXVI European Conference on Laser Interaction with Matter.

J. D. Zuegel and D. W. Jacobs-Perkins, "An Efficient, High-Frequency Bulk Phase Modulator," to be published in Applied Optics.

J. D. Zuegel and S. A. Letzring, "Bulk Microwave Phase Modulators for Smoothing by Spectral Dispersion," to be published in Applied Optics.

Conference Presentations

The following presentations were made at OPTO Northeast and Imaging 2001, Rochester, NY, 10–11 April 2001:

J. E. DeGroote, S. D. Jacobs, L. L. Gregg, and A. E. Marino, "Exploring Optical Polishing Pitch."

L. L. Gregg and S. D. Jacobs, "The Optics Suitcase—A Tool for Learning."

M. J. Guardalben, L. Ning, N. Jain, D. J. Battaglia, and K. L. Marshall, "Comparison of a Liquid Crystal Point Diffraction Interferometer (LCPDI) and a Commercial Phase-Shifting Interferometer."

S. D. Jacobs, S. R. Arrasmith, I. A. Kozhinova, L. L. Gregg, H. J. Romanofsky, and A. B. Shorey, "Magnetorheological Finishing: MRF of Optical Glasses and Crystals."

A. E. Marino, S. R. Arrasmith, L. L. Gregg, S. D. Jacobs, G. Chen, and Y. Duc, "Developing a Durable Phosphate Glass with a Low Glass Transition Temperature."

J.-R. Park, W. R. Donaldson, R. Boni, and R. Sobolewski, "Optical Properties of a Dual Diffusing Sphere Fiber Optic Detector."

The following presentations were made at the Conference on Lasers and Electro-Optics, Baltimore, MD, 6–11 May 2001:

W. R. Donaldson, J. H. Kelly, R. L. Keck, and R. Boni, “Predicting and Measuring Optical Pulse Shapes on the OMEGA Laser System.”

M. J. Guardalben, A. Babushkin, R. S. Craxton, R. L. Keck, W. R. Donaldson, and K. A. Thorp, “Obtaining UV Energy Balance with 1-THz Spectral Bandwidth on the 60-Beam OMEGA Laser.”

J. Li, T. Y. Hsiang, and W. R. Donaldson, “High-Speed Bragg Modulator on AlGaAs Waveguides.”

T. Z. Kosc, K. L. Marshall, S. D. Jacobs, and B. Klehn, “Polymer Cholesteric Liquid Crystal Flakes for Display and Other Electro-Optic Applications,” Novel Optical Materials and Applications, NOMA Cetraro, Italy, 20–27 May 2001.

The following presentations were made at the 31st Anomalous Absorption Conference, Sedona, AZ, 3–8 June 2001:

R. S. Craxton, D. D. Meyerhofer, W. Seka, R. W. Short, and R. P. J. Town, “Design of Long-Scale-Length Plasmas for Interaction Physics Experiments on OMEGA.”

J. A. Delettrez, C. Stoeckl, S. P. Regan, P. W. McKenty, D. D. Meyerhofer, and J. P. Knauer, “Precision One-Dimensional *LILAC* Simulations of CH-Shell Implosions on the OMEGA Laser.”

R. Epstein, J. A. Delettrez, V. Yu. Glebov, V. N. Goncharov, P. W. McKenty, P. B. Radha, S. Skupsky, V. A. Smalyuk, and C. Stoeckl, “One-Dimensional Simulation of the Effects of Unstable Mix on Neutron and Charged-Particle Yield from Laser-Driven Implosions Experiments.”

V. Yu. Glebov, D. D. Meyerhofer, P. B. Radha, W. Seka, S. Skupsky, J. M. Soures, C. Stoeckl, S. Padalino, L. Baumgart, R. Colburn, J. Fuschino, and T. C. Sangster, “Current Status of Tertiary Neutron Diagnostic by Carbon Activation.”

Y. A. Kholodov, “A Comparison of Monotone Schemes of High-Order Accuracy for Hyperbolic Problems.”

V. N. Goncharov, S. Skupsky, R. Betti, J. A. Marozas, P. W. McKenty, and R. P. J. Town, “Hydrodynamic Stability of Moderate- to High-Gain Direct-Drive Target Designs for the NIF.”

S. P. Regan, J. A. Delettrez, V. A. Smalyuk, B. Yaakobi, F. J. Marshall, R. Epstein, V. Yu. Glebov, P. A. Jaanimagi, D. D. Meyerhofer, P. B. Radha, W. Seka, S. Skupsky, J. M. Soures, C. Stoeckl, R. P. J. Town, D. A. Haynes, Jr., C. F. Hooper, Jr., C. K. Li, R. D. Petrasso, and F. H. Séguin, “Core-Mix Measurements of Direct-Drive Implosions on OMEGA.”

W. Seka, S. P. Regan, D. D. Meyerhofer, B. Yaakobi, C. Stoeckl, R. S. Craxton, R. W. Short, H. Baldis, and J. Fuchs, “Multibeam SBS Interaction Experiments in OMEGA Long-Scale-Length Plasmas.”

R. W. Short, R. S. Craxton, W. Seka, and D. D. Meyerhofer, “Theoretical Interpretation of SBS Observations in OMEGA Long-Scale-Length Plasma Experiments.”

A. Simon and R. W. Short, “Damping and Spatial Propagation of Oscillations in Weakly Collisional Plasma.”

C. Stoeckl, R. E. Bahr, V. Yu. Glebov, D. D. Meyerhofer, W. Seka, R. W. Short, and B. Yaakobi, “Measurements on the Two-Plasmon-Decay Instability on OMEGA.”

A. Sunahara, J. A. Delettrez, R. W. Short, and S. Skupsky, “Electron Thermal Conduction in Inertial Confinement Fusion.”

R. L. McCrory, J. A. Delettrez, R. Epstein, V. Yu. Glebov, R. L. Keck, P. W. McKenty, F. J. Marshall, D. D. Meyerhofer, P. B. Radha, S. P. Regan, S. Roberts, W. Seka, S. Skupsky, V. A. Smalyuk, C. Sorce, C. Stoeckl, J. M. Soures, R. P. J. Town, B. Yaakobi, J. D. Zuegel, J. A. Frenje, C. K. Li, R. D. Petrasso, F. H. Séguin, K. Fletcher, S. Padalino, C. Freeman, N. Izumi, R. Lerche, T. W. Phillips, and T. C. Sangster, “Core Performance in Direct-Drive Spherical Implosions on OMEGA,” Pulsed Power Plasma Science 2001, Las Vegas, NV, 17–22 June 2001.

D. D. Meyerhofer, R. Betti, T. R. Boehly, J. A. Delettrez, R. Epstein, V. Yu. Glebov, V. N. Goncharov, D. R. Harding, R. L. Keck, R. L. McCrory, P. W. McKenty, F. J. Marshall, P. B. Radha, S. P. Regan, S. Roberts, W. Seka, S. Skupsky, V. A. Smalyuk, C. Sorce, C. Stoeckl, J. M. Soures, R. P. J. Town, B. Yaakobi, J. A. Frenje, C. K. Li, R. D. Petrasso, F. H. Séguin, K. Fletcher, S. Padalino, C. Freeman, N. Izumi, R. Lerche, T. W. Phillips, and T. C. Sangster, “Interferences of Mix in Direct-Drive Spherical Implosions with High Uniformity,” 28th EPS Conference on Controlled Fusion and Plasma Physics, Madeira, Portugal, 18–22 June 2001.

D. D. Meyerhofer, J. H. Kelly, R. P. J. Town, L. J. Waxer, S. J. Loucks, R. L. McCrory, W. Seka, and S. Skupsky, “An Integrated Fast Ignitor Experiment for OMEGA,” 5th Workshop on Fast Ignitor of Fusion Targets, Madeira, Portugal, 18–22 June 2001.

T. R. Boehly, B. Yaakobi, J. P. Knauer, D. D. Meyerhofer, and R. P. J. Town, “Measurements of Shock Heating in Laser-Driven Targets,” 12th Biennial International Conference of the APS Topical Group on Shock Compression of Condensed Matter, Atlanta, GA, 24–29 June 2001.

UNIVERSITY OF
ROCHESTER